Alma Mater Studiorum · Università di Bologna
in cotutela con Universität Bern

DOTTORATO DI RICERCA IN FISICA

Ciclo XXX
Settore Concorsuale di afferenza: 02/A1
Settore Scientifico displinare: FIS/01

Exploiting the ATLAS detector in a search for stop squark in a compressed mass spectrum using the Higgs boson

Presentata da: **Gabriele D'Amen**

Coordinatore Dottorato:
Prof.ssa Silvia Arcelli

Relatore:
Prof. Alessandro Gabrielli

Relatore:
Prof. Antonio Ereditato

Esame Finale Anno 2018

Abstract

In past decades, experimental and theoretical efforts offered several reasons to believe that the Standard Model of particles (SM) is nothing more than an effective low-energy approximation of a more fundamental theory. The theory of Supersymmetry (SUSY) seems to be a natural candidate to extend the SM. Of particular interest among SUSY particles is the stop squark, due to the fact that it gives the dominant contribution to the Higgs boson mass radiative corrections. In this thesis, I present a search for direct stop squark pair production in data collected by the ATLAS detector at the CERN Large Hadron Collider (LHC) during 2015-16 in proton-proton collisions with a centre-of-mass energy $\sqrt{s} = 13$ TeV. This search takes advantage of the full capabilities of ATLAS further increased by the improvements made to the ATLAS pixel detector during 2014 - 2015. Both the installation of a new pixel detector layer ($Insertable\ B-Layer$) and the upgrade of the data-acquisition system of the pre-existing layers are presented in detail in this thesis, along with their impact to the b-jets reconstruction efficiency. This search for stop squark relies on events with a pair of b-jets compatible with the decay of an Higgs boson to select the signal candidate events. Results of this selection are interpreted in models with long decay chains involving a heavy neutralino $\widetilde{\chi}_2^0$ or the heavier stop squark $\widetilde{t}_2$. No excess is observed in the data with respect to the SM predictions for any of the models and decay chains, thus excluding at 95% confidence level $\widetilde{t}_2$ and $\widetilde{t}_1$ masses up to about 800 GeV and extending the exclusion region of supersymmetric parameter space covered by previous LHC searches.

Sommario

Nei decenni passati, sforzi sperimentali e teorici hanno offerto molteplici ragioni per credere che il Modello Standard delle particelle elementari (SM) non sia nulla più che un'approssimazione efficacie a basse energie di una teoria più fondamentale. La teoria delle Supersimmetrie (SUSY) sembra essere un candidato ideale per estendere il Modello Standard. Il partner supersimmetrico del quark top, detto squark stop suscita particolare interesse a causa del suo contributo dominante alle correzioni radiative della massa del bosone di Higgs. In questa tesi presento dunque un lavoro di ricerca di produzione diretta di coppie di top squark in dati raccolti dal detector ATLAS al Large Hadron Collider (CERN) durante il periodo 2015 - 2016 in collisioni protone-protone con energia nel centro di massa $\sqrt{s} = 13$ TeV. Quest'analisi si avvantaggia delle piene possibilità offerte dal detector ATLAS ed incrementate dai miglioramenti effettuati al pixel detector di ATLAS durante il 2014 - 2015. In questa tesi vengono presentate in dettaglio l'installazione di un nuovo sottosistema del pixel detector ($Insertable\ B-Layer$) ed il lavoro di aggiornamento del sistema di acquisizione dati del pixel detector pre-esistente, a causa dell'impatto che essi hanno sull'efficienza di ricostruzione dei b-jet. Questa ricerca di squark top è basata sulla discriminazione di eventi contenenti una coppia di b-jet compatibile con il prodotto di decadimento di un bosone di Higgs. I risultati di tale selezione sono interpretati tramite modelli con lunghe catene di decadimento contenenti un neutralino pesante $\widetilde{\chi}_2^0$ o il secondo autostato di massa dello squark stop $\widetilde{t}_2$. Nei dati presi in esame non sono stati osservati eccessi rispetto alle previsioni del Modello Standard per nessuno dei modelli o catene di decadimento presi in esame, escludendo pertanto al 95% di livello di confidenza masse per $\widetilde{t}_2$ e $\widetilde{t}_1$ fino a circa 800 GeV ed estendendo dunque la regione di esclusione dello spazio dei parametri di supersimmetria coperta da precedenti analisi ad LHC.

Contents

Introduction

"Citius! Altius! Fortius!" (Faster! Higher! Stronger!) has been the motto of the Modern Olympic Games since their re-foundation in 1896. This principle is also a fitting metaphor for the evolution of the accelerator experiments in high-energy physics, as probing the fundamental laws of nature requires us to push the energy frontier higher and higher. This is why a machine such as the Large Hadron Collider (LHC from now on) was built.

The Large Hadron Collider is a proton-proton/heavy ions collider located at CERN, near Geneva (CH). It gives us the possibility to probe uncharted phase-space regions and study what lies beyond the current Standard Model (SM) of particle physics. Multiple questions are still unanswered in modern physics: the existence of Dark Matter and its interaction with baryonic matter; the unification of the known interactions at high energies; the hierarchy problem of the electro-weak scale are some examples. The latter affects the Higgs boson mass: without any additional symmetry stabilizing the electroweak scale by providing a cancellation mechanism, the Higgs mass receives large corrections by the one-loop diagram contributions. An answer to this problem (and partially, of the other two questions presented) could be given by Supersymmetric extensions of the Standard Model (SUSY). The search for evidences of SUSY at LHC is motivated by the fact that some particles belonging to these models are expected to be observable at energies achievable by the LHC, such as the top squark (supersymmetric quark).

This thesis presents a search for evidence of the supersymmetric top squark $\widetilde{t}$ which I performed with the ATLAS experiment at CERN, using data acquired in proton-proton collisions during the Run-2 period. This analysis targets the decay of the lightest stop mass eigenstate $\widetilde{t}_1$ into a neutralino and a top quark in an yet unexplored portion of the $\widetilde{t}_1 - \widetilde{\chi}_1^0$ mass space where $m_{\widetilde{t}_1} - m_{\widetilde{\chi}_1^0} = m_t$. Previous searches had very limited reach in this region, as the top quark originating from the stop decay is produced at rest leaving a signature similar to the dominating SM $t\bar{t}$ production.

The plan is to target this kinematic region by creating the $\widetilde{t}_1$ as a decay product of the heavier mass eigenstate $\widetilde{t}_2$ in the two-body decay $\widetilde{t}_2 \to \widetilde{t}_1 + h$. As the $\widetilde{t}_2$ is expected to be significantly more massive than the $\widetilde{t}_1$, the latter is produced with an appreciable boost. Invisible particles originating from its decay, such as neutrinos and neutralinos, will therefore give rise to some E_{T}^{miss} in the final state. My search strategy is use this E_{T}^{miss}, together with the signature of the Higgs boson decay $h \to b\bar{b}$, to detect the production of $\widetilde{t}_2$ at the LHC. This

search has been performed in the context of a simplified model where only $\widetilde{t}_1$, $\widetilde{t}_2$, $\widetilde{\chi}_1^0$ and $\widetilde{\chi}_2^0$ are considered as active particles. A set of different models is taken into account, each targeting a different mass splitting between the $\widetilde{t}_2$ and the $\widetilde{t}_1$. I then analysed the collected data with a cut-and-count method by applying requirements on kinematic variables of the stop quark decay products. Due to the wide spectrum of possible masses for these particles, the kinematics of the $\widetilde{t}_2 \rightarrow \widetilde{t}_1 + h$ decay can be extremely heterogeneous and therefore three different Signal Regions targeting different kinematic of this decay have been set in place.

Even in case the $\widetilde{t}_1$ exist, its production cross-section is expected to be small, thus needing the acquisition of large amounts of data to observe a statistically relevant number of $\widetilde{t}_1$. To address this issue, the beam luminosity at LHC was increased with respect to the first data taking period. This luminosity increase led to the necessity of an upgrade of the ATLAS Pixel Detector, as the increased data troughput caused de-synchronization issues and high-bandwidth occupancy with subsequent data loss. Radiation damages occurred to the pixel subsystem during Run-I led to degraded b-tagging capabilities, thus requiring the installation of a new pixel detector layer, the IBL. While the front-end electronics of the Pixel Detector remained unchanged with respect to Run-1, the data-acquisition system had to be revamped with IBL-inspired read-out boards, namely the *Read-Out Driver* and the *Back-Of-Crate*; I took care of the commissioning of both the electronic components and the firmware of these boards, as well as developing custom software for the data-taking system and evaluating their interaction with the pixel detector system. In addition, I developed testing hardware of the new Opto-Electrical transceiver RX-Plugin, designed as an interface between the front-end electronics to the read-out boards. The upgraded detector was used for data-taking during Run-2, providing solid performances and stability with enhanced data reconstruction efficiency, with respect to Run-1.

During the thesis period, I signed 174 publications (some still pending) as a member of the ATLAS community, including the paper[1] presenting the analysis hereby included. Three[2] proceedings at national and international conferences (two[3][4] of which have been submitted but not yet published) document my work on the upgrade of the pixel detector and future developments of the sys-

[1] ATLAS Collaboration (D'Amen, G. et al.), *Search for direct top squark pair production in events with a Higgs or Z boson, and missing transverse momentum in $\sqrt{s}$ = 13 TeV pp collisions with the ATLAS detector*, Jun 13, 2017. 29 pp. Published in **JHEP 1708 (2017) 006**

[2] D'Amen, G., *ATLAS pixel detector: Readout upgrades for Run2 and beyond*, **IL NUOVO CIMENTO 40 C (2017) 80**

[3] A. Gabrielli, F. Alfonsi, G. Balbi, G. D'Amen, D. Falchieri N. Giangiacomi, G. Pellegrini, R. Travaglini- *Commissioning of ROD Boards for the Entire ATLAS Pixel Detector* - TWEPP 2017 Topical Workshop on Electronics for Particle Physics 11-15 September (2017) Santa Cruz Ca (USA) (POSTER) **PoS(TWEPP-17)113**

[4] A. Gabrielli, F. Alfonsi, G. Balbi, G. D'Amen, D. Falchieri N. Giangiacomi, G. Pellegrini, R. Travaglini- *A Multi-Channel PCI Express Readout Board Proposal for the Pixel Upgrade at LHC* - TWEPP 2017 Topical Workshop on Electronics for Particle Physics 11-15 September (2017) Santa Cruz Ca (USA) (POSTER) **PoS(TWEPP-17)068**

tem. Finally, a paper documenting my work in microelectronic design outside the ATLAS community has been published[5].

The thesis is organized as follows: **Chapter 1** introduces both the LHC collider and the system used to collect data from it, the ATLAS experiment; **Chapter 2** focuses on the upgrade of the ATLAS innermost system, the pixel detector, to whom I personally contributed; A brief introduction to the limits of the SM and to the nature of its supersymmetrical extension is given in **Chapter 3**; **Chapter 4** explains the phenomenological aspects of the search for the stop squark and the data samples used to search for its production at LHC; **Chapter 5** covers the entire analysis process, giving particular attention to the reconstruction of the Higgs boson from the stop decay chain; results of this selection are compared to the ones expected for the sole SM hypothesis and reported in **Chapter 6**, together with extrapolated results of alternative interpretations with the same final signature. Finally, **Chapter 7** compares the obtained results with previous results in SUSY searches and other SUSY channels complementing this analysis.

[5]Gabrielli, A; Bastianini, S; Crepaldi, M; D'Amen, G; Demarchi, D; Lax, I; Ros, P Motto; Zoccoli, G, *Low power wireless ultra-wide band transmission of bio-signals*, **JOURNAL OF INSTRUMENTATION**, 2014, 9, pp. 1 - 9

Part I

Accelerators for High-Energy Physics

Chapter 1

LHC and the ATLAS experiment

This thesis presents a search for evidences of new physics performed on data collected by the ATLAS experiment from proton-proton collisions at the Large Hadron Collider (LHC), with a center-of-mass energy of $\sqrt{s} = 13$ TeV, acquired during 2015 and 2016. An introduction to the experimental setup is presented in this chapter, as well as an overview of past major results and improvements achieved during the last two years.

1.1 The Large Hadron Collider

The Large Hadron Collider (LHC) is a two-ring-superconducting proton/ion accelerator installed in the pre-existing 26.7 km tunnel built between 1989 and 2000 for the Large Electron-Proton Collider (LEP) at CERN (Conseil Europeen pour la Recherche Nucleaire) under the border between France and Switzerland [1].
The approval of the LHC project was given by the CERN Council in December 1994 with the plan to build the machine in two stages, but the idea was later scrapped in favour of a single stage project. The final design of the accelerator is capable of reaching a center-of-mass energy per collision of 14 TeV for the protons, broadening the phase space region accessible to probe new physics beyond the Standard Model, with a specific focus on the observation of the Higgs boson and particles predicted by supersymmetrical extensions (SUSY) of the standard model.

Unlike previous particle-antiparticle colliders (such as LEP and Tevatron), in which both beams share the same phase space in a single ring, the LHC machine is based on proton-proton collisions. The two beams of protons travel in two counter-rotating rings, crossing in eight different locations (called points) flanked by long straight sections for Radio Frequency (RF) cavities, which are used to accelerate particles and compensate the high synchrotron radiation losses. The main motivation to use hadrons instead of electron-positron pairs in a circular collider (as was LEP) is in fact the increased limit of achievable center-of-mass energy, which, in case of electron-positron accelerators, is strongly limited by energy losses from the synchrotron radiation. The latter is an electromagnetic radiation generated by radially accelerated charged particles; in circular colliders the main contributions to this phenomenon comes

from the dipole magnets used to bend the charged particles trajectory.

In general, the energy loss due to the synchrotron radiation in circular colliders can be expressed as:

$$\frac{dE}{dt} \propto \frac{E^4}{m^4 R^2} \tag{1.1}$$

where E is the energy of the beam particle, m the mass of the accelerated particle and R the bending radius. The factor is extremely less relevant for protons, due to their high mass (2,000 times higher than the electron) as the synchrotron radiation is proportional with $\frac{1}{m^4}$. The high-energy proton beams travel close to the speed of light in opposite directions inside the accelerator. Each beam is composed of a number n_b (2,808 for each proton beam[1][2]) of particle bunches, colliding head-on every 25 ns (*bunch spacing*). Taking into account these data, the number of events of interest (i.e. the number of occurrences of the processes we're interested into) per second generated inside the LHC is:

$$N_{process} = \mathcal{L} \cdot \sigma_{process} \tag{1.2}$$

where $\sigma_{process}$ is the cross section of the process under study and $\mathcal{L}$ is the machine *luminosity*, which is defined as the number N of events with interaction cross section σ detected in a certain time period t and can be written, assuming a gaussian distribution for the colliding bunches, as:

$$\mathcal{L} = \frac{1}{\sigma}\frac{dN}{dt} = \frac{N_b^2 \cdot n_b \cdot f_{rev} \cdot \gamma_r}{4\pi \cdot \epsilon_n \cdot \beta^*} F \tag{1.3}$$

where:

N_b is the number of particles per bunch

f_{rev} the revolution frequency of the bunches in the accelerator

γ_r the relativistic gamma factor of the particles

ϵ the normalized transverse beam emittance

β^* the beta function at the collision point

F the geometric luminosity reduction factor, due to the crossing angle of the two beams at the interaction point (IP)

The exploration of rare events (i.e. events with low σ) at the LHC requires therefore a high luminosity, achieved with high-intensity and high-energy beams. The total amount of collisions data collected during a period of time is defined as *integrated luminosity*:

$$L = \int_{\Delta t} \mathcal{L} \cdot dt \tag{1.4}$$

Examples of integrated luminosity recorded by the ATLAS detector are shown as total integrated luminosity collected by the ATLAS detector per year (Fig. 1.1) and integrated luminosity recorded during 2016 by the ATLAS detector with respect to the total integrated luminosity delivered by the LHC (Fig. 1.2).

As previously introduced, these beams are not continuous but are divided in

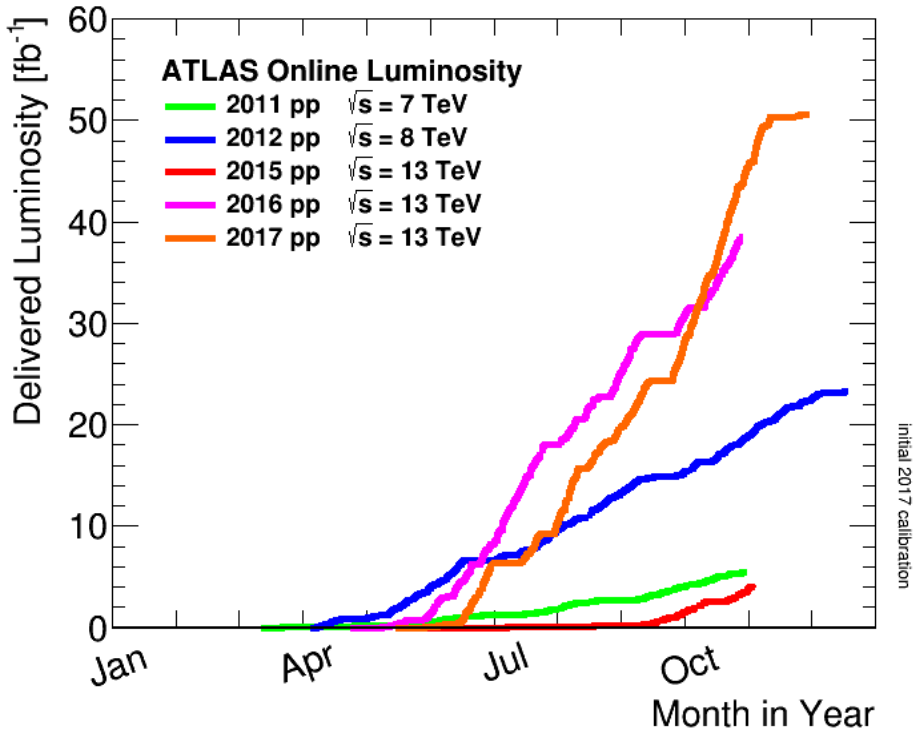

Figure 1.1: Integrated luminosity collected by the ATLAS detector for each year in the period 2011-2017, in pp collisions at different centre-of-mass energies delivered by the LHC.

bunches (each containing $\sim 10^{11}$ protons) with a minimum time separation of 25 ns. In every bunch-crossing, elastic and inelastic collisions prevent the interacting protons from continuing to circulate in the beam pipe in phase with the original bunches, resulting in a degradation over time of the beam luminosity:

$$\mathcal{L} = \mathcal{L}_0 e^{\frac{-t}{\tau}} \tag{1.5}$$

where the time constant τ is of the order of 15 h, thus making possible to circulate the beam for hours without requiring a refill. The potentiality of the LHC has not been exploited from the start of the operations (in 2010), as it was decided to slowly approach the design goals of the machine one step at the time, while constantly upgrading and improving the accelerator and the experiments surrounding it. The evolution of the beam parameters over time is presented in Tab. 1.1.

[1] Calculated from the bunch instantaneous luminosity ($\mathcal{L}_{bunch}$) as $\mu = \mathcal{L}_{bunch} \cdot \frac{\sigma_{inel}}{f_{rev}}$. σ_{inel} is the inelastic cross section and f_{rev} is the LHC revolution frequency.

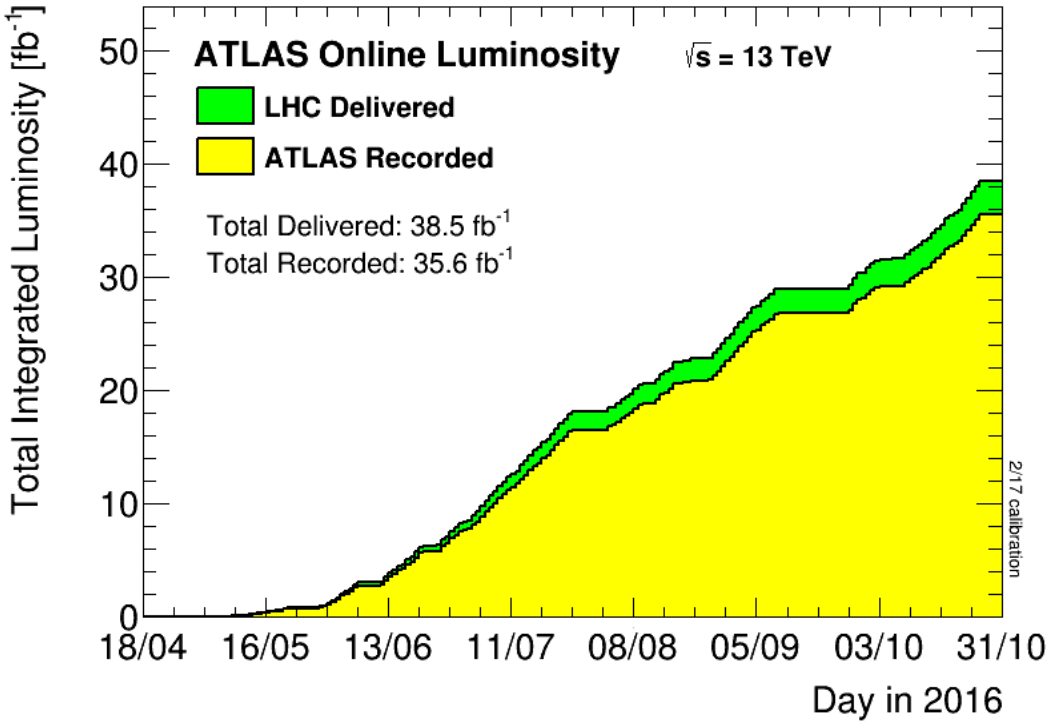

Figure 1.2: Cumulative luminosity versus time delivered to (green) and recorded by (yellow) ATLAS during stable beams for pp collisions at 13 TeV centre-of-mass energy in 2016. The delivered luminosity accounts for luminosity delivered from the start of stable beams until the LHC requests ATLAS to put the detector in a safe standby mode to allow for a beam dump or beam studies. Shown is the luminosity as determined from counting rates measured by the luminosity detectors.

Parameter / Year	2010	2011	2012	2015	2016	**Design**
Energy per Beam (TeV)	3.5	3.5	4	6.5	6.5	**7**
Bunch spacing (ns)	150	75-50	50	25	25	**25**
Peak Luminosity ($\times 10^{32} cm^{-2} s^{-1}$)	2.1	37	77	44	140	**100**
Delivered Luminosity (fb^{-1})	0	5.46	23.08	4.34	38.71	**-**

Table 1.1: Evolution of the beam parameters as seen by the ATLAS experiment in the 2010-16 period. During 2013 and 2014 no data was delivered, as the machine was experiencing an upgrade shutdown (Long Shutdown I). Design values are present for comparison.

1.2 LHC layout

The problem of detecting and studying the wide spectrum of different particles and phenomena created in the *pp* collisions is left to the four main experiments built around the ring of LHC. Out of these four experiments, two are focused on exploiting the high luminosity provided by the LHC, namely ATLAS and CMS, both aiming at a peak luminosity of $\mathcal{L} = 1 \times 10^{34}\ cm^{-2}s^{-1}$ for proton-proton collisions; this goal luminosity was achieved and surpassed in 2015.
A third experiment, LHCb, is designed to investigate the flavour physics of the B mesons and their involvement in CP violation. Finally, the ALICE experiment is dedicated to the study of heavy ion collisions and the ensuing production of quark-gluon plasma. Both ALICE and LHCb operate at a lower luminosity (respectively $\mathcal{L}_{ALICE} = 10^{27} cm^{-2}s^{-1}$ and $\mathcal{L}_{LHCb} = 10^{32} cm^{-2}s^{-1}$).
These experiments are located in specific points of the LHC layout, which is divided into eight arcs and eight straight section, each 528 m long, serving as an experimental or utility insertion. As shown in Fig. 1.3, the ATLAS experiment is located at Point 1 and the the CMS experiment at Point 5.

Protons travelling inside LHC are not accelerated in a single stage, but through a series of smaller accelerators injecting higher and higher energy protons into subsequent stages of the "injection chain".
The injection chain is shown in Fig. 1.4 and starts with the linear accelerator *Linac2*, which accelerates protons up to the energy of 50 MeV, injecting the beam at a rate of 1 Hz in the *Proton Synchrotron Booster* (*PSB*), which increases the energy to 1.4 GeV/proton. The *Proton Synchrotron* (*PS*) further increases this energy from 1.4 to 25 GeV, separating the protons in bunches and feeding the particle packets to the *Super Proton Synchrotron* (*SPS*). After the SPS the beams, with an energy of 450 GeV/proton, are injected directly into the LHC.

These accelerators were pre-existing but received a substantial upgrade during the LHC construction to meet the very stringent needs of the LHC: many high intensity proton bunches (2808 per LHC ring) with small transverse and well defined longitudinal emittances are required for the operations. The PS complex now provides twice the transverse beam brightness (defined as $\frac{intensity}{emittance}$) with respect to the past performances and proton bunches with the LHC spacing of 25 ns. A new linear accelerator, *Linac4*, will replace Linac2 in 2020 as a proton source for the LHC. The total (integrated) luminosity produced at the end of this chain by the LHC in one run is:

$$L_{int} = L_0 \tau_L \left[1 - e^{-T_{run}/\tau_L}\right] \tag{1.6}$$

where T_{run} is the total length of the run. It's worth mentioning that other accelerators are used for different types of injection in the LHC: *Linac3* accelerates lead ions for fixed target experiments, injecting the bunches in the *Low Energy Ion Ring*, which compresses the received bunches for injection in the LHC; the *Antiproton Decelerator* slows down antiprotons so they can be used to study antimatter. Heavy ion collisions are operated at LHC using beams of fully stripped lead ions ($^{208}Pb^{82+}$); with a nominal magnetic field of

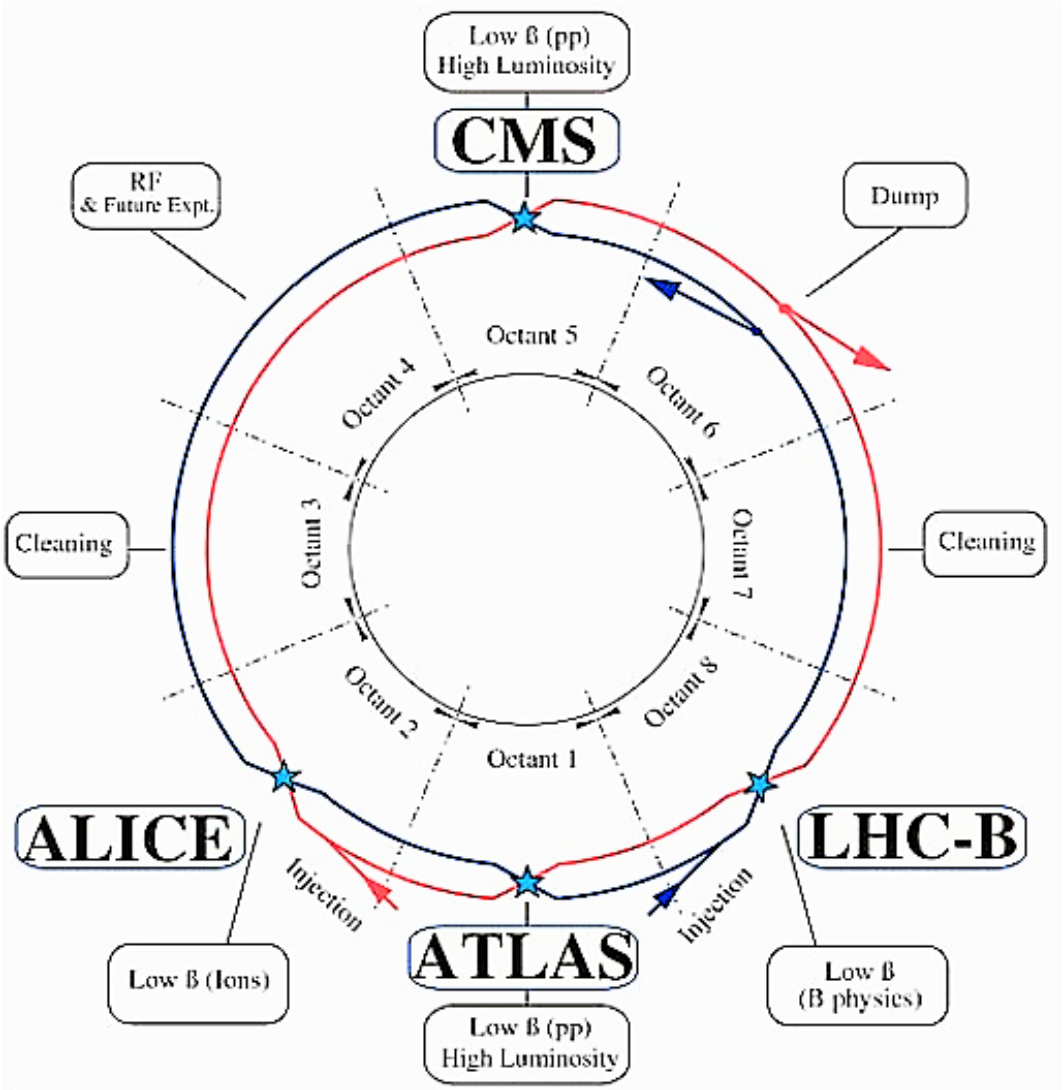

Figure 1.3: Layout of the LHC, focusing on the position of the four main experiments with respect to the interaction points. Radio-frequency cavities and utility insertions are present in octants not covered by experimental setups.

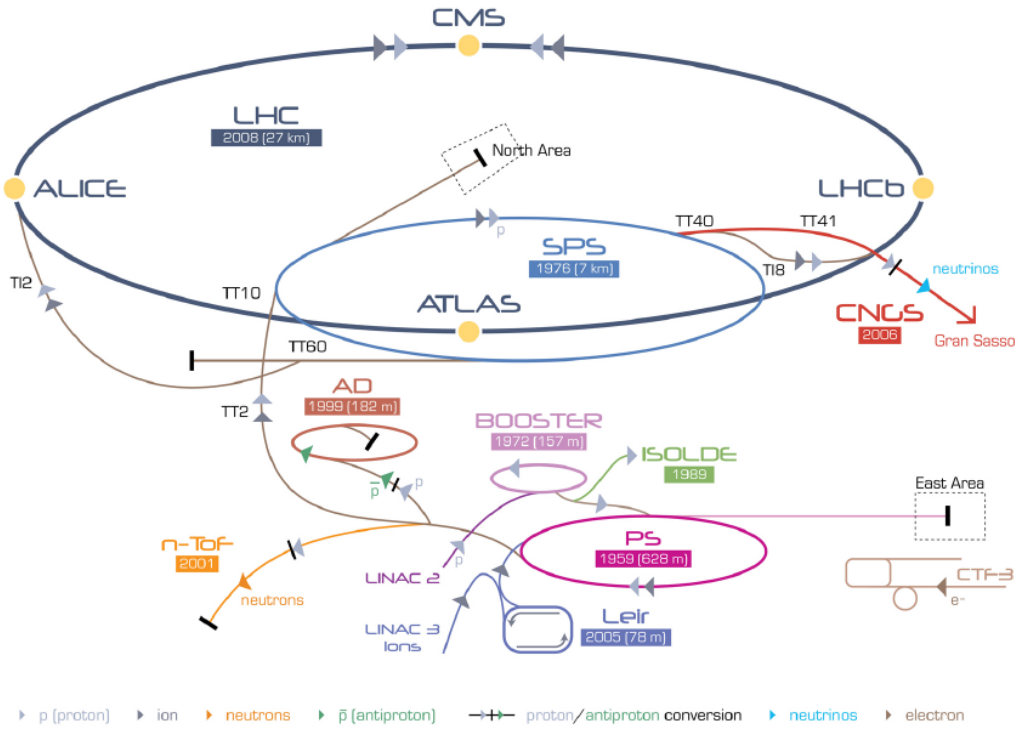

Figure 1.4: The injection chain of the LHC accelerator, each ring representing a different accelerator. The chain starts with the linear accelerator *Linac2*, followed by the *Proton Synchrotron Booster* (*PSB*). The *Proton Synchrotron* (*PS*) further increases the beam energy and feeds the particle packets to the *Super Proton Synchrotron* (*SPS*). After the SPS the beams are injected directly into the LHC.

8.33 T, these ions are accelerated up to an energy of 2.76 TeV/nucleon, yielding a total center-of-mass energy of 1.15 PeV and a nominal luminosity of 1.0 $\times 10^{27} cm^{-2} s^{-1}$. The collision of two counter-rotating proton beams requires opposite magnetic dipole fields in both rings. The LHC is therefore designed as a proton-proton collider with separate magnet fields and vacuum chambers in the main arcs and with common sections only at the insertion regions where experimental detectors are located.
Due to the fact that LHC is built in the LEP tunnel, there is not enough room for two separate rings of magnets and it is therefore necessary to use twin bore magnets, consisting of two sets of coils and beam channels contained within the same mechanical structure and cryostat. The peak beam energy depends on the integrated dipole field around the storage ring; for operations at the design energy of 14 TeV, this implies a peak dipole field of 8.33 T, meaning that superconducting magnet technology is mandatory. Exploiting superconductivity requires niubium-titanium wires for the 1232 magnets of the LHC, be held at temperatures under 2 K by liquid helium that must produced and stored at CERN.

1.3 The LHC roadmap

During the first years of operation, the LHC ramped up its energy from the start-up energy of 900 GeV up to 7 TeV, later upgraded to 8 TeV, which is just over half of the design energy of the machine for proton-proton collisions. In november 2012 the LHC reached a peak instantaneous luminosity of $7.7 \times 10^{33} cm^{-2} s^{-1}$, close to the design luminosity of $10^{34} cm^{-2} s^{-1}$, even though at half the design energy and twice the bunch crossing separation (50 ns instead of 25) [3]. Together with an Ion-Ion collisions run in 2010, this data-taking period is part of the so-called *Run-I*, which has successfully ended in February 2013, bringing the LHC to the first long shutdown necessary for its energy upgrade to the design specification.
The discovery of the Higgs boson was the most relevant of a long series of impressive results achieved by LHC experiments during the first period of data-taking. A first Long Shutdown (LS1), happened from february 2013 to april 2015, focused on the consolidation of the magnet interconnections of the LHC machine. This upgrade was needed to run the LHC at the design energy of 7 TeV per beam and at the design luminosity of $10^{34} cm^{-2} s^{-1}$.
In 2015 the second period of operations of the LHC, called *Run-II*, has started, with the center-of-mass energy increased to 13 TeV and the bunch spacing reduced to 25 ns. Thanks to these changes, it has been possible to achieve and surpass the design luminosity, reaching in June 2017 the record of $1.58 \times 10^{34} cm^{-2} s^{-1}$.
According to the proposed schedule, the LHC is expected to continue providing collisions until 2023, at the end of the *Run-III*.
The scheduled life of the LHC takes into account three long shutdown periods, corresponding to three stages of evolution of the machine performance (see Fig. 1.5):

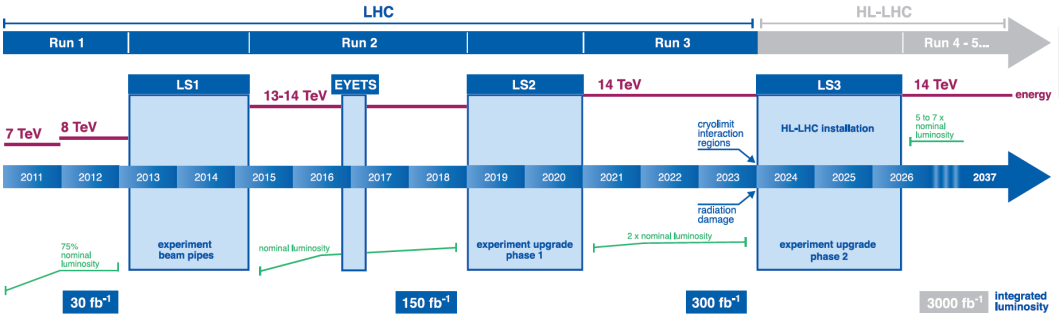

Figure 1.5: The LHC upgrade roadmap. The Run periods (during which data is acquired) are separated by Long Shutdown periods (LS), for hardware maintenance and upgrade. Each period comprising a LS and a Run is called a Phase.

- *Phase-0:* The current status of the LHC, started with the LS1 in February 2013, with the increase of the center-of-mass energy of proton-proton collisions from $\sqrt{s} = 8$ TeV to $\sqrt{s} = 13 - 14$ TeV with a peak luminosity of $L_{peak} = 10^{34} cm^{-2} s^{-1}$ delivering a total of about 100 fb^{-1} of data.
  During the 18 months of LS1, a long list of improvements (such as the magnet interconnections consolidation) has been put in place, in order to bring the machinery to the level needed to sustain 7 TeV beams. Most of the LHC experiments have undergone several consolidation and upgrade works in order to cope with the new running conditions.

- *Phase-1:* In this period, which will start with the second Long Shutdown (LS2) in 2019 and will extend until the end of 2020, the LHC will achieve its design energy and luminosity through a series of improvements, including the installation of a new injector (Linac4).
  Towards the end of this period, the LHC will reach a peak luminosity of $2 - 3 \times 10^{34} cm^{-2} s^{-1}$, beyond the original design value, and is expected to deliver about 300 fb^{-1} of proton-proton collision data. Detailed investigation of the Higgs boson properties and searches for new rare physics phenomena will require to collect more data than the 300 fb^{-1} foreseen by the present LHC schedule.

- *Phase-2 - HL-LHC:* In its ultimate running conditions (after the LS3 in 2024) the LHC is expected to reach a peak luminosity of $5 - 7 \times 10^{34} cm^{-2} s^{-1}$. The performance will improve by gradually exchanging aged components with improved ones, such as new 13 T superconducting magnets; on the other hand, the upgrade will require an optimization of the detectors, as the radiation from the higher luminosity will have a strong impact on the performance of the innermost subdetectors. The upgrade program, called *High-Luminosity LHC* (*HL-LHC*) is expected to deliver an integrated luminosity (at $\sqrt{s} = 14$ TeV) of about 3000 fb^{-1}, further increasing the physics reach of the LHC experiments.

An additional shutdown, the *Extended Year-End Technical Stop* (EYETS), was carried out between the end of 2016 and april 2017 and focused on preparing the LHC machine and the injectors for the future HL-LHC upgrade.

During the LS3 the four main LHC experiments (ALICE, ATLAS, CMS, LHCb) will undergo substantial upgrades in order to meet the strong requirements imposed by the demanding running conditions of the HL-LHC.

1.4 The ATLAS experiment

The ATLAS experiment[2] is a multi-purpose detector built in Point 1 (Fig. 1.3) to probe proton-proton collisions. The detector has cylindrical symmetry and can be divided into a central barrel and two end-cap regions at both side of the detector, as shown in Fig. 1.6. The point where proton-proton collisions occur

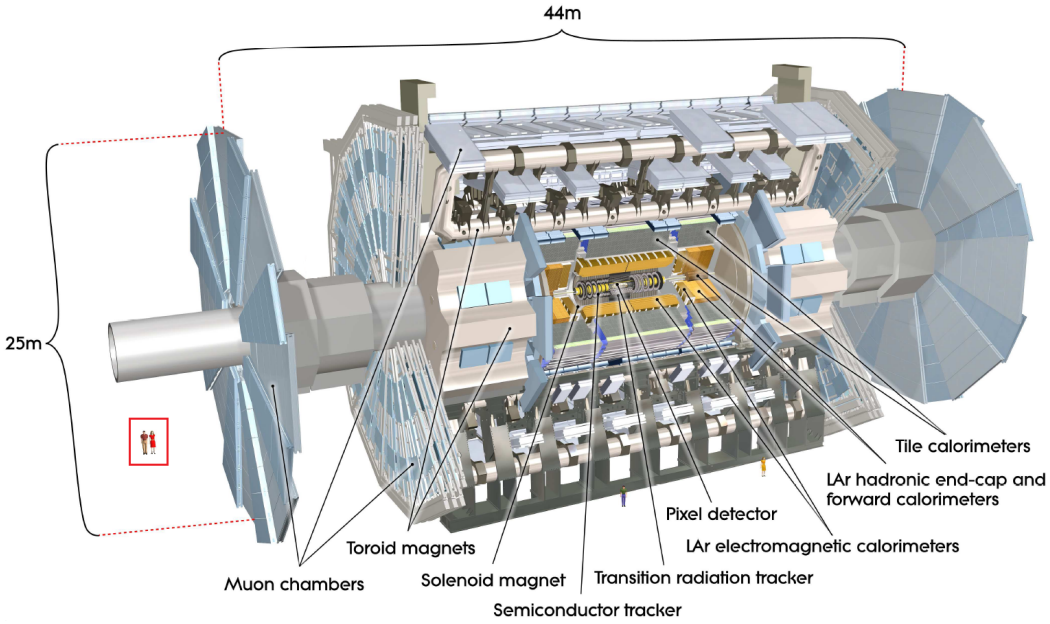

Figure 1.6: View of the ATLAS detector. The system is built with cylindrical symmetry with the beam pipe as the axis. From the innermost (closer to the beam pipe) to the outermost, all the subdetectors of ATLAS are shown. It is possible to compare the size of the ATLAS experiment with the humans in the red box.

inside ATLAS (*IP - Interaction Point*) is defined as the origin of the coordinate system. While the beam line defines the z-axis, the x-y plane transverse to the beam is defined "transverse plane"[3]. Many observables are conserved in the transverse plane, such as transverse momentum p_{T}[4] and transverse energy E_T; we can exploit this conservation for the reconstruction of kinematic quantities such the missing transverse momentum E_{T}^{miss}.
The coordinate system is often described in polar coordinates, namely the azimuthal angle ϕ, measured with respect to the $x - axis$ in the transverse plane, the polar angle θ, measured with respect to the beam axis, and the radial

[2] A Toroidal LHC ApparatuS

[3] The positive x-axis is defined as pointing from the interaction point to the centre of the LHC ring ad the positive y-axis is defined as pointing upwards. The definition of the z-axis sign is right-handed with respect to the x-y plane

[4] $p_{\mathrm{T}} = \sqrt{p_x^2 + p_y^2}$

coordinate r, defined as the distance from the interaction point. Using this coordinate representation it is possible to define Lorentz-invariant variables, such as the *rapidity* (invariant for transformations along the z-axis):

$$y = \frac{1}{2} ln \left[\frac{(E + p_z)}{E - p_z} \right] \tag{1.7}$$

which is reduced, for particles travelling close to the speed of light, to the *pseudorapidity*:

$$\eta = -ln \left(tan \left(\frac{\theta}{2} \right) \right) \tag{1.8}$$

which is only a function of the angular position of the particle, regardless of its nature and energy. It is therefore possible to measure the position of a particle in a new Lorentz-invariant coordinate system, composed by (η, ϕ, z), and to represent a difference in distance between two points (objects) in the $\eta - \phi$ plane as:

$$\Delta R = \sqrt{\Delta\eta^2 + \Delta\phi^2} \tag{1.9}$$

where $\Delta\eta$ and $\Delta\phi$ are respectively the difference in pseudorapidity and azimuthal angle of the two objects.

The high luminosity produced at the LHC enables high precision tests of QCD, electroweak interactions, and flavour physics, as well as searches for new physics beyond the Standard Model. The ATLAS detector already provided a proof of the existence of the Standard Model Higgs boson, together with the CMS experiment, in 2012 [10][11]. Furthermore, searches for Beyond the Standard Model particles, such as squarks and neutralinos of the minimal supersymmetric extension of the Standard Model (discussed in Chapter 3), require increased b-tagging performances (as presented in Chapter 4), which is one of the main reasons for the upgrade of the ATLAS Pixel Detector (as presented in Chapter 2). The production and subsequent decay of supersymmetric particles, such as squarks, would involve cascades which always contain a lightest stable supersymmetric particle (LSP), supposing the R-parity is conserved. As the LSP would interact very weakly with the detector, the experiment would measure a significant E_{T}^{miss} in the final state, while the rest of the cascade would result in a number of leptons and jets.

The requirements of a high luminosity and interaction rate at LHC are needed because of the small cross-sections expected for many of the BSM processes. However, with an inelastic proton-proton cross section of ~ 80 mb (out of a total proton-proton interaction cross section of $\sigma_{tot} = 96$ mb), the LHC produces a total rate of $\sim 10^9$ inelastic events per second at design luminosity.
Most of these collisions are QCD processes, as the nature of proton-proton collisions brings to high jet production cross-sections. The identification of rare new physics process thus requires the precise identification of characteristic experimental signatures, such as high E_{T}^{miss} or particle momentum.
In general, the ATLAS detector is focused on satisfying a wide variety of requirements:

- *Electronics and Sensors:* Due to the experimental conditions at the LHC, the detectors require fast, radiation-hard electronics and sensor elements.

In addition, high detector granularity is needed to handle the particle fluxes and to reduce the influence of overlapping events;

- *Geometric acceptance:* Large acceptance in pseudorapidity with almost full azimuthal angle coverage;
- *Calorimetry:* Good resolution for the electromagnetic calorimeter is required for electron and photon identification. Full coverage hadronic calorimeter is needed for accurate jet and missing transverse energy (E_{T}^{miss}) measurement;
- *Charged particle reconstruction:* Good charged-particle momentum resolution and reconstruction efficiency in the inner tracker are essential. For offline tagging of τ leptons and b-jets, vertex detectors close to the interaction region are required to be able to resolve secondary vertices;
- *Muon identification:* muon needs to be identified with momentum resolution over a wide ranges of p_{T};
- *Trigger:* Efficient triggering system on a wide spectrum of transverse momentum objects with good background rejection, in order to achieve an acceptable trigger rate for most processes of interest;

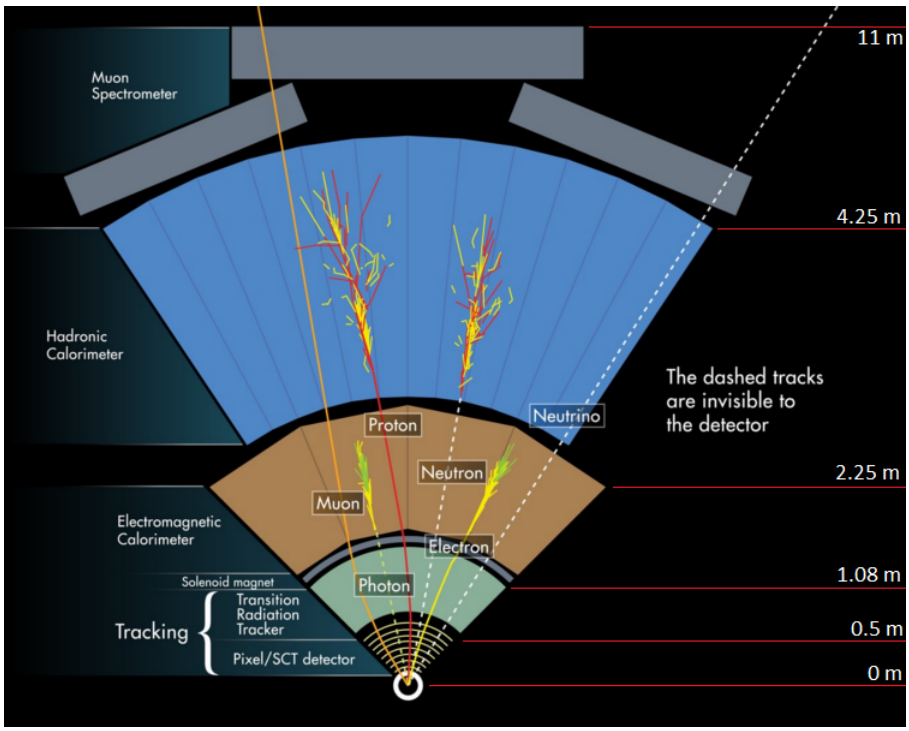

Figure 1.7: Section of the ATLAS detector, highlighting the subdetectors and their interaction with the particles produced in the collisions. On the bottom, a vertical section of the pipeline in which the particles travel near the speed of light, colliding inside the ATLAS detector.

These requirements cannot be satisfied by a single detector and proved to be necessary the creation of an interconnected system of cooperating subdetectors, each focused to a specific role. As presented in Fig. 1.7, particles created

Detector component	**Required resolution**	η **coverage** (measurement)	η **coverage** (Trigger)
Tracking	$\frac{\sigma_{p_T}}{p_T} = 0.05\% p_T \oplus 1\%$	$\|\eta\| < 2.5$	
EM calorimetry	$\frac{\sigma_E}{E} = \frac{10\%}{\sqrt{E}} \oplus 0.7\%$	$\|\eta\| < 3.2$	$\|\eta\| < 2.5$
Hadronic calorimetry (jets)			
barrel and end-caps	$\frac{\sigma_E}{E} = \frac{50\%}{\sqrt{E}} \oplus 3\%$	$\|\eta\| < 3.2$	$\|\eta\| < 3.2$
forward	$\frac{\sigma_E}{E} = \frac{100\%}{\sqrt{E}} \oplus 10\%$	$3.1 < \|\eta\| < 4.9$	$3.1 < \|\eta\| < 4.9$
Muon spectrometer	$\frac{\sigma_{p_T}}{p_T} = 10\%\ at\ p_T = 1\ TeV$	$\|\eta\| < 2.7$	$\|\eta\| < 2.4$

Table 1.2: Requirements for each of the ATLAS detector subsystem. The minimal resolution required to achieve the expected results is presented for the pseudorapidity region the subdetector is expected to cover. Pseudorapidity requirements for the trigger system of each subdetector are also presented.

in the interaction point inside ATLAS travel trough multiple subdetectors, interacting differently with each of them. The innermost detector encountered by the produced particles is the *Inner Detector* (*ID*), located near the beam pipe and close to the interaction point. It is designed to reconstruct the passage of charged particles and is composed of multiple superimposed layers (with cylindrical symmetry around the beam pipe).

In order to measure the particle charge and momentum, the innermost detector is immersed in a 2 T solenoidal field created by a thin superconducting solenoid, which bends the trajectory of charged particles. Pattern recognition, momentum and vertex measurements as well as electron identification are achieved with a combination of discrete, high-resolution semiconductor pixel and strip detectors in the inner part of the tracking volume, and straw-tube tracking detectors with the capability to generate and detect transition radiation in its outer part.

Photons and electrons are discriminated thanks to *Electromagnetic Calorimeter* (*ECAL*), which provides a great energy and position resolution for these particles. A high spatial resolution proved to be of primary importance in the Higgs discovery, acting as discriminant between the $\pi^0 \to \gamma\gamma$ background and the $H \to \gamma\gamma$ signal.
Jets originating from hadronic showers are measured thanks to the *Hadronic Calorimeter* (*HCAL*) which also provides an important contribution to the E_T^{miss} reconstruction, making this subdetector an essential component in searches for new physics which are often characterised by a high missing momentum. The magnetic field is generated, around the calorimeters, by three large superconducting toroids (one barrel and two end-caps) arranged with an eight-fold azimuthal symmetry.

The calorimeter is surrounded by the muon spectrometer; multiple-scattering effects are minimised, and excellent muon momentum resolution is achieved with three layers of high precision tracking chambers. A recap of the performance requirements of the ATLAS subdetectors is presented in Tab. 1.2.

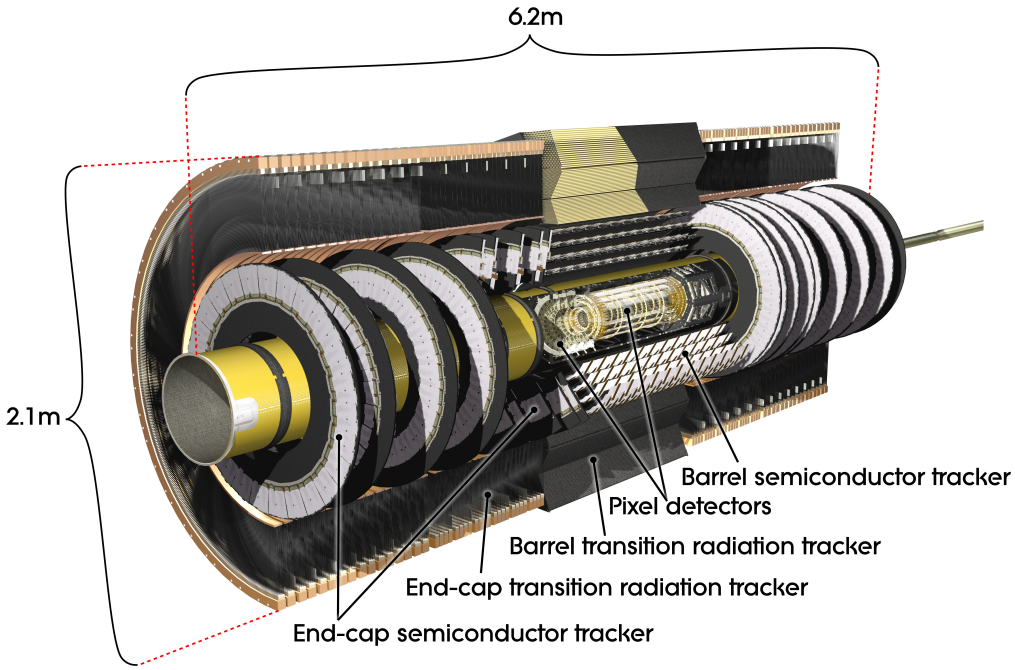

Figure 1.8: The Inner Detector of the ATLAS experiment, composed by the Pixel Detector Layers (IBL, B-Layer, Layer-1, Layer-2) and the Trackers (Semi Conductor Tracker, Transition Radiation Tracker).

1.5 ATLAS subdetectors

The drawback of the high number of collisions created by the LHC is the necessity to identify a huge ($\mathcal{O}(10^3)$) amount of particles emerging from the interaction point every 25 ns within a narrow cone of $|\eta|< 2.5$, creating a very large track density in the detector. To achieve the momentum and vertex resolution requirements imposed by the benchmark physics processes, high-precision measurements must be made with fine detector granularity. The ATLAS Inner Detector combines high-resolution detectors at the inner radii with continuous tracking elements at the outer radii, all contained in the Central Solenoid, which provides a nominal field of 2 T (Fig. 1.8). In the barrel region, they are arranged on concentric cylinders around the beam axis, while in the end-cap regions they are located on disks perpendicular to the beam axis. The highest granularity is achieved around the vertex region using silicon pixel detectors.

– *Pixel Detector (PD):* the innermost part of the ID, it covers the region $|\eta|< 2.5$ and is part of the precision tracking detector of the ID together with the Semi Conductor Tracker. The PD is composed of 3 + 1 layers of pixel matrices: the three original layers, called *B-Layer*, *Layer-1* and *Layer-2* (ordered by their distance from the IP), are segmented in the $R-\phi\times z$ plane by 50×400 μm^2 silicon pixels, grouped in readout chips called $FE-I3$. The three layers are located respectively at a distance of 50.5, 88.5, 122.5 mm from the pipe.

  In 2014 a fourth layer, the *Insertable B-Layer* (*IBL*) was added as the innermost layer, at a distance of 33.25 mm from the beam pipe, provid-

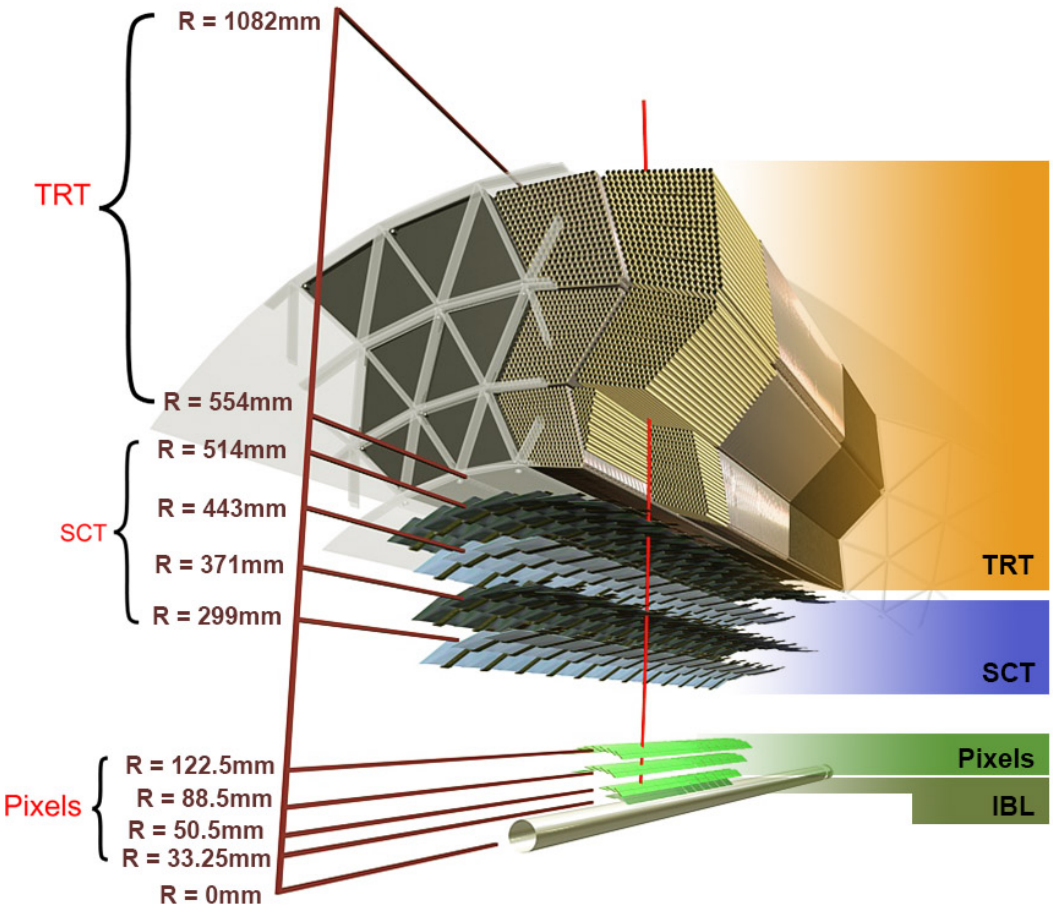

Figure 1.9: Section of the ATLAS Internal Detector, showing the distribution and distance from the beam pipe of each sub-detectors.

ing better track and secondary vertex reconstruction, as well as higher acquisition rate capability. This fourth layer uses more advanced components and is expected to replace the B-Layer, which sustained high radiation damage due to his proximity to the beam pipe. The IBL is based on new FE-I4 modules with faster readout and smaller pixels, for higher granularity. A complete overview of the PD readout and upgrade after the IBL insertion will be the focus of the next chapter.

– *Semi Conductor Tracker (SCT):* The SCT system is designed to provide high precision measurements per track in the intermediate radial range, contributing to the measurement of momentum, impact parameter and vertex position. It is composed of four cylinders in the barrel region, covering the pseudorapidity range $|\eta| < 1.1-1.4$ (depending on the cylinder), and two end caps components, each consisting of 9 disks and covering $1.1 - 1.4 < |\eta| < 2.5$. While pixels, thanks to their geometry, offer better 2-dimension coverage, microstrips have a better resolution along one privileged coordinate. In the barrel SCT eight layers of silicon microstrip detectors provide precision point in the $R - \phi$ and z coordinates, using small angle stereo to obtain the z-measurement. The spatial resolution of the SCT is 17μm along the $R-\phi$ direction and 580 μm in the z direction.

  The silicon detector is composed by 6.36×6.40 cm^2 modules, with 780 readout strips of 80 μm pitch. The barrel modules are mounted on carbon-fibre cylinders at radii of 299, 371, 443 and 514 mm. The end-cap modules are very similar in terms of construction, but use tapered strips with one set aligned radially.

– *Transition Radiation Tracker (TRT):* The outermost part of the ID, the Transition Radiation Tracker is composed by 1.43 m long cylindrical barrel layers and two end-caps components. Both the barrel and the end-caps use 420,000 carbon-polyimide straw detectors ($\sim$50 000 double straws in the barrel and 320,000 in the end-caps) filled with a $Xe(70\%)CO_2(27\%)O_2(3\%)$ gas mixture. The particles produced in the *pp* collision travel at relativistic speed trough the straw tubes, emitting a transition radiation whose intensity is a function of the relativistic gamma factor of the particle $\gamma = \frac{E}{m}$ This information can be used, together with the energy deposit the particle leaves in the calorimeter, for particle identification, in particular for $e/\pi^{\pm}$ separation.

  While the TRT cannot compete with the silicon-based PD and SCT in terms of resolution, the high number of measurements allows the TRT significantly contribute to the track definition and consequently to the momentum resolution.

The reconstruction of the energy of a crossing particle is made by the calorimeters. The entire calorimeter detector is divided in multiple parts, each dedicated to a different type of particle, and covers the range $|\eta| < 4.9$. Calorimeters must provide good containment for electromagnetic and hadronic showers, as the particle (or jet) must lose the entirety of its energy inside the detector, making calorimeter depth an important design consideration. The pseudora-

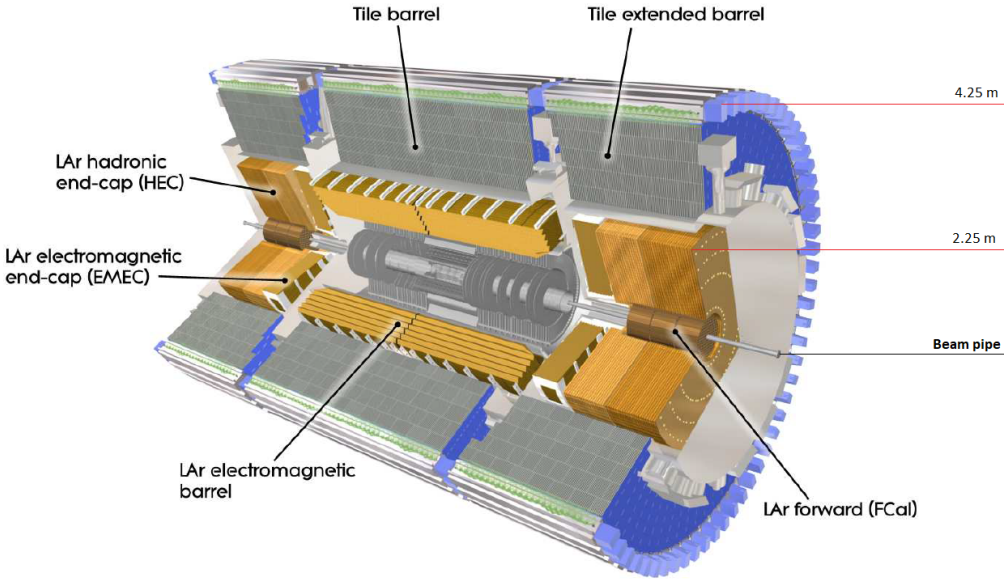

Figure 1.10: View of the ATLAS calorimeter system, for measures of the energies and positions of charged and neutral particles. It consists of a Liquid Argon (LAr) electromagnetic calorimeter and an Hadronic Calorimeter. Interactions in the absorbers transform the energy into a "shower" of particles that are detected by the sensing elements.

pidity coverage and granularity of the ATLAS calorimeters are presented in Tab. 1.3.

LAr electromagnetic calorimeter The high-granularity liquid-argon (LAr) electromagnetic sampling calorimeter is focused at the destructive measure of the electrons and photons energy. It covers the pseudorapidity range $|\eta|< 3.2$ and has an excellent performance in terms of energy and position resolution. The Electromagnetic Calorimeter is divided into a barrel (covering $|\eta| < 1.475$) and two end-caps (covering $1.375 < |\eta| < 3.2$); each end-cap calorimeter is mechanically divided in two coaxial wheels: an outer wheel covering the region $1.375 < |\eta| < 2.5$ and an inner wheel covering $2.5 < |\eta| < 3.2$.
Since the EM showers are contained ($> 99\%$ of the energy) within 20 radiation lenghts (X_0), the total thickness of the EM calorimeter is > 22 radiation lengths in the barrel and > 24 X_0 in the end-caps. Over the η region matched to the inner detector, the fine granularity of the EM calorimeter is ideally suited for precision measurements of electrons and photons. The coarser granularity of the rest of the calorimeter is sufficient to satisfy the physics requirements for jet reconstruction and E_{T}^{miss} measurements.

The EM calorimeter is based on a lead-LAr detector with accordion-shaped kapton electrodes and lead absorption plates over its full coverage. The liquid argon was chosen as an active medium because of its intrinsic radiation hardness and good energy resolution. The advantage of the accordion geometry is that it provides complete ϕ symmetry without azimuthal cracks. Over

		η coverage	Granularity ($\Delta\eta \times \Delta\phi$)
EM calorimeter			
Presampler	*barrel*	$\lvert\eta\rvert < 1.54$	0.025×0.1
	end-caps	$1.5 < \lvert\eta\rvert < 1.8$	0.025×0.1
Sampling 1	*barrel*	$\lvert\eta\rvert < 1.4$	0.003×0.1
		$1.4 < \lvert\eta\rvert < 1.475$	0.025×0.025
	end-caps	$1.375 < \lvert\eta\rvert < 2.5$	0.003 - 0.025×0.1
		$2.5 < \lvert\eta\rvert < 3.2$	0.1×0.1
Sampling 2	*barrel*	$\lvert\eta\rvert < 1.4$	0.025×0.025
		$1.4 < \lvert\eta\rvert < 1.475$	0.075×0.025
	end-caps	$1.375 < \lvert\eta\rvert < 2.5$	0.050 - 0.025×0.025
		$2.5 < \lvert\eta\rvert < 3.2$	0.1×0.1
Sampling 3	*barrel*	$\lvert\eta\rvert < 1.35$	0.05×0.025
	end-caps	$1.5 < \lvert\eta\rvert < 2.5$	0.05×0.025
Tile calorimeter			
Sampling 1-2	*barrel*	$\lvert\eta\rvert < 1.0$	0.1×0.1
	extended-barrel	$0.8 < \lvert\eta\rvert < 1.7$	0.1×0.1
Sampling 3	*barrel*	$\lvert\eta\rvert < 1.0$	0.2×0.1
	extended-barrel	$0.8 < \lvert\eta\rvert < 1.7$	0.2×0.1
Hadronic end-cap			
Sampling 1-4		$1.5 < \lvert\eta\rvert < 2.5$	0.2×0.2
		$2.5 < \lvert\eta\rvert < 3.2$	0.1×0.1
Forward			
Sampling 1-3	$3.1 < \lvert\eta\rvert < 4.9$	0.2×0.2	

Table 1.3: Pseudo-rapidity coverage and granularity of the ATLAS calorimeter subdetectors.

the region $|\eta| < 2.5$, which is intended to be used for precision physics, the EM calorimeter is segmented in depth in three sections. The first layer of the calorimeter, called the η-strip layer, is finely granulated in η in order to allow for a better separation between photons (which results in a single energy deposition) and neutral pions (which results into two very close deposits of energy from the $\pi^0 \to \gamma\gamma$ decay). The resolution achievable in the barrel EM calorimeter is able to discriminate photons and electrons in a wide energy range ($\sim$5 GeV to $\sim$5 TeV). From fits based on electron beam irradiations, the resolution was measured as:

$$\frac{\sigma(E)}{E} = \frac{9.4\%}{\sqrt{E(\text{GeV})}} \oplus 0.1\% \tag{1.10}$$

where 9.4% is the stochastic term and 0.1% is the constant term. The energy response is also linear within $\pm$0.1%. Similar results have been obtained for the end-cap EM calorimeters.
At the transition between the barrel and the end-cap calorimeters, at the boundary between the two cryostats, the amount of material in front of the calorimeter reaches a localized maximum of about 7 X_0. For this reason, the region $1.37 < |\eta| < 1.52$ is not used for precision measurements involving photons and electrons.

Hadronic calorimeter The focus of the HCAL is the energy measurement of jets originated from hadronic processes, as well as the determination of the missing transverse momentum. The hadronic calorimetry in the range $|\eta| < 1.7$ is provided by a scintillator-tile calorimeter, the *Hadronic Tile Calorimeter* (*HTC*), which is separated into a large barrel (covering the region $|\eta| < 1.0$ for a total of 1.4 interaction lenghts) and two smaller extended barrel cylinders (covering the region $0.8 < |\eta| < 1.7$, for a total of 4.0 and 1.8 interaction lenghts, respectively), one on either side of the central barrel. In the end-caps ($|\eta| > 1.5$), LAr technology is also used for the *Hadronic End-Caps Calorimeters* (*HEC*) (12 interaction lenghts), matching the outer $|\eta|$ limits of the end-cap electromagnetic calorimeters. Finally, the LAr *Forward Calorimeters* (*FCAL*) (2.6 interaction lenghts) provide both electromagnetic and hadronic energy measurements, extending the pseudorapidity coverage up to $|\eta| = 4.9$.
The HTC uses steel as the absorber and scintillating tiles as active material. Two sides of the scintillating tiles are read out by wavelength shifting fibres into two separate photomultiplier tubes. The energy response to isolated charged pions of the combined LAr and tile calorimeter was measured with test beams as:

$$\frac{\sigma(E)}{E} = \frac{52\%}{\sqrt{E(GeV)}} \oplus 3\% \tag{1.11}$$

For the HEC, LAr technology is used as the EM calorimeter in the barrel region, while copper is used as passive material instead of lead and a flat-plate geometry was chosen. The energy resolution for isolated pions is:

$$\frac{\sigma(E)}{E} = \frac{71\%}{\sqrt{E(GeV)}} \oplus 1.5\% \tag{1.12}$$

Finally, the FCAL also uses LAr as active material and copper as passive absorber for the first layer and tungsten for the second and third layers. As a result of test beams, the energy response to isolated pions is expressed by:

$$\frac{\sigma(E)}{E} = \frac{94\%}{\sqrt{E(GeV)}} \oplus 7.5\% \tag{1.13}$$

While most of the SM particles interacts with either the Calorimeter system, muons usually pass through it totally undetected and is therefore necessary a dedicated subdetector for the study of their signature. The ATLAS Muon Spectrometer has been designed to achieve momentum measurement with high efficiency and resolution over a wide range in transverse momentum, pseudo-rapidity and azimuthal angle, while simultaneously providing triggering capabilities.
The Muon Spectrometer is divided in two different groups of subdetectors: the Precision Chambers (*Monitored Drift Tubes* and *Cathode Strip Chambers*) are focused on precision measurement of muon momentum, while the Trigger Chambers (*Thin Gap Chambers* (TGC) and *Resistive Plate Chambers* (RPC)) provide online trigger.
The measurement is based on the magnetic deflection of muon tracks in the large superconducting air-core toroid magnets, instrumented with separate trigger and high-precision tracking chambers. Over the range $|\eta|<1.4$, magnetic bending is provided by the large barrel toroid, while for $1.6<|\eta|<2.7$, muon tracks are bent by two smaller end-cap magnets inserted into both ends of the barrel toroid. Over $1.4<|\eta|<1.6$ (transition region) a combination of barrel and end-cap fields provides magnetic deflection.

Precision Chambers

Monitored Drift Tubes (MDT): MDT are drift chambers of two multilayer drift tubes, with 30 mm diameter aluminium walls filled with an Argon-mixture gas (93%Ar-7%CO_2), focused on precise measurement of the z coordinate in the barrel region, covering the region $|\eta|< 2$. By measuring the drift time in a single tube it is possible to reconstruct the hit position of the particle, with a space resolution of 80 μm.

Cathode Strip Chambers (CSC): The CSC are multi-wire chambers with strip cathodes for the measurement of muon momenta in the pseodurapidity region $1.0 < |\eta|< 2.7$. The CSC wires are composed of parallel anodes which are perpendicular to 1 mm large strips of opposite polarity. The anode-cathode distance equals the distance between the anode wires, typically 2.5 mm, with a time resolutions of about 7 ns and a corresponding spatial resolution of 60 μm in the ϕ direction and $\mathcal{O}(10^{-2})$m in η.

Trigger Chambers

Thin Gap Chamber (TGC): The end-cap region of the trigger chamber is equipped with very thin multiwire chambers, the TGC. The anode-catode spacing is smaller than the anode-anode spacing, leading to a very short drift time ($<$ 20 ns). To satisfy the requirement of 4 ns time

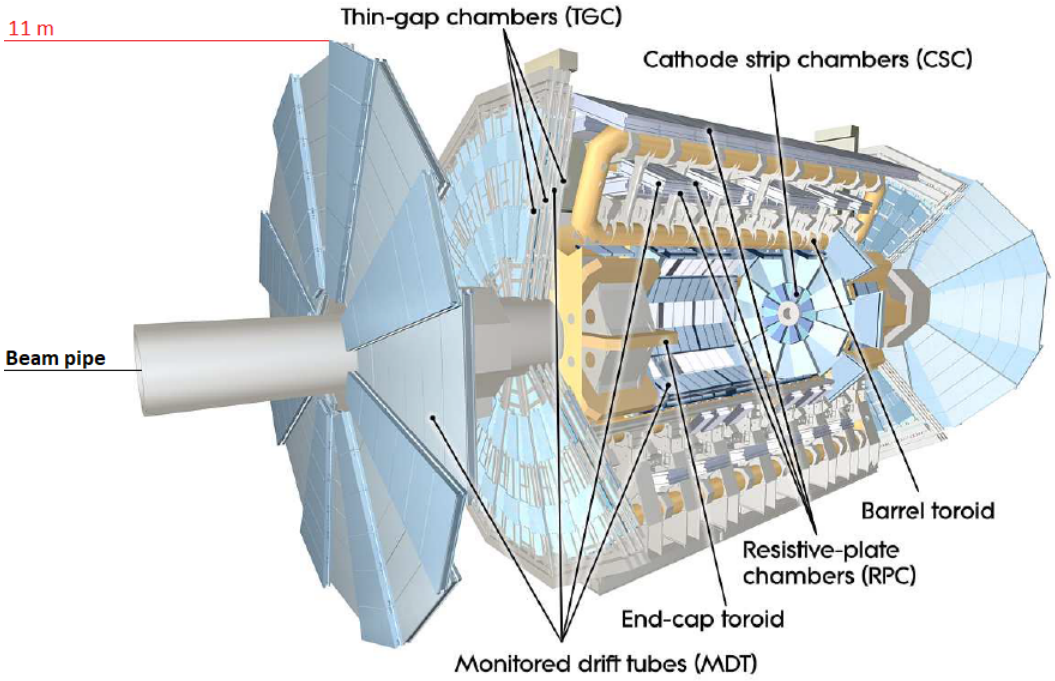

Figure 1.11: View of the ATLAS muon detector system. It is divided in two different groups of sub-detectors, the Precision Chambers (Monitored Drift Tubes and Cathode Strip Chambers) for muon moment and Trigger Chambers (Thin Gap Chambers, Resistive Plate Chambers) for online data-acquisition triggering.

resolution and a good performance in a high particle flux, the TGC works in saturation regime. TGC are filled with a highly quenching gas mixture (55% CO_2 and 45% n-pentane C_5H_{12}). The spatial resolution of these detectors is 4 mm in the radial direction and 5 mm in the ϕ coordinate. The TGC are also used to improve the measurements along the ϕ coordinate obtained from the precision chambers.

Resistive Plate Chambers (RPC): The RPC are gaseous parallel electrode-plate detectors, with a spatial resolution of 1 cm in two coordinates and an excellent time resolution of 1 ns. Each of the two rectangular layers which form the RPC is read out by two orthogonal series of pick-up strips: the η coordinate is measured by strips parallel to the MDT wires, while the ϕ coordinate is measured by orthogonal strips. This sub-detector works in the avalanche regime: when a charged particle passes inside the chamber, the primary ionization electrons are multiplied into avalanches by a high electric field, typically 4.9 kV/mm. The signal is read out on both sides of the chamber through capacitive coupling strips. The RPC and TGC trigger chambers cover the range $|\eta| < 2.4$.

The ATLAS experiment uses a two staged trigger system (shown in Fig. 1.12) to identify events of interest. It consists of a hardware-based *First-Level Trig-*

ger (*L1*) and a software based *High-Level Trigger* (*HLT*). The massive data

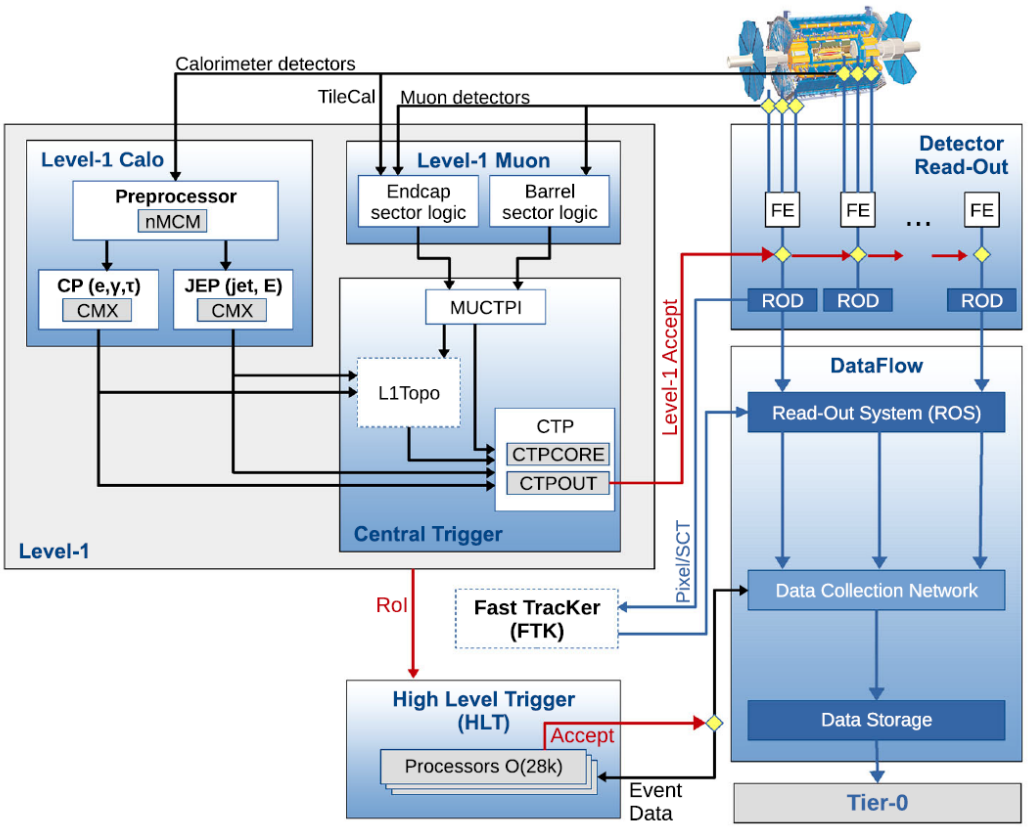

Figure 1.12: Schematic layout of the ATLAS trigger and data acquisition system in Run-II. The Level-1 trigger uses information from multiple subsystems to quickly identify events of interest, while the more refined High-Level Trigger exploits informations from all the subsystems. Accepted data is then sent to the Read-Out system to be stored.

rate of 40MHz (as the collisions happens every 25 ns) is reduced to 100kHz by L1. Since the transit and processing time is around 2.5 μs, the detector data must be time stamped and held in the buffers of the front-end circuit. The L1 uses information from dedicated muon trigger and from the calorimeters, as the only signatures which can be selected in the L1 trigger are high-p_{T} muons, electrons/photons, jets, τ-leptons decaying into hadrons and missing transverse energy. No information coming from the tracking devices can be used at L1.
The second stage of the trigger system is composed of two levels (*L2* and *Event Filter*) collectively known as HLT and further reduces the event rate to a level of $0.4 \div 1$ kHz. The HLT is a software based trigger and uses offline-like reconstruction algorithms, exploiting informations from all sub-detectors in regions of interest (areas of the detector identified as interesting by the L1 trigger) around the Level-1 objects in full granularity. The use of regions of interest allows to have a fast execution time keeping a high selection efficiency.

Chapter 2

ATLAS Pixel Detector upgrade for Run-II

The continuous challenge towards high luminosities and center-of-mass energies brings along the necessity of a constant development of the hardware used in the study of high energy physics. Besides this, a natural evolution of the machinery is also necessary, both to increase its efficiency by replacing older solutions with bleeding-edge technology and as a form of maintenance for damages created by the extreme environment. The latter point is particularly true for the ATLAS pixel detector which, being the subsystem closest to the interaction point, is subject to heavy radiation doses.
A brief overview of the structure and limits of the Run-I pixel detectors is hereby presented, followed by an extended exposition on how these limits have been overcame with the upgrade for Run-II. This upgrade process was divided in two main phases: the construction of a new detector layer, the Insertable B-Layer, and the upgrade of the previous pixel layers (B-Layer, Layer-1 and Layer-2) using IBL technology.

2.1 Pixel Detector in Run-I

Before the 2013 shutdown, the original pixel detector consisted of three layers: B-Layer, Layer-1 and Layer-2. Their construction exploited the most advanced technology available at the time, in order to achieve the highest spatial resolution and radiation hardness. The Run-I pixel detector (presented in Tab. 2.1) is composed by a total of 112 structures called staves, each divided in 13 Front-End modules. The modules are composed by a sensor part, 16 Front

Layer	Mean Radius [mm]	Number of staves	Number of modules	Number of channels	Active Area $[m^2]$
B	50.5	22	286	13,178,880	0.28
1	88.5	38	494	22,763,520	0.49
2	122.5	52	676	31,150,080	0.67
Total	/	112	1456	67,092,480	1.45

Table 2.1: Summary of the construction parameters of the three original layers (B-Layer, Layer-1 and Layer-2) of the ATLAS Pixel detector.

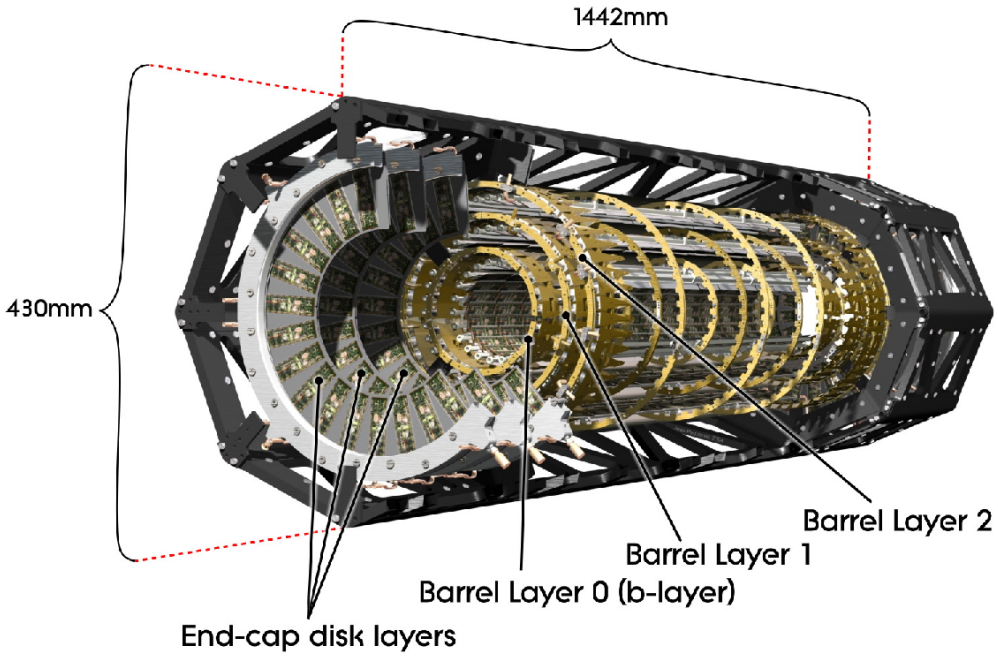

Figure 2.1: Schematic view of the ATLAS pixel detector during Run-I. From the innermost to the outermost, Layer-B, Layer-1 and Layer-2 are shown. To increase pseudorapidity coverage, additional End-cap disk layers have been built.

End chips called *FE-I3*, a flex-hybrid and a Module Controller Chip (MCC). The sensor is divided in a matrix of 47,232 pixels; 41,984 of them have a size of 400 $\times$ 50 μm, while the remaining are slightly bigger (600 $\times$ 50μm) and are located on the sides in order to minimize signal loss in the zone between two modules. Each pixel is composed of a reverse biased n-doped crystalline semiconductor with a p-doped well. Due to the reverse bias, the depletion region is free of charges until a ionizing particle passes, freeing electrons and holes. Before the recombination can take place, the electric field separates electrons and holes, leading them on the metal contacts where a charge amplifier collect them.

Particles passing through the pixel detector generate a signal in the silicon sensor, which is read-out by the FE-I3 chip, which is bump-bonded on the sensor. Each FE-I3 chips is 195 μm thick and 1.09 $\times$ 0.74 cm large, counting 3.5 millions of transistors manifactured in 250 nm CMOS technology. The analog signals are then digitized and buffered inside the End of Columns electronic waiting for a trigger. When the trigger arrives, End of Columns signals departs toward the MCC that takes care of distributing timing, trigger, reset and calibration signals while also taking care of ordering the 16 FE-I3 EoC data and producing an event for the Read-Out Driver board. The electrical signal is then converted to optical and sent to the read-out electronics via optical fibres.

2.2 Limits of the Run-I Pixel Detector

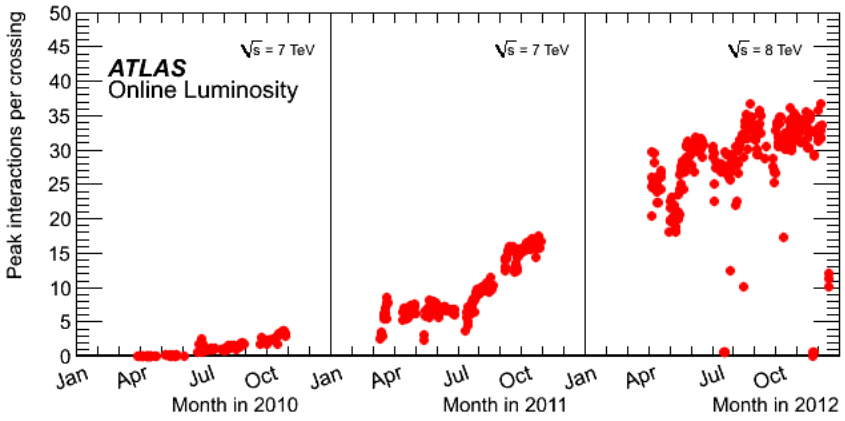

Figure 2.2: The maximum mean number of events per beam crossing versus day during the *pp* runs of 2010, 2011 and 2012. The online luminosity measurement is used for this calculation as for the luminosity plots. Only the maximum value during stable beam periods is shown

In a complex system such as the LHC it is essential to predict the impact of the evolution of each aspect of the experimental setup. The increased beam luminosity exploited in Run-II by the LHC has posed major challenges for many ATLAS sub-systems.
Each bunch-crossing, a number of proton-proton collisions, referred to as "pile-up", takes place in the interaction point. If at least one of these interactions passes the trigger selections, signals from detector cells hit by particles originating from the collisions must be revealed.
By increasing the beam luminosity, the average pile-up is expected to grow as well, thus incrementing the quantity of data to be read-out from the sub-detectors. The number of interactions per beam crossing could be summarized as $\mu = \mathcal{L}_{bunch} \times \sigma_{inel}/f_r$ where $\mathcal{L}_{bunch}$ is the per-bunch instantaneous luminosity, σ_{inel} is the inelastic cross-section at 13 TeV (which is taken to be 80 mb) and f_r is the LHC revolution frequency of 11.245 kHz.

During 2011, the number of proton-proton collisions per bunch crossing increased from 5 to 15, and during 2012 from 10 to almost 35 (Fig. 2.2); the increase in luminosity led to an important rise of the pile-up during Run-II, as shown in Fig. 2.3 and in 2017, the pile-up reached values as high as 70; Fig. 2.4 illustrates the increase of pile-up during Run-II as a function of the total integrated luminosity.

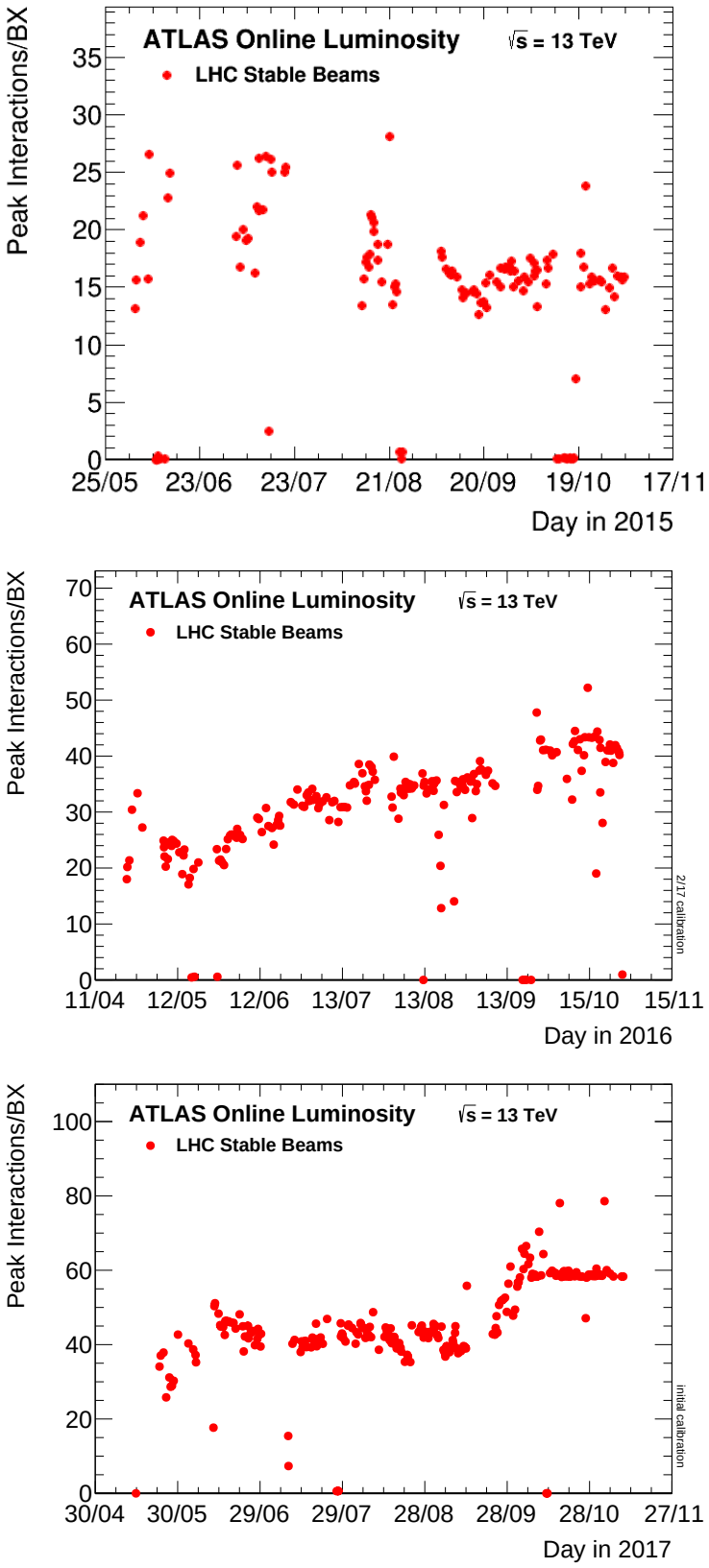

Figure 2.3: The maximum number of inelastic collisions per beam crossing (μ) during stable beams for pp collisions with a center-of-mass energy $\sqrt{s} = 13$ TeV is shown for each fill in 2015, 2016 and 2017. The number of interactions shown is averaged over all colliding bunch pairs, and only the peak value per fill during stable beams is shown.

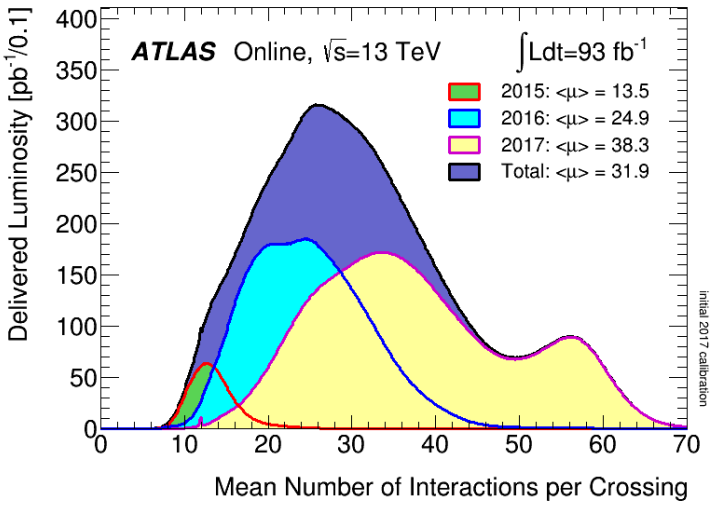

Figure 2.4: Luminosity-weighted distribution of the mean number of interactions per crossing for the 2015 (green),2016 (light blue) and 2017 (light yellow) *pp* collision data at 13 TeV centre-of-mass energy. The luminosity-weighted distribution of the mean number of interactions per crossing during the entire Run-II is shown in purple. All data delivered to ATLAS during stable beams is shown, and the integrated luminosity and the mean μ value are given in the figure. The luminosity shown represents the initial 13 TeV luminosity estimate and includes all 13 TeV *pp* data recorded in 2015,2016 and 2017.

As the luminosity delivered by the LHC kept increasing even beyond the design expectation value, several scenarios of bunch spacing (25 ns or 50 ns) and number of pile up events have been studied to understand the detector performance and limitations. The increased luminosity also had an important effect on the data throughput [1] that the read-out system must acquire every second. Reaching readout bandwidth limitations leads to pixel detector inefficiencies and instabilities in tracking.
Based on the experience achieved during Run-I, extrapolations have been calculated for the occupancy of the Pixel Detector layers modules, called *pixel occupancy*. Tab. 2.2 shows the outcome in terms of occupancy for the different scenarios.

	μ	B-Layer	Layer 1	Layer 2	Disks
50 ns	37	0.17	0.07	0.04	0.06
25 ns	25	0.15	0.06	0.04	0.05
	51	0.27	0.11	0.07	0.09
	76	0.39	0.16	0.10	0.13

Table 2.2: Extrapolated pixel occupancies per column pair and bunch crossing for each Layer of the Run-I pixel detector. Run-I scenarios with both 50 and 25 ns of bunch-crossing have been calculated. Collisions with 25 ns bunch-crossing have a center-of-mass energy of 13 TeV. Orange values are limit values, meaning the readout system is operating at near full-capacity.

Using these extrapolated pixel occupancies studies, it was possible to derive the *link occupancy*, defined as the ratio between data throughput and read-out bandwidth, by taking into account the trigger rate, data word length, etc. This process has been reiterated for several scenarios of LHC operation. Tab. 2.3 and Tab. 2.4 show the result of this calculation in different L1 trigger rate scenarios. A link occupancy higher than 1 (that is, 100% of the bandwidth is used), leads to desynchronization problems.

It can be observed that Layer-2 was expected to suffer link occupancy limitations already during Run-II. Layer-1 was also expected to start to be limited during operation after LS2.
The effect of this readout limitation was already partially seen in Run-I; Fig. 2.5 shows that a number of pixel modules suffered from desynchronization problem already in 2012, with Layer-2 performing the worst due to limitations in readout speed. With the increased luminosity in 2015/16 and even more by 2018, this effect was expected to grow dramatically, leading to the potential loss of readout capability for the pixel detector.

[1] the amount of data sent each second by the detector to the acquisition system

	μ	B-Layer	Layer 1	Layer 2	Disks
50 ns	37	39%	34%	52%	30%
25 ns	25	35%	31%	48%	27%
	51	53%	59%	66%	39%
	76	71%	73%	111%	64%

Table 2.3: Link occupancy for a L1-trigger rate of 75 kHz. The link occupancy is defined as the ratio between the detector data throughput and the bandwidth of the readout system. Orange values are limit values, meaning the readout system is operating at full-capacity. Red values shows scenarios in which the readout system bandwidth is too low to cope with the data throughput, leading to de-synchronization errors.

	μ	B-Layer	Layer 1	Layer 2	Disks
50 ns	37	51%	45%	69%	40%
25 ns	25	47%	42%	65%	37%
	51	71%	67%	88%	52%
	76	95%	97%	148%	75%

Table 2.4: Link occupancy for a L1-trigger rate of 100 kHz. The link occupancy is defined as the ratio between the detector data throughput and the bandwidth of the readout system. Orange values are limit values, meaning the readout system is operating at full-capacity. Red values shows scenarios in which the readout system bandwidth is too low to cope with the data throughput, leading to de-synchronization errors.

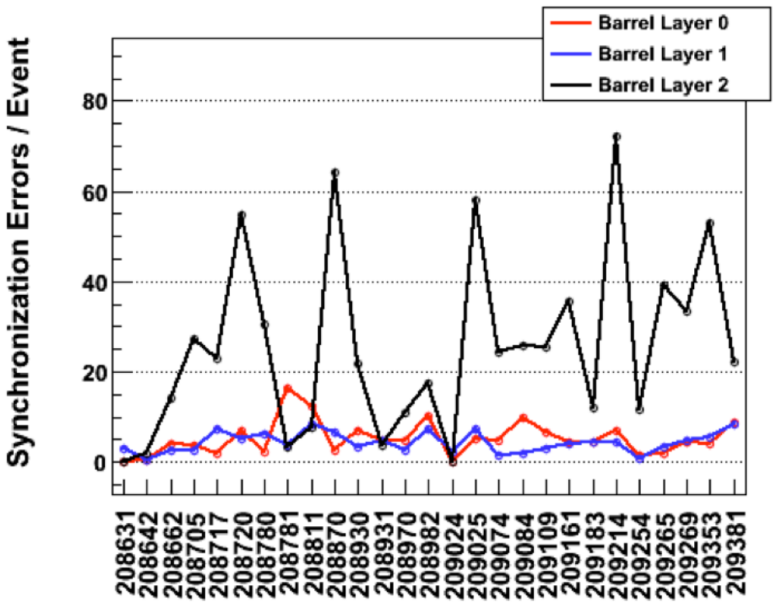

Figure 2.5: Number of desynchronized modules observed during 2012 (Run-I) in pp collisions with a center-of-mass energy of $\sqrt{s} = 8$ TeV measured by the ATLAS Pixel Detector. While B-Layer (layer 0, red) and Layer-1 (blue) shows stable performances during the year, Layer-2 exhibit an high number of de-synchronizations due to readout limitations.

2.3 Challenges for Run-II

The ATLAS Pixel Detector is expected to remain operational until the third long shutdown of the LHC machine, foreseen for the end of 2023. During this long period some modules are expected to fail, and due to the current configuration of the pixel detector any intervention or substitution of component is impossible. In particular, a loss of data taking capabilities in the Pixel B-Layer would seriously deteriorate the impact parameter resolution, directly affecting the b-tagging capability [2].
Taking into account the expected lifetime of the B-Layer an upgrade of the whole layer was deemed necessary together with the LHC phase-I upgrade. The original program of the B-Layer replacement planned its extraction and substitution with a new one, but the project appeared unfeasible. By exploiting improved technology, a new *Insertable B-Layer* (*IBL*) was designed and inserted between the existing one and the beam pipe.

In order to make room for the insertion of this layer, the existing beam pipe was replaced by a new Beriullium pipe with reduced diameter. This new *Be* beam pipe also decreased the material budget close to the interaction point. The addition of the fourth layer close to the beam-pipe not only ensures that the b-tagging capabilities will not deteriorate over time, but also improved the performances of the latter, being located closer to the interaction point with respect to the Pixel B-Layer.

The IBL is in particular important for the pattern recognition and fake track reduction at high instantaneous luminosity. In addition, it provides redundancy in case of failures or radiation damage in the present pixel system. This first phase of the upgrade took place during the LS1 of the LHC in 2013-2014. The insertion of the IBL did not, however, overcame the limits of the existing pixel detector layers. The planned approach was to upgrade the old layers by increasing the readout bandwidth for the mainly affected layers, Layer-2 and Layer-1, from 40 Mb/s to 80 Mb/s for Layer-2 and from 80 Mb/s to 2×80 Mb/s for Layer-1 respectively.
At the core of this upgrade lies the read-out technology developed for the Insertable B-Layer, namely the *Back Of Crate* (*IBLBOC*) and *Read-Out Driver* (*IBLROD*) boards designed for IBL. The IBL boards can easily expand the bandwidth of the Pixel Layer-2 and Layer-1 by using a dedicated firmware to interface with the old detector.
The two boards are paired back-to-back by a *Versa Module Europa* (*VME*) bus standard, which is the same configuration used by the previous read-out system. The IBLRODs handle the data processing while the IBLBOCs take care of the optical input/output functionality and interface. Both the IBLROD and IBLBOC boards are based on field-programmable gate arrays (FPGA) integrated circuits to implement logic circuit and soft processors on which a data acquisition and processing software can be ran.

[2] which is of primary importance for the search presented in this thesis, due to the high reliance on the reconstruction of b-jets

In addition, the B-Layer and Disks will be also upgraded using the IBL read-out system; this upgrade will be commissioned by the technical stop in 2018. Thus, eventually, the entire Pixel Detector of ATLAS will share the same hardware readout chain and software code, implementing different configurations with specific firmware depending on the front-end sensors and modularity.

2.4 The IBL upgrade

The new IBL was slid inside the pixel detector in 2014 (Fig. 2.6). It is located at a nominal distance[3] of 33.5 mm from the beam axis and is the closest layer to the interaction point of the ATLAS detector. Given the small sensor distance from the beam-axis (compared to 50.5 mm for the Pixel B-Layer), the sensors and front-end electronics must cope with a much higher hit rate and radiation with respect to the other layers. To address these requirements, a new front-end read-out chip has been developed, the *FE-I4*. The main differences

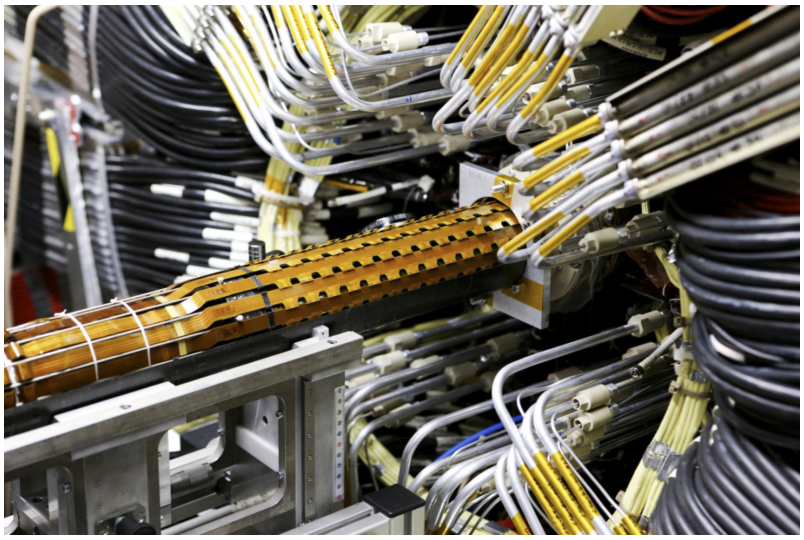

Figure 2.6: A moment of the insertion of the IBL in the pixel detector, in may 2014.

between with the FE-I3 chip, used by the Run-I pixel detector, are presented in Tab. 2.5.

	FE-I3	FE-I4
Pixel Size [μm^2]	50×400	50×250
Pixel Matrix	18×160	80×336
Active Fraction	74%	89%
Output Data Rate [Mb/s]	40	160

Table 2.5: Layout parameters of the FE-I3 chips, used for the Run-I pixel detector in B-Layer, Layer-1 and Layer-2, and the FE-I4 chip, designed for the new Insertable B-Layer.

The basic structure of the IBL is borrowed by the Run-I pixel layers, with

[3]the distance refers to the sensors position

	Pixel	IBL
Active Surface [m^2]	1.73	0.15
Number of channels [$\times 10^6$]	80.36	12.04
Pixel size [μm^2]	50×400	50×250
Pixel array [pixels]	18×160	80×336
Chip size [mm^2]	7.6×10.8	20.2×19.0
Active fraction [%]	74	89
Analog current [μA/pixel]	26	10
Digital current [μA/pixel]	2.0	1.2
Analog voltage [V]	1.6	1.4
Digital voltage [V]	2.0	1.2
Data out transmission [Mbit/s]	40	140
Sensor type	Planar	Planar/3D
Sensor thickness [μm]	250	200/230
Layer thickness [$\%X_0$]	2.8	1.9
Cooling fluid	C_3F_8	CO_2

Table 2.6: Main construction parameters of the Pixel detector layers and the new IBL detector.

multiple staves arranged in parallel with respect to the beam pipe. Planar sensors populate the central region of each stave, while 3D sensors the regions on the two sides. The staves are tilted by 14° with respect to the radial direction in order to achieve an overlap of the active area between staves. In case of 3D sensors, this also helps in compensating for the Lorentz angle of drifting charges.
Due to space constraints, the sensors are not overlapped along the stave (in z). However, to minimize the dead region the modules are glued on the stave with a gap of 200 μm. A comparison between the IBL and the 3 layer Pixel detector technical parameters is reported in Tab. 2.4. The reduction of the material budget leads to an optimization of the tracking performance; the average IBL radiation length is 1.88 X_0 for normal incidence tracks at $z = 0$ and it corresponds to $\sim 70\%$ of that for the Pixel B-Layer. A lower radiation length with respect to the Pixel has been achieved thanks to various improvements, such as the use of CO_2 evaporative cooling that optimizes the mass flow and the pipe size and the use of aluminium conductors for the electrical power services.

2.5 The Layer-1/2 upgrade

The increase of the pile-up in Run-II proved to be a critical factor for the Pixel Detector, as it induces a rise in data throughput that must be compensated with a faster and larger readout bandwidth. The Pixel upgrade project is based on the implementation of the read-out IBL Boards in place of the old *Silicon Boards* (*Si-ROD* and *Si-BOC*). The substitution followed [8] three primary points:

– *Backward Compatibility:* the implementation of the new boards in the

ATLAS Pixel Detector had to profit from the data path firmware logic of the previous generation of readout Si-Boards. For backward compatibility motivations, the VME bus was maintained in the IBL readout design even though it is by now an obsolete solution;

- *Online Histogramming:* a complete new scheme of steering and calibration firmware was employed; this led to the histogram fitting during calibration to be moved off-board. In the old Si-ROD cards this task was carried out on-board through digital signal processors while now the IBLRODs send data directly to a PC farm tasked with the histogram fitting;
- *Pixel Firmware and Software unification:* in order to save time and increase portability of improvements and fixed between the layers, the entire ATLAS Pixel Detector readout system must be based on a unified firmware and software code, integrating both IBL and Pixel layers;

The system bandwidth and readout speed of each module were increased to cope with the link occupancy to avoid de-synchronizations. Thanks to these changes, the IBLBOC and IBLROD proved to be an optimal replacement of the old readout for the outermost pixel layers. Tab. 2.7 shows the effects, in terms of link occupancy, of the readout upgrade.
The replacement of the Silicon BOCs and RODs towards IBLBOC and RODs started in 2015-2016 and was completed in 2017. In 2018 the B-Layer and Disks Si-BOCs and Si-RODs will be also replaced. While for the Disks there will be a doubling of the readout speed, for the B-Layer the readout speed will not increase as it is already at the limit for the module.

μ	B-layer	Layer-1		Layer-2	
	both readouts	old readout	new readout	old readout	new readout
	160 Mbps	80 Mbps	160 Mbps	40 Mbps	80 Mbps
40	60%	81%	41%	119%	59%
60	81%	103%	52%	159%	79%
80	101%	125%	63%	188%	98%

Table 2.7: Module Link occupancy estimation based on 2016 Run at different pileups (μ) assuming Level 1 trigger rate of 100 kHz and a center of mass energy of $\sqrt{s} = 13$ TeV. For each pixel layer, the expected link occupancy of the old Si-boards is confronted with that of the new IBL boards. Red numbers shows configurations in which the data throughput exceeds the available read-out bandwidth, causing de-synchronizations.

2.6 The new IBL Pixel boards

The IBL read-out system is summarized in Fig. 2.7. Data is sent from the modules to the read-out chain via optical fibres. Each read-out board pair (IBLBOC + IBLROD) is assigned to a certain number of modules, whose configuration depends on which Pixel Layer is connected to:

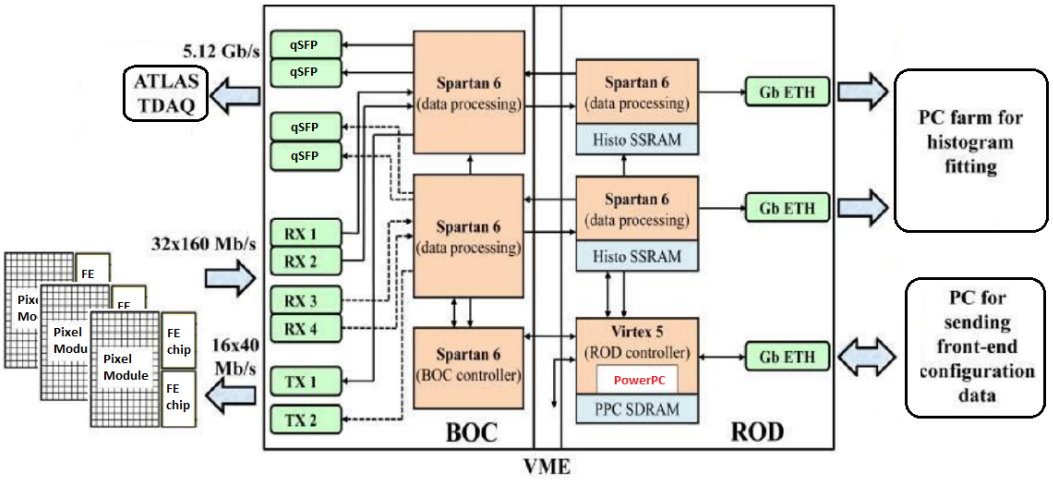

Figure 2.7: Logical scheme of the unified data-taking system for the pixel detector of ATLAS in Run-II. From left to right, Front-End modules read data from their respective pixel sensor, sending them to the read-out system via high-speed optical links. Optical signals are transduced by the Opto-electrical plugins mounted on the IBLBOC board and processed by dedicated Spartan6 FPGAs on the IBLBOC. Data is then sent, via VME bus, to the IBLROD, where is formatted and used for histogram fitting and monitoring. The formatted data is sent back to the IBLBOC via VME bus and forwarder to the ATLAS TDAQ system, where is stored, via optical transmission.

- *IBL:* Each card pair processes data received from 32 FE-I4 data links working at 160 Mb/s, for a total I/O bandwidth of 5.12 Gb/s [5]. The maximum data rate the MCC can deliver is two links at 80 Mb/s. The receiving part at the off-detector side is the IBLBOC card, which has 32 inputs from the modules and 32 outputs to the IBLROD. The maximum bandwidth between IBLBOC and IBLROD is slowed down to 40 Mb/s due to the formatters on the IBLROD.

- *Layer-2:* the IBLBOC is connected to 2 staves with all modules operating at 40 Mb/s.
  This fills the bandwidth capability of the cards completely.

- *Layer-1:* operating at 80 Mb/s only half the number of staves can be connected to the IBLBOC card as each incoming stream has to be split into 2×40 Mb/s towards the IBLROD. So only 1 stave can be connected per off-detector card pair.

The data, passing through optical fibres, is received by opto-electrical converters, known as *RX plugins*. The RX plugin transduces the optical signal from the fibre to digital electrical signals, which is processed by the IBLBOC. Data is then sent, via VME bus, to the IBLROD, which takes care of the data formatting and histogramming and is connected via a Gigabit Ethernet connection to a PC farm, dedicated to online data histogram fitting. Formatted data is sent back to the IBLBOC, which communicates with the ATLAS data

acquisition system, using the *S-Link* protocol. In the specific case of Layer-1, the links were already running at maximum bandwidth for a single channel; in order to increase its bandwidth an additional fibre had to be installed for each module. This second fibre can be used as the 2nd channel for its readout, effectively doubling the bandwidth to 2× 80 Mb/s per module.

Power is distributed to the system by VME connectors and the VME bus interfaces the IBLROD with the external DAQ controller system, acting as a backup in case of failure of the main ethernet control link. A Gigabit Ethernet connection on the IBLROD is used to interface the DAQ controller system (main connection) while two more Ethernet ports deliver the calibration scan results.
A common clock is distributed by a timing board, the TTCrq mezzanine, that receives the ATLAS clock and trigger commands.

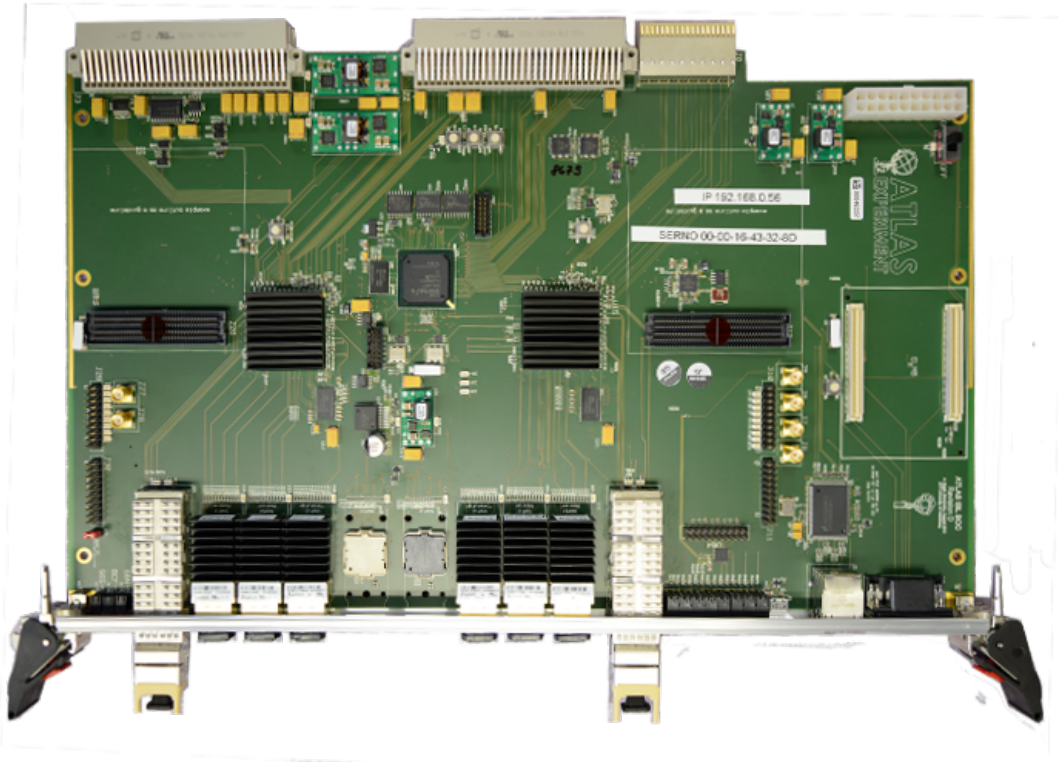

Figure 2.8: The IBLBOC (rev.D), used for the readout of the pixel detector during Run-II collisions at a center-of-mass energy of $\sqrt{s} = 13$ TeV.

The IBLBOC is responsible for the propagation of the detector timing and the signal conversion between detector, higher-level readout and IBLROD board. This new board, shown in Fig. 2.8, is based on the previous Pixel Si-BOC[6] but exploits FPGA technology for the signal processing. Three Xilinx Spartan-6 FPGAs are mounted on the board, enhancing flexibility and optimization for future tasks and upgrades.
The two IBL read-out boards are based on a common Master-Slave-Slave configuration: the BOC Control FPGA (*BCF*) provides the control logic for all modules on the card and the Ethernet interface. The two BOC Main FPGAs (*BMF*) are responsible for the signal processing on the card, including signal

conversion between the electrical interface to the IBLROD card and the optical interface to the detector and the higher level readout. The opto-electric conversion of the signals to and from the detector is performed by the RX plugins.
The connection to the higher-level readout is made with commercial (Q)SFP modules. Both (Q)SFP and SNAP12 modules are standardised and widely used in the telecommunication market. The connectivity with the data acquisition system is ensured by an ethernet port and two JTAG chains.

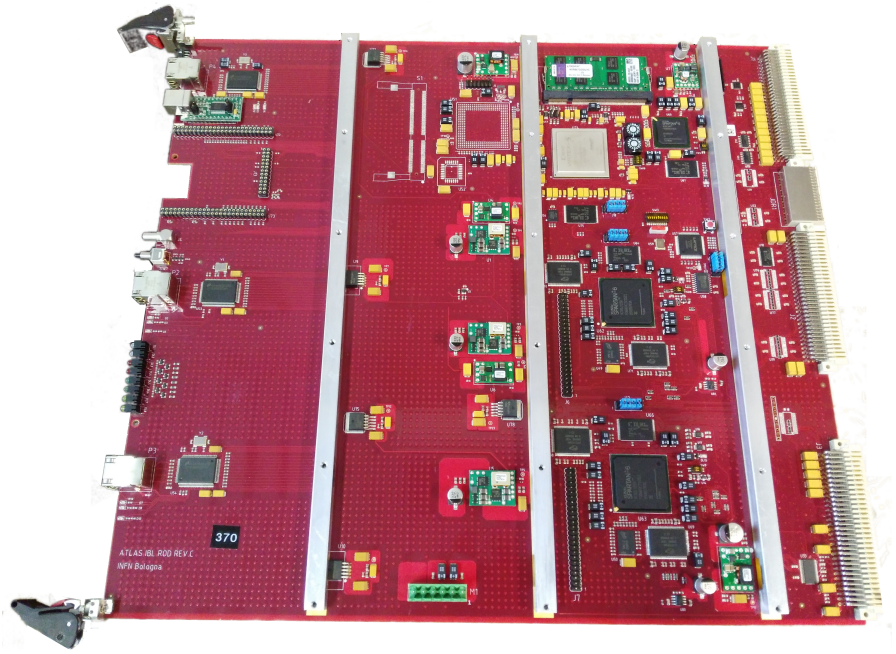

Figure 2.9: The IBL ROD (rev.C), used for the readout of the pixel detector during Run-II collisions at a center-of-mass energy of $\sqrt{s} = 13$ TeV.

The IBLROD card (Fig. 2.9) takes care of detector control (by configuring and sending commands to the read-out electronics), data taking (by forwarding triggers and building events), detector calibration (by steering dedicated acquisition runs, getting data and collect them for building cumulative histograms) and detector monitoring.
Various revisions of the board have been produced[7], in order to enhance signal stability and power consumption. The last revision (version D) features the fastest speed grade available on the market for the Xilinx Spartan-6 FPGAs. This choice was made to better cope with possible future upgrades of the current firmware which is already close to its performance limit in terms of speed and routing congestion.
As the IBLBOC, the IBLROD design implements a Master-Slave-Slave architecture (Fig. 2.10), where a Xilinx Virtex-5 master device controls the operation of two Xilinx Spartan-6 slaves dedicated to data processing (gathering of front-end output, event building, and calibration data processing).
To maintain backward compatibility, the PowerPC microprocessor embedded in the Virtex-5 performs the functions of the DSP of the old pixel Si-ROD.

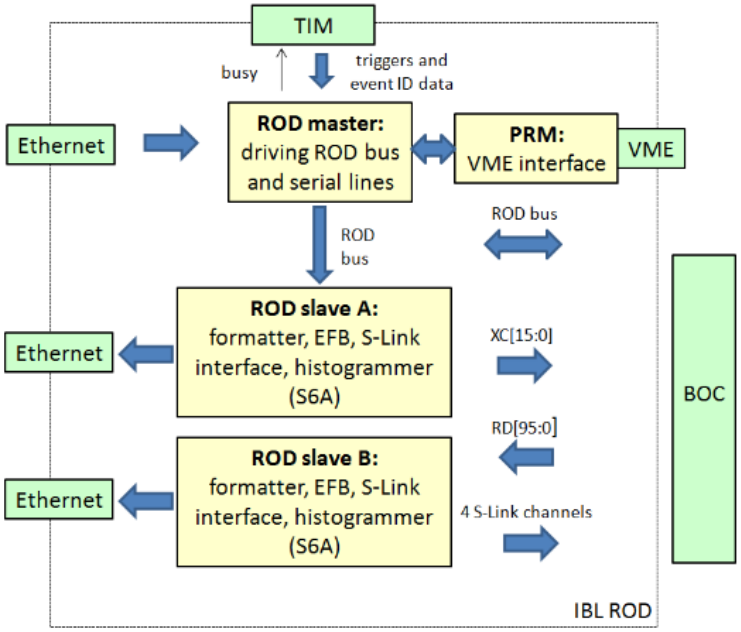

Figure 2.10: Connectivity map and block diagram of the main IBLROD logic components. The Master-Slave-Slave configuration is common between the entire IBL read-out system. The master device controls the operation of two slaves dedicated to data processing.

Static and dynamic memory components are hosted on the IBLROD; in particular, the Virtex-5 is equipped with a SO-DIMM DDR module. It is also supplied with a 64 Mbit Atmel Flash device devoted to the storage of both non-volatile parameters (e.g. Ethernet IP addresses) and software programs to be executed by the PowerPC.

The readout system must provide flawless operations over a wide time period. It is important to remember that interventions and replacements of the read-out boards are possible only during the shutdown periods. An issue with one or more boards could potentially compromise part of the pixel detector data taking capability. In order to prevent and diagnose board production, damages, software or firmware issues in advance, a number of electrical and functionality tests have been set in place. These tests have been performed a first time during the boards production by the laboratories in charge of the design and repeated at CERN during the insertion of the readout boards in the off-detector electronics.

The tests cover the totality of the functionalities required by the IBLROD and IBLBOC boards. Some calls on unique features or components of one of the two boards (SSRAM test, plugin BERT test), while others are focused on the correct intercommunication between the boards and the readout system. The tests that have been carried out are shown in Fig. 2.11.

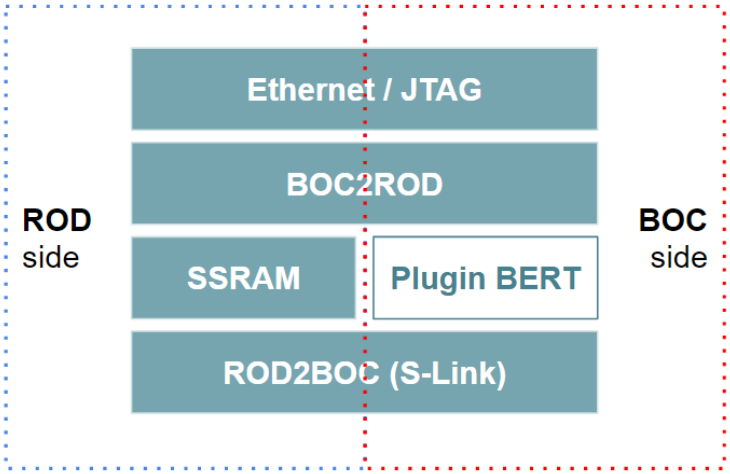

Figure 2.11: Block diagram of the testing procedures operated at CERN on the IBL data taking boards for the Layer-2 upgrade in 2015. The tests have been executed serially starting from the topmost, except for the SSRAM test and the Plugin BERT, which have been executed in parallel on the IBLROD and IBLBOC, respectively.

Ethernet and JTAG communication test

Any direct communication for debug or monitoring with the boards passes trough either Ethernet or JTAG ports.

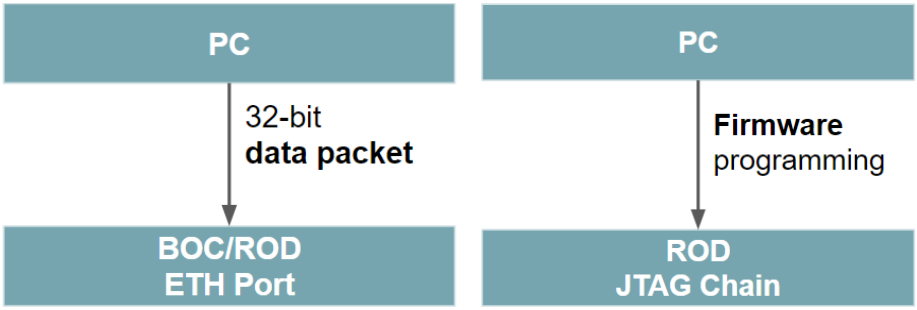

Figure 2.12: Test of the Ethernet connectivity (left) and JTAG connectivity (right) of the IBL ROD and BOC boards. For the Ethernet test, 12,000 32-bit data packets are sent to check the connection stability under stress. For the JTAG Chain test, both the master and the slaves firmware is loaded trough the JTAG port.

- To guarantee the stability of the connection with the system, all of the ethernet ports were tested (IBLROD master, 2×IBLROD slaves, IBLBOC). 12,000 32-bit data packets are sent (Fig. 2.12a) to each boards over the course of a two hours period in order to check the stability of the network; any drop in connectivity (package loss) could potentially indicate an issue with the ethernet port.

- The IBLROD JTAG chain was tested by loading both the Master and the Slaves firmware through the JTAG port (Fig. 2.12b). Boards with faulty

JTAG chain cannot be correctly controlled and lack low level debugging capabilities.

SSRAM test

One of the tasks of the IBLROD card is to generate histograms of the data for calibrating the detector. Preliminary estimates show how scans, which required about 10 minutes with the existing electronics, can be performed faster in the IBLROD. Since the histograms are read-out via Gigabit Ethernet links,

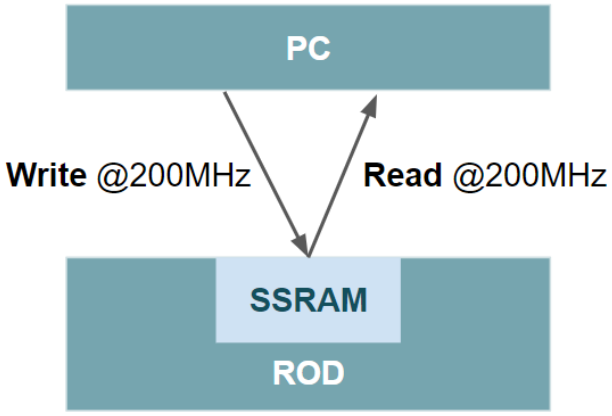

Figure 2.13: Block diagram of the Synchronous Static RAM (SSRAM) testing procedure operated at CERN on the IBL data taking board for the Layer-2 upgrade in 2015. The SSRAM is accessed for read/write operations a clock frequency of about 200 MHz.

acquisition runs with a comparable amount of data can be accomplished in about 10 seconds. The most important speed limitation becomes the maximum data rate of the Synchronous Static RAM (SSRAM) components. Due to the card design, in order to manage histograms for all Front-End modules in parallel, the selected SSRAM3 must be accessed with a clock frequency of about 200 MHz.
In order to test that the access to the SSRAM, in both reading the memory and writing on it, a 200 MHz read/write scan has been implemented. The test continuously write data on the SSRAM and read back the location in which it has written. This is repeated for a total of $\sim 1.5 \times 10^{12}$ times, giving a response on the Bit Error Rate reliability of the SSRAM. Fig. 2.13 illustrates a schematic representation of the testing procedure.

BOC2ROD

The data received by the IBLBOC from the Front-End modules, after decoding, is sent to the IBLROD via a 96-bit wide bus with a single line signal rate of 80 Mb/s. The bus width and the signal rate have been dimensioned as a trade-off between the bandwidth requirement between IBLBOC and IBLROD (5.12 Gb/s) and the design modularity (12 bit is the width of the front-end data). The bus connects the Spartan-6 FPGAs hosted on the different cards through the VME backplane connectors.

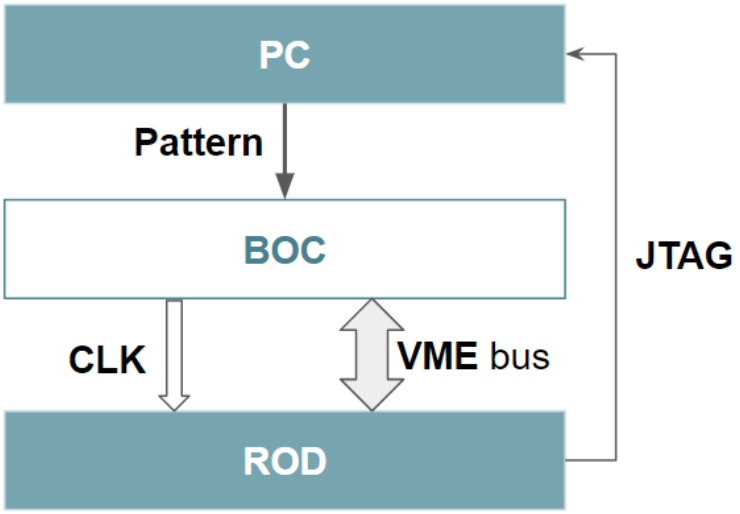

Figure 2.14: Block diagram of the communication between IBL BOC and ROD via the standard VME bus testing procedure operated at CERN on the IBL data taking board for the Layer-2 upgrade in 2015. A data pattern is sent to the IBLBOC and read back from the JTAG connection on the IBLROD. Read data is compared with the sent pattern to check for possible mismatches.

Transmission is double data rate, synchronized with a 40 MHz clock common to both cards. The bus has been designed to have minimal skew and to optimize the signal integrity in the PCB layout. Extensive tests have been performed with an ad-hoc firmware, sending a data pattern continuously and measuring the bit error rate by varying the phase of the receiver clock. The goal of this test was to measure the width of the good sampling phase window.

ROD2BOC

After the data has been processed and formatted by the IBLROD, it is sent to the external ATLAS DAQ system via the four S-Link data path. Each IBLROD Slave controls two S-Link channels, acting as the main connection between the IBLROD Slave and the respective BOC BMF. In order to test the ability of the IBLROD to address and send data to the S-Link, a known pattern is written by the IBLROD on the VME bus towards the IBLBOC S-Links. The pattern is read back from an external PC and eventual discordances with the original signal are investigated. The process is schematized in Fig. 2.15.

2.7 Opto-electrical converters RX

The transduction of the optical signals used for communication between the IBLBOC and the Front-End chips is executed by 4 × opto-electrical (RX-) and 2 × electro-optical (TX-) plugins, present on the IBLBOC. RX-plugins handle the transmission of data from the Pixel detector modules to the IBLBOC, while TX-plugins are responsible for the transmission of timing and control signals to the detector.
While commercial TX-plugins proved to be a feasible option for the IBL and

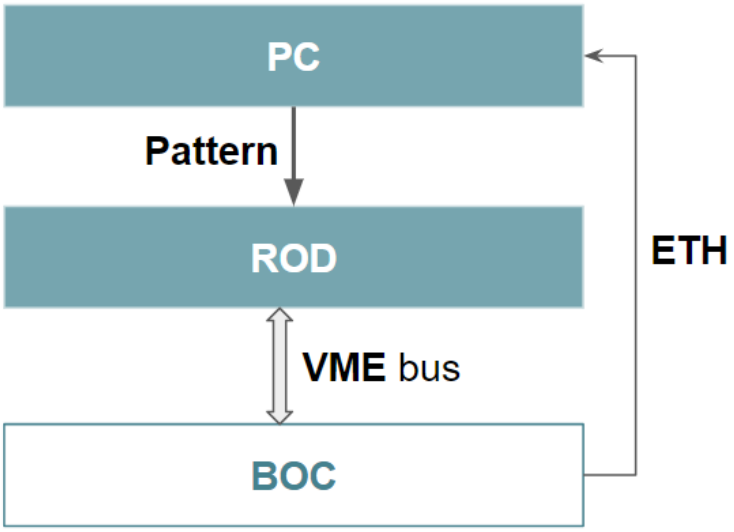

Figure 2.15: Block diagram of the communication between IBL ROD and BOC via the standard VME bus testing procedure operated at CERN on the IBL data taking board for the Layer-2 upgrade in 2015. A data pattern is sent to the IBLROD and read back from the S-Link channels on the IBLBOC. Read data is compared with the sent pattern to check for possible mismatches.

Pixel upgrade, custom RX-plugins had to be developed from scratches. RX-plugin were designed by the *University of Bern* and the *Ohio State University*, for the electronic and optical part, respectively.

The RX-Plugins are connected to the IBLBOC fitting the SNAP12 (MSA) standard 10 $\times$ 10 pin socket. The 160 Mb/s Pixel data stream is 8b/10b encoded to achieve a DC-balanced signal. Various prototypes have been developed exploiting different paradigms, such as solutions with discrete components or based on a custom ASIC. In the end, the ASIC solution outperformed other candidates in terms of stability of the operating range. 12 channels optical fibres connect the front-end electronics to the RX-plugin, where each channel is read by a PiN photodiode. The custom ASIC mounted on the RX-plugin, called *DRX-12 II*, detects the output of the PiN photodiode array. Each of the 12 channels is equipped with a transimpedance amplifier. The optical input current enters a transimpedance amplifier (TIA) and its value is compared by a comparator to a programmable threshold value. The output of the comparison is sent in the output line in LVDS format by a LVDS driver. The threshold of each channel is independent with respect to the others and can be set separately. The data format is non-return-to-zero (NZR) at 80 Mbit/s, with a signal current amplitude in the range of [40 μA $\div$ 2 mA]. It has been designed using AMS 0.35 μm CMOS technology and fully simulated via software, for behavioural and parasitic studies.

A custom PCB, shown in Fig. 2.17, was developed in Bern and extensive testing has been performed to ensure correct functionality over the course of Run-II and Run-III. Finally, the 12-channel optical array was developed and mounted by the Ohio State University. Extended testing of the single com-

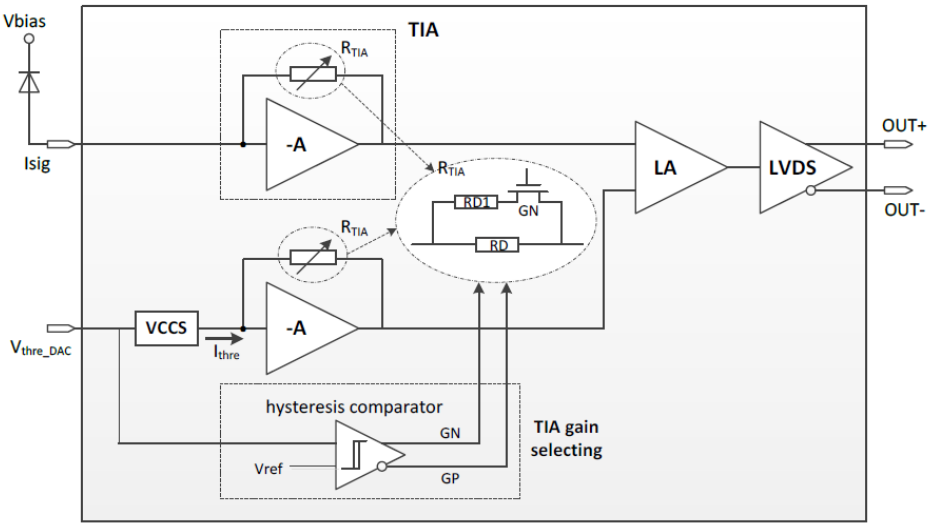

Figure 2.16: Block diagram of one of the 12 channels of the DRX-12 II ASIC. The input current to be transduced enters a trans-impedance amplifier (TIA) and its value is compared by a comparator to a programmable threshold value. The output of the comparison is sent in the output line in LVDS format.

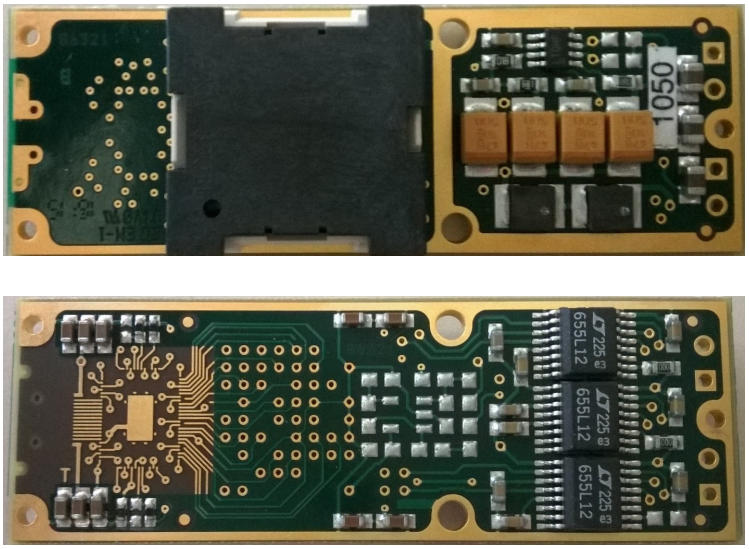

Figure 2.17: Front (top) and back (bottom) of the PCB which is base for the IBLBOC RX-plugin. The 10×10 SNAP12 connector is covered by a black cap. The gold-plated area on the left-bottom will host the DRX-12 II ASIC.

ponents, as well as the final product, have been put in place to ensure the reliability of the design. The goals were to check the correct independent operation of all channels in parallel, while minimizing the number of errors in the transmission over long periods and to make sure that the operating range was compatible with the final working conditions.

PCB electric connectivity tests

The designed electric connectivity of a PCB can be compromised by issues during the etching of the tracks, the soldering of the components on the PCB or simply due to errors in the design. It is therefore of primary importance to check the electric connectivity of all the PCB channels before continuing the production process, as the PCB itself is inexpensive compared to other components in the RX-plugins, such as the ASIC. Due to the huge amount of PCBs produced, the test of the connectivity had to be as quick and reliable as possible, while maintaining an high statistical value.
A testing board (Fig. 2.18) was designed by the University of Bern; it features a SNAP 12 connection on one side to accommodate the PCB to be tested and a matrix of test needles which directly connects to sense points on the PCB. Data is injected trough the SNAP 12 connector and checked via the sense needles directly on the board.
The whole system is managed with an Arduino DUE controller by the RXino

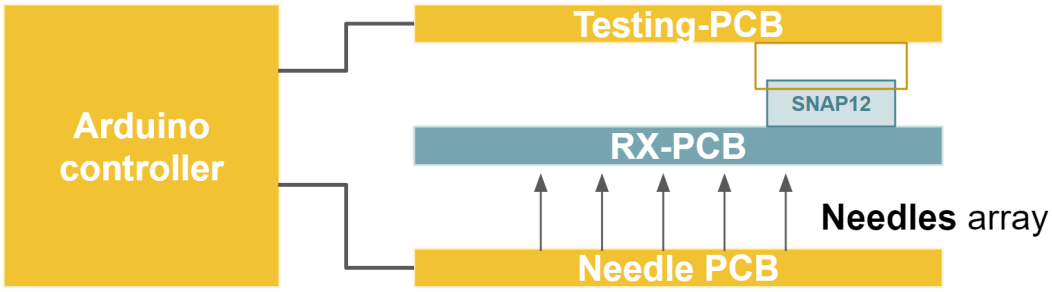

Figure 2.18: PCB electrical connection testing board, designed to check the connections. Electric signals are injected into the RX-PCB by a testing PCB, plugged on the SNAP12 connector of the RX-PCB. The signals are then checked on sense points on the RX-PCB by an array of sense needles, connected to a custom Needle PCB, and compared by an Arduino microcontroller.

suite (that I personally developed), which generates data to be injected, sets the threshold voltage value V_{th} of each of the 12 channels and read back the data signal as it passes though the board, via the testing needles.

- *Connection Test:* A first test checks that no broken tracks or high impedances are present on the PCB. A 3V DC signal is is injected in the SNAP12 connector by the Arduino DUE board and read back from sense points using the testing needles;

- *Insulation Test:* Imperfect soldering or track etching can potentially lead to serious cross-talk or direct connections between nearby channels, compromising the functionality of the PCB. Using the same setup as the Connection Test, a 3V DC signal is injected in a specific channel via the SNAP12 connector by the Arduino DUE controller; in all the channels travelling close to the selected channel the reading from the sense point must not be higher than 30 mV (which are always present due to electric noise);

– *Threshold Test:* The discrimination of optical signals operated by the DRX-12 II ASIC is based on the comparison between the input signal, coming from an optical fibre, and a reference threshold value. This threshold can be changed via an I^2C bus present on the PCB, which stores the selected value on a 32-bit shift register for each of the 12 channels .

  The threshold of all the channels if set at 1.25 ± 0.02 V by default. By driving the I^2C bus present on the Arduino DUE, the value was changed to 250 mV. Using the test needles, the stored value was read back as an analog signal and checked if within an interval of ±10 mV.

The GoNoGo board: Electro-optical tests

Issues may occur during the wire-bonding of the ASIC/optopackage on the PCB. If an issue is found before encapsulation, it can be solved and the RX recovered. A full test of the functionalities of the RX-plugin would require a IBLBOC board and a full-crate setup, which is impractical for extensive testing of large numbers of RX-plugins. To address this need, I developed a testing

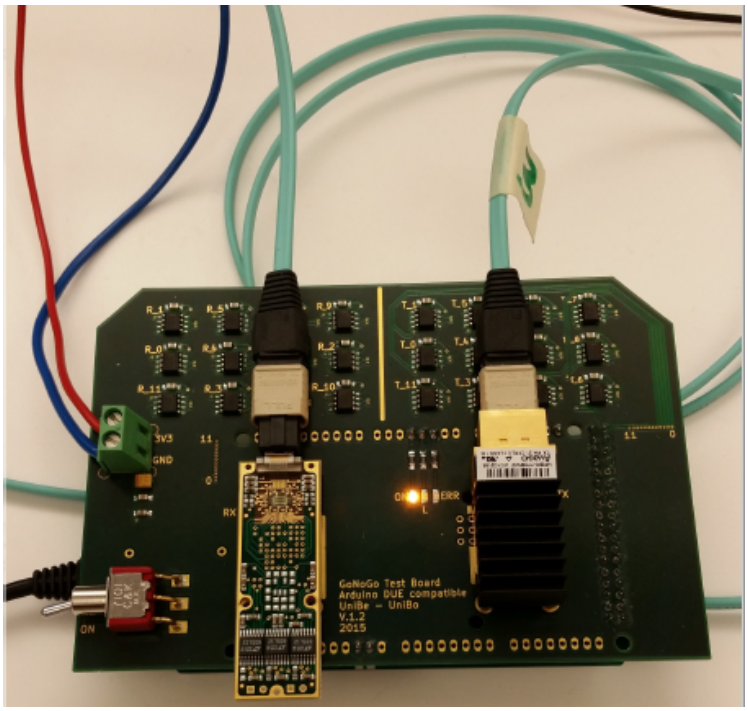

Figure 2.19: The GoNoGo board v1.2, produced in Bern for Loopback tests of the completed IBLBOC RX-plugins. The data is sent from an Arduino controller (located under the board) to a TX-plugin (right slot) which tranduces the electric signal to optical pulse, driving it in a 12-channels optic fibre. Data is read back by a custom RX-plugin (left slot) and converted back to an electrical digital LVDS signal.

board, the GoNoGo board, able to perform a quick loopback test using a TX/RX-plugin pair. After a first prototype, a revision called the GoNoGo 1.2 (Fig. 2.19) was validated independently in Bern and OSU.

As the Arduino architecture proved to be reliable for the testing procedures, the GoNoGo board has been built as an Arduino DUE compatible Shield. Two SNAP12 connectors are present on the board to accomodate the TX and RX plugins. The system is powered using two distinct lines:

- the Arduino DUE board is powered at 3.3 V using a USB cable for both powering and software loading;
- the GonoGo board is powered by a power supply at 3.3 V that also provides a common ground for the entire system;

The GoNoGo board performs a fully automatized test of the correct data transmission in the loopback using six different patterns (Tab. 2.8), to avoid fake correct signals due to shorts or crosstalk between channels. Each of the 12 channels is subject to $\sim$ 100 pattern changes and reading each second.

	Pattern 1		Pattern 2		Pattern 3	
	Normal	Inverted	Normal	Inverted	Normal	Inverted
CH 0	0	1	1	0	1	0
CH 1	0	1	1	0	0	1
CH 2	0	1	1	0	1	0
CH 3	0	1	1	0	0	1
CH 4	0	1	1	0	1	0
CH 5	0	1	1	0	0	1
CH 6	0	1	1	0	1	0
CH 7	0	1	1	0	0	1
CH 8	0	1	1	0	1	0
CH 9	0	1	1	0	0	1
CH 10	0	1	1	0	1	0
CH 11	0	1	1	0	0	1

Table 2.8: GoNoGO board data patterns. Each pattern targets a different possible issue of connectivity or cross-talk and the GoNoGo board loops continuously though them.

The patterns are focused on the continuous change the status of each channel. Channel 0 is not used in the final setup, so its status is automatically skipped.

RX-plugin Bit Error Rate Test

Once tested and encased, the RX-plugin is ready for a final quality check. The RX is plugged into a IBLBOC and a MCC-like Non-Return to Zero communication is performed, using an external nSQP board, the Optoboard, as a source of the optical signal. Signal Bit Error Rate is tested with a for 10^{12} bit transmission @80 MHz, varying the threshold voltage for the comparator $V_{threshold}$ and the optical input power current I_{input}. A schematic representation of this test in shown in Fig. 2.20. A typical test result, in the $V_{thres} - I_{input}$ plane, is presented in Fig. 2.21. Different colors indicates different fractions of bit-error

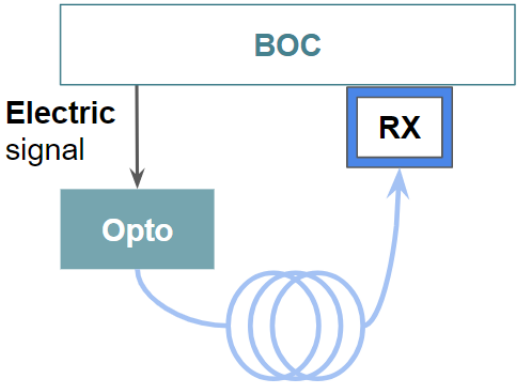

Figure 2.20: Block diagram of the RX-plugin Bit Error Rate test. Data is sent from an IBLBOC to an nSQP Optoboard, converting the electrical pulse to an optical signal. The optical data is transmitted trough an optical fibre and read-back by the RX at a rate of 80MHz.

rate in the readback data.
At least a subset of the $V_{thres} - I_{input}$ region is expected to be stable and not show any transmission error after 10^{12} bit transmissions, shown in the figure as a black region. The white region is out of specifications for this transmission and has not been tested.

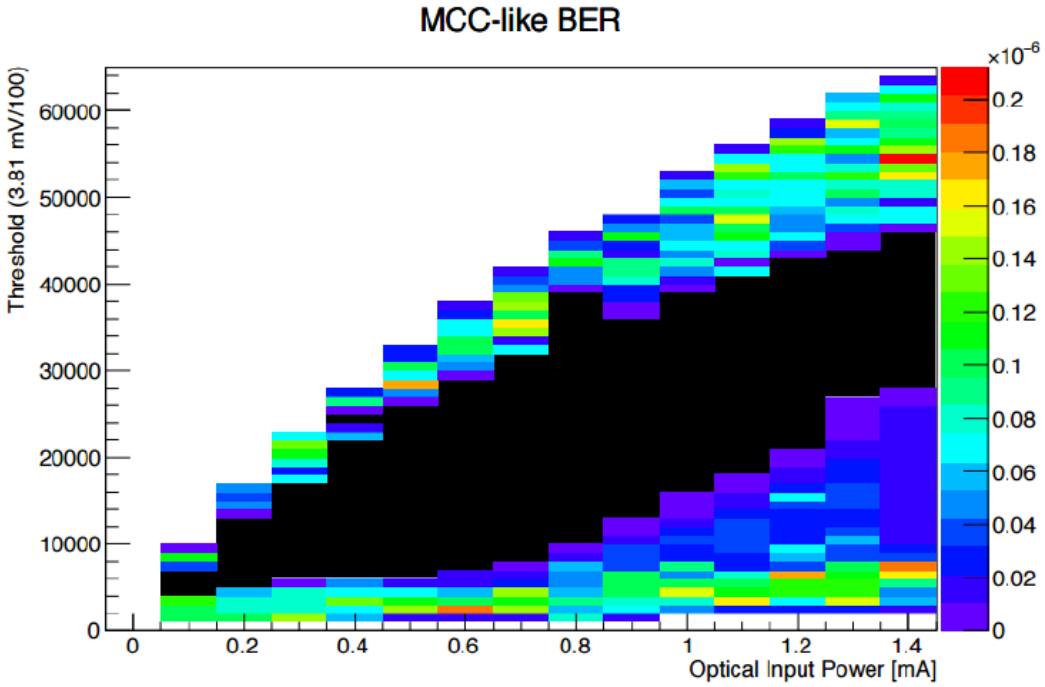

Figure 2.21: Typical test result of an RX-plugin Bit Error Rate Test. Different colors indicates different fractions of bit-error rate in the readback data. At least a subset of the $V_{thres} - I_{input}$ region is expected to be stable and not show any transmission error after 10^{12} bit transmissions, here shown in black. The white region is out of specifications for this transmission and has not been tested.

2.8 Pixel detector upgrade impact

The need for an upgrade of the ATLAS pixel detector in view of Run-II was first of all motivated by the high link occupancy observed during Run-I and by the foreseen module desynchronization errors caused by it (as introduced at the beginning of this chapter). The evaluation of the efforts in the pixel detector upgrade can be therefore left to the observation of the behaviour of the data-acquisition system in the years following the IBL insertion (2014) and the Layer-2 upgrade (2015).
In Fig.2.22 is shown the average fraction of modules with desynchronization errors for june to august runs during 2015. IBL (in black) shows an higher average fraction of modules with desynchronization errors with respect to the other pixel detector layers, B-Layer (red), Layer-1 (green) and Layer-2 (blue). During this first phase, the IBL data acquisition system was still in its early stages and lacked optimization.
A complete overhaul of the IBL ROD firmware was performed during the first weeks of august 2015, leading to a considerable decrease by more than two orders of magnitude in the average fraction of desynchronization errors during data-taking. Data-taking wise, the IBL passed from being the worst to the best performing pixel detector during this upgrade period.

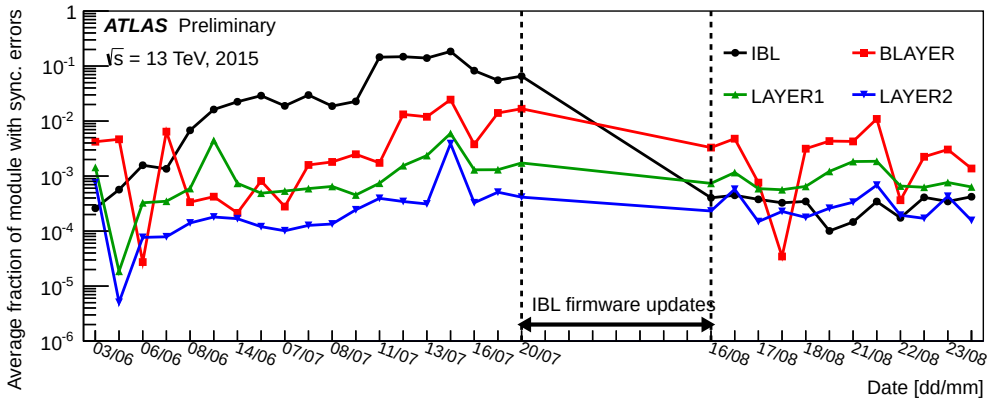

Figure 2.22: The average fraction of modules with synchronization errors for each 2015 run for IBL (black), B-Layer (red), Layer-1 (green) and Layer-2 (blue) in Run-II. Each point shows the average fraction in a given run. The synchronization error signals a discrepancy between the level-1 trigger or bunch crossing identifiers recorded in the front-end chips and those stored in the central acquisition system. The fraction of synchronization error of IBL decreases by more than two orders of magnitude due to improvement of the ROD firmware.

A similar consideration can be done for the Layer-2 upgrade that took place during 2015; Fig.2.23 shows the average fraction of pixel detector modules with desynchronization errors per event in 2016 runs. The effect of the subsequent increase in the number of interactions per bunch crossing and colliding bunches in the machine (up to approximately 32 and 2100 respectively) is visible until the end of June, when the change in the Layer-2 ROD firmware was adopted, leading to a factor 10 decrease in the synchronization error rate (blue line).

At the same time the ATLAS trigger rate was raised from 70 kHz to 85 kHz, making the firmware modification even more relevant.

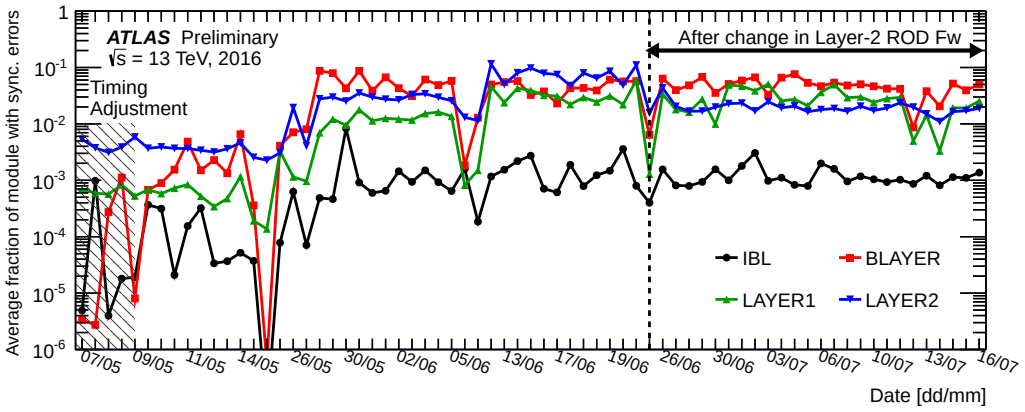

Figure 2.23: The average fraction of pixel and IBL modules with synchronization errors per event in 2016 runs. Each point shows the average fraction in a given run. The synchronization error signals a discrepancy between the level-1 trigger or bunch crossing identifiers recorded in the front-end chips and those stored in the central acquisition system. Different readout windows were used for Pixel and IBL in the first 5 runs due to timing adjustments. Runs until the middle of May were characterized by a low number of interactions per bunch crossing (< 25) and colliding bunches (< 1200). The effect of the subsequent increase in the number of interactions per bunch crossing and colliding bunches in the machine (up to approximately 32 and 2100 respectively) is visible until the end of June, when a change in the Layer-2 off-detector firmware (ROD Fw) was adopted, leading to a factor 10 decrease in the synchronization error rate. Data used in this plot have been collected by a mixture of triggers used in the monitoring stream.

The impact of this upgrade is not limited to the pixel detector performance alone, but extends to the ATLAS physics observables in both indirect and direct ways: first, by giving the possibility to operate the pixel detector flawlessly during Run-II and therefore taking advantage of the increased luminosity and center-of-mass energy to increase the ATLAS sensitivity to rare decays and probe wider phase space regions; second, the presence of a new high-technology pixel detector layer close to the interaction point leads to a significant improvement in the ability to discern tracks originating from b-quarks, as discussed in **Chapter 4**.

Part II

Searching for Supersymmetry

Chapter 3

Supersymmetrical models

Starting from the end of the 1940s and especially during the 1950 and 60s, the study of cosmic rays (1945-55) and accelerator physics (1960-65) lead to the discovery of a huge amount of new particles, never observed before (Fig. 3.1). It soon became clear that these particles could not be elementary and must have been generated as a combination of a smaller number of fundamental objects, combined by an yet-to-be-discovered force.

These elementary particles were successfully identified by Gell-Mann and

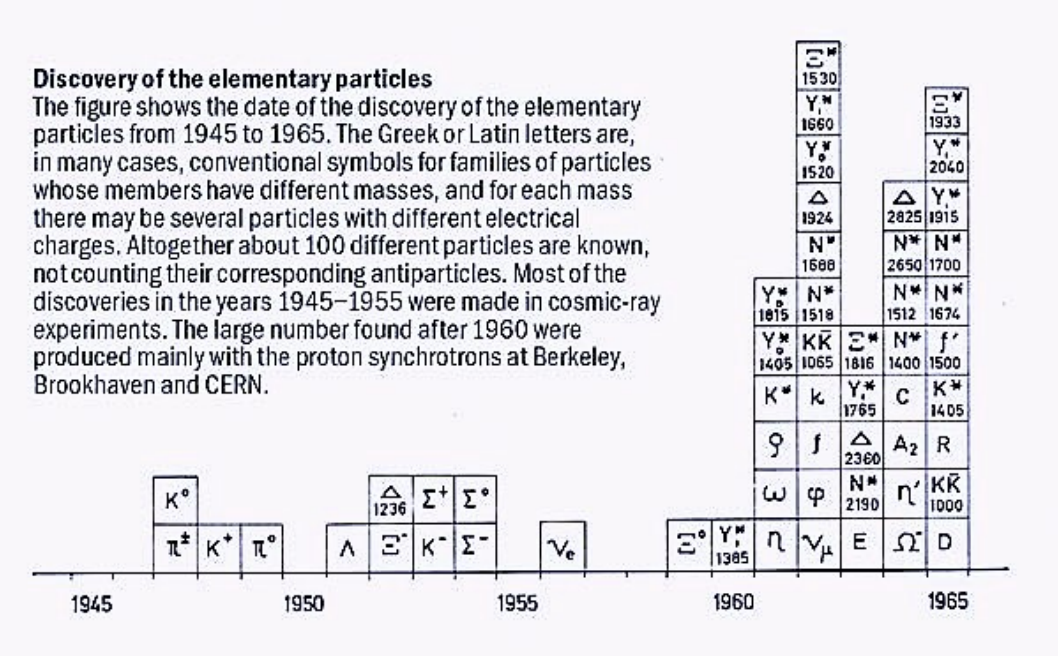

Figure 3.1: Time-line of particle discoveries, in the period 1945-1965. The greek and latin letters are conventional symbols for families of particles whose members have different masses and electrical charges. Altogether, about 100 different particles are known, not counting their corresponding antiparticles. [CERN courier, December 1966]

Zweig as *Quarks* (or *Aces*, as proposed by Zweig), organized into multiplets of $SU(3)_f$, the **f** referring to a new quantum number describing these objects, the *flavour*. This procedure was known as the *eight fold way* of Gell-Mann and Neeman. It soon became clear that, using a similar principle of unifica-

tion, a common model describing every known particle and interaction could be created. A first step in this direction was indeed already been made by S.Glashow in his 1961 paper, with the proposed unification of electromagnetic and weak interaction [15] and later expanded by S.Weinberg(1967)[16] and A.Salam (1968)[17] with the inclusion of the Higgs mechanism to the Glashow frame.
During the following half of the century the study of particle physics shifted more and more from the detection of cosmic rays to the particle accelerators which provide a much more controlled environment. Exploiting the collisions of accelerated particle beams with targets of different nature, tenth of new particles were discovered laying the foundations for a better and better understanding of the fundamental laws ruling the microscopic world. Since then, huge progresses have been made; a coherent theory, the so-called *Standard Model* (SM), encompassesing all known particle physics phenomena has been built piece by piece, starting from the pioneering work of Glashow and leading to predictions as accurate as one part in 10^{10} (for example, it is the order of magnitude of the precision of the anomalous electron magnetic moment [18]), whereas some of them (particularly the ones involving low energies and the strong interactions) have only been tested only at the 10% level.
On the other hand, there is to date no unambiguous direct particle collider measurement which contradicts the SM predictions. The study of what lies Beyond the Standard Model must therefore focus on more precise measurements at the colliders in order to observe the possible effects of new physics trough virtual effects leading to sizeable deviations from SM predictions.

3.1 The limits of the Standard Model and the hierarchy problem

Every phenomena related to particle physics observed from the first half of the 20^{th} century to date can be explained by using a small set of particle and interactions settled within the SM framework; however, this doesn't mean that the SM is expected to be the final theory supposed to be valid in every condition[19]. There is a certain number of assumptions that could be fundamental to the a theory such as of the SM (and every theory in general) that brings along limits to the validity of the theory itself. An historical example of this assertion can be done by studying the evolution of the theory behind the weak-interaction.
A first approach to this matter was made by E.Fermi in 1933 in his article on the study of β decay [20]. Using this method, it is possible to describe a $2 \to 2$ scattering between 4 fermions and an electron as a point-four-body interaction (Fermi β-interaction, Fig. 3.2):

The scattering amplitude of this $2 \to 2$ fermions process grows, at high energy, quadratically in respect to the center-of-mass energy of the two colliding fermions E_{cm}:

$$\alpha_W \sim G_F E_{cm}^2 \simeq \frac{E_{cm}^2}{v^2} < 16\pi^2 \tag{3.1}$$

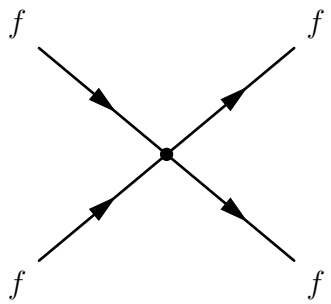

Figure 3.2: Feynmann diagram of a four-body point interaction between four fermions, such as two leptons and two neutrinos, using the Fermi β-interaction theory.

At high values of E_{cm}^2 this values becomes too large, overcoming the critical value of $16\pi^2$, meaning that the Weak force gets too strong to be treated as a small perturbation of the free-fields dynamics and the perturbative treatment of the theory breaks down. Being the Fermi theory instrinsically defined as a perturbation theory, as soon as this non-perturbative regime is reached (i.e. as the energy approaches an high value) the theory itself becomes inconsistent and, in general, not predictive of the behaviour of the system.
A new physics is therefore needed to explain this class of processes in an either perturbative or non-perturbative way and the effects of this physics must show up before the energy cut-off:

$$\Lambda = \frac{4\pi}{\sqrt{G_F}} \simeq 4\pi\nu \tag{3.2}$$

where $\nu \simeq 246$ GeV is the Electro-Weak Symmetry Breaking energy scale (EWSB).
This new physics, namely the mechanism of transport of momentum via an intermediate vector boson, has been in fact proven by the experimental discovery of the W vector boson, which mediates the scattering shown in Fig. 3.2. It must also be noted that the mass of this vector boson is $m_W \simeq 80$ GeV, far below the $4\pi\nu$ value required by the constraint on perturbativity required by the Fermi theory.
In general, interactions happening at an energy below an energy scale of the order of 10^4 GeV (the LHC energy scale) are well described by the SM: however, there is a certain number of events that do not enter in this model and must be therefore described in different ways:

- *Gravity:* The entire class of events described by the interaction with the gravity cannot be described by this method, as the Einstein-Hilbert action contains non-renormalizable interactions. This makes the graviton scattering amplitude grow quadratically with the energy predicting new physical processes of quantum gravity at high energy; in this case, the scale at which we can expect this cut-off can be as high as the Plank scale: $\Lambda_{Plank} \approx 10^{19}$ GeV. As can be easily understood, it's basically impossible to probe a region at so high energy, as the current limit of experimental searches is $\approx 10^4$ GeV.

- *Hierarchy problem:* If we consider higher energies up the to Grand Unified Theory (GUT) ($\Lambda_{GUT} \approx 10^{16}$ GeV) or Planck scale, we encounter a

number of conceptual problems: The first comes from the very large difference between the electroweak energy scale and the GUT or the Planck scales. This is called *hierarchy problem*. This affects the Higgs boson mass: without any additional symmetry stabilizing the electroweak scale by providing a cancellation mechanism, the Higgs mass receives large corrections by the one-loop diagram contributions.

– *Dark Matter and Dark Energy:* cosmological observations gave an insight on the existence of massive particles which have no candidates in the Standard Model.

– *Standard Model Generations:* quarks and leptons seem to have a lot in common, like the existence of three non-mass degenerate families, and this is not addressed in the Standard Model.

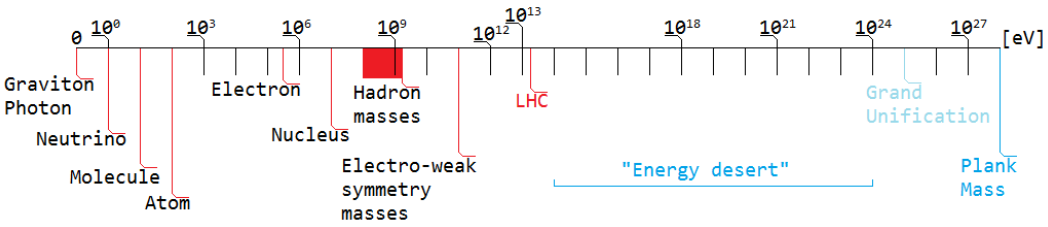

Figure 3.3: Energy scales of the known phenomena and particles. The highest energy we are currently able to directly probe is the LHC energy ($\sim$ 10 TeV, in red). New physics is expected to show up at around 10^{16} GeV (Grand Unification Theory). The limit of validity of the known physics is the Plank Mass scale at 10^{19} GeV.

The starting point of this search is the observed mass of the Higgs boson: after more than 40 years of research this last "missing piece" of the Standard Model puzzle has been experimentally observed at the LHC (CERN) by two distinct detectors, ATLAS [10] and CMS [11], with a mass $m_h = 125.09 \pm 0.24$ GeV. This mass value is a fundamental parameter of the SM, driving most of the processes and the physics described by it; at the same time, the mass itself is an input parameter of the SM and is not predicted by the theory itself, if not by a constrain on the maximum value the mass itself can assume due to considerations similar as the ones presented in the previous paragraph, limiting its value to $\sim$3 TeV.
This mass value could either be an intrinsic constant of nature or being generated from processes of new physics; in the latter case, we can postulate the existence of a fundamental theory of new physics, yet to be observed, giving rise to the microscopic origin of the Higgs mass-term, with a coefficient predicted by the fundamental theory in terms of its own more fundamental input parameters.
As previously observed, it is of primary importance to determine at which energy scale this theory will show up, replacing the SM; Fig. 3.3 shows that there are no indication of new physics or natural limits of the SM for energies lower than the Plank scale (10^{19} GeV). Being the Plank scale the only

constraint, it seems odd that $\frac{m_h}{M_{Plank}} \approx 10^{-17}$ is so much smaller than 1, as in a fundamental theory one might expect to have the effect of the theory (the mass of the Higgs boson) to be at the same order as the scale of the theory itself. The impossibility of answering this point in the frame of the SM poses the so called Hierarchy Problem, that is the lack of an explanation of what constraints the mass of the Higgs boson to the experimental value of $\sim$ 125 GeV.
In QFT, one sees that quantum corrections (loops) to m_H are expected to be, for a fermion f coupling with the Higgs Boson, described with a lagrangian term given by:

$$\mathcal{L} = -\lambda_f H f \bar{f} \tag{3.3}$$

giving rise to mass corrections to the bare mass of the Higgs boson m_{H0}:

$$m_H^2 = m_{H0}^2 - \frac{|\lambda_f^2|}{8\pi^2}\Lambda_{UV}^2 + ... \tag{3.4}$$

where m_H is the observed mass of the Higgs boson, λ_f is the Yukawa coupling of the fermion f and Λ_{UV}^2 is the ultraviolet momentum cut-off, used to regulate the loop integral. This cut-off should be interpreted as the energy scale at which new physics enters to alter the high-energy behaviour of the theory [12].

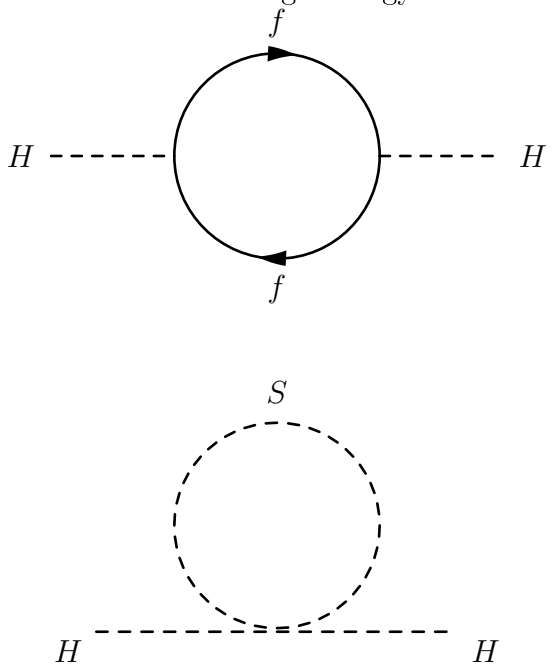

Figure 3.4: One-loop quantum corrections to the Higgs squared mass parameter m_H^2, due to (a) a Dirac fermion f and (b) a scalar S

As observed in Fig. 3.4, these contributions lead to a divergence of the Higgs mass, quadratically proportional to the factor Λ_{UV}, with a contribution of the m_f loops growing at most logarithmically with Λ_{UV}.
Due to the fact that the Higgs boson couples with almost every particle of the SM and that the masses themselves are obtained by this coupling, this divergence lead to a dependence of the cut-off scale Λ on the masses of every

lepton, quark and electro-weak boson of the SM, due to their dependence on the Higgs vacuum expectation value (VEV).

In the fundamental theory formula that predicts the Higgs-mass term it will be possible to identify two distinct contributions: one of them, $\delta_{SM} m_H^2$, resulting from the exchange of virtual quanta with virtuality below Δ_{SM} (the energy scale of the SM), while a second one, $\delta_{BSM} m_H^2$, coming from physics about such scale.
The total observed Higgs boson mass can be parametrised as:

$$m_H^2 = m_{0H} + \Delta m_H^2 = m_{0H}^2 + \delta_{SM} m_H^2 + \delta_{BSM} m_H^2 \tag{3.5}$$

where m_{0H}^2 is the "naked" mass of the Higgs boson, $\delta_{SM} m_H^2$ and $\delta_{BSM} m_H^2$ are the radiative contributions from the coupling respectively with the SM and BSM particles it interacts with. The standard models contribution can be estimated via the couplings of the SM particles with the Higgs bosons: the top quark, for example, is the SM particle with the highest coupling with the Higgs, with a Yukawa coupling $y_t \sim 1$, producing a fermionic contribution (3.4a) of the order of:

$$\delta_{SM} m_H^2 \simeq \frac{3\ y_t^2}{8\pi^2} \Delta_{SM}^2 \tag{3.6}$$

that, for $\Delta_{SM} >> \mathcal{O}(\text{TeV})$ [1], grows significantly above the observed value of m_H. The BSM term, in order to cancel this contribution, is forced to be of the same order (and almost equal) to the SM term, with an opposite sign, giving rise to the observed value of the mass of the Higgs boson. This process is defined as *fine-tuning* and the "order" of fine-tuning required for our theory to match experimental data is defined as:

$$\Delta \simeq \frac{\delta_{SM} m_H^2}{m_H^2} \simeq \left(\frac{\Delta_{SM}}{450\ \text{GeV}} \right)^2 \tag{3.7}$$

where $m_H \simeq 125$ GeV is the observed mass of the Higgs boson.
The level of *fine-tuning* Δ needed to account for the observed value of a parameter (in this case, the Higgs mass m_H) from new physics at the cut-off scale Δ_{SM} gives us an insight on the *Naturalness* of our solution; the theory can be therefore defined *Natural* if $\Delta \lesssim 1$ and *Un-Natural* if $\Delta \gg 1$[13].

3.2 Supersymmetry as solution to the hierarchy problem

As we have seen in the previous paragraph, this cancellation of two unrelated terms of the same order Δm_H^2 could be responsible of the stabilization of observed mass of the Higgs boson, independently on the order of fine-tuning Δ of the terms themselves. Presented these constraints, it is now time to discuss a solution (that is, formulating a theory of new physics) that satisfies these requirements and provides a term of opposite sign that cancels the known SM contribution. Considering that every particle that couples with the Higgs

[1] remember that the only constraint on Δ_{SM} is Δ_{Plank}

boson gives rise to a contribution on its mass term $(\delta_{SM} m_H^2)_i$, a natural way to cancel (almost) exactly this factor is to consider a second set of particles, mostly identical to the SM one, coupling with the Higgs boson.
This second set of particle has a fundamental difference in nature from the SM one, namely it associate a fermionic (bosonic) partner to each boson (fermion) of the SM, the generators of this new symmetry being Majorana spinors:

$$Q_\alpha \ (\alpha \ = \ 1, 2, 3, 4)$$

that act on the physical states changing their spin of a quantity $\pm\frac{1}{2}$. The fermionic generators satisfy the relations:

$$[Q_\alpha, M^{\mu\nu}] = i(\delta^{\mu\nu})^\beta_\alpha Q_\beta \tag{3.8}$$

$$\{Q_\alpha, \bar{Q}^\beta\} = -2(\gamma_\mu)_{\alpha\beta} P^\mu \tag{3.9}$$

$$[Q_\alpha, P^\mu] = \{Q_\alpha, Q_\beta\} = \{\bar{Q}_\alpha, \bar{Q}_\beta\} = 0 \tag{3.10}$$

with

$$\sigma_{\mu\nu} = \frac{1}{4}[\gamma_\mu, \gamma_\nu] \tag{3.11}$$

$$\bar{Q}_\alpha = Q_\alpha^T \gamma^0 \tag{3.12}$$

and γ_μ are 4×4 Dirac matrices

$$\gamma_0 = \begin{pmatrix} 1 & 0 & 0 & 0 \\ 0 & 1 & 0 & 0 \\ 0 & 0 & -1 & 0 \\ 0 & 0 & 0 & -1 \end{pmatrix} \qquad \gamma_2 = \begin{pmatrix} 0 & 0 & 0 & -i \\ 0 & 0 & i & 0 \\ 0 & i & 0 & 0 \\ -i & 0 & 0 & 0 \end{pmatrix}$$

$$\gamma_1 = \begin{pmatrix} 0 & 0 & 0 & 1 \\ 0 & 0 & 1 & 0 \\ 0 & -1 & 0 & 0 \\ -1 & 0 & 0 & 0 \end{pmatrix} \qquad \gamma_3 = \begin{pmatrix} 0 & 0 & 1 & 0 \\ 0 & 0 & 0 & -1 \\ -1 & 0 & 0 & 0 \\ 0 & 1 & 0 & 0 \end{pmatrix}$$

$P^{\mu\nu}$ is the momentum operator and $M^{\mu\nu}$ is the Lorentz group generator.
We can use this symmetry (admitting it exists) to solve the hierarchy problem that was previously presented. Taking into account a scalar particle S, with mass M_S, that couples with the Higgs boson with strength λ_S: the Lagrangian term of this coupling will be:

$$\mathcal{L} = \lambda_S |H|^2 |S|^2$$

giving rise to a scalar contribution to the Higgs mass (3.4b)

$$\delta m_H^2 = \frac{\lambda_S}{16\pi^2}\Lambda^2 + ... \tag{3.13}$$

Confronting Eq. 3.3 and Eq. 3.13, one can clearly see that if each fermion of the SM is accompanied by two scalars, each with $\lambda_S = |\lambda_f|^2$, the quadratic divergences coming from these two terms cancel each other, independently on the masses m_f, m_S and the value of the couplings λ_f, λ_S.
After the application of this "*Supersymmetry*" (SUSY) we find ourselves with

two scalar partners S for each fermion f of the SM, and these scalars also couples with the Higgs, contributing with mass corrections given by Eq. 3.13. Higher order interactions, which are not quadratically divergent, also contribute to the Higgs mass renormalization that depends on the mass slitting between the fermion and the partner scalars.
The remaining terms (the ones that do not cancel) are of the form[2]

$$\delta m_H^2 = \frac{\lambda}{16\pi^2}\left[m_f^2 \log\left(\frac{\Lambda}{m_f}\right) - m_S^2 \log\left(\frac{\Lambda}{m_S}\right)\right] \tag{3.14}$$

where λ stands for the various dimensionless couplings. In order to avoid considerable fine tuning and keep naturalness, these corrections must be of the same order (or not much greater) than the mass of the SM Higgs. Using $\Lambda \approx M_P$ and $\lambda \approx 1$ one finds that the masses of at least the lightest few superpartners should be of about 1 TeV, in order to provide a Higgs VEV resulting in the experimentally observed $m_W \approx 80$ GeV and $m_Z \approx 91$ GeV[3].
Going back to the previous paragraph, we have now an estimate on the scale at which the SM is no longer valid and must be substituted by its supersymmetric extension, that must be of the order of:

$$\mathcal{O}\left(|m_S^2 - m_f^2|\right) \leq \left((1\text{ TeV})^2\right) \tag{3.15}$$

Therefore, as long as the mass splitting between scalars and fermions is "small" (that means, of the order of Eq. 3.15), no unnatural cancellations will be required and the theory can be considered Natural.

3.3 The Minimal Supersymmetric Standard Model

We need to find a way to introduce these new particle states, partners of the existing SM particles. Since there are no candidates for these supersymmetric partners within the set already observed, we need to introduce a new set, doubling in fact the number of elementary particles. This eased extension of the Standard Model is referred to as the *Minimal Supersymmetric Standard Model* (MSSM) and couples the "old" SM particles and the new hypothetical "SUSY" partners in the so-called *supermultiplets*.
Each of the known fundamental particles is included in either a chiral or gauge supermultiplet and must have a *superpartner* with a spin differing by $\frac{1}{2}$ unit

- *Chiral supermultiplets:* a massless spin-$\frac{1}{2}$ Weyl fermion with two spin helicity states and two real scalar fields, assembled into a complex scalar field.
- *Gauge supermultiplets:* a massless spin-1 vector boson and a massless spin-$\frac{1}{2}$ Weyl fermion

In the Standard Model Lagrangian $\mathcal{L}_{SM}$, the requirements of renormalizability and gauge invariance set the conservation of two quantum numbers for both baryonic and leptonic decays:

[2]Other smaller contributions have been omitted
[3]The masses of the Intermediate Vector Bosons are highly sensible to the Higgs VEV

		spin 0	spin 1/2	$SU(3)_C$,$SU(2)_L$,$U(1)_\gamma$
squark, quarks	Q	$(\widetilde{u}_L\ \widetilde{d}_L)$	$(u_L\ d_L)$	(3,2,$\frac{1}{6}$)
($\times$3 generations)	$\bar{u}$	$\widetilde{u}^*_R$	$u^\dagger_R$	($\bar{3}$,1,-$\frac{2}{3}$)
	$\bar{d}$	$\widetilde{d}^*_R$	$d^\dagger_R$	($\widetilde{3}$,1,$\frac{1}{3}$)
sleptons, leptons	L	$(\widetilde{\nu}\ e_L)$	$(\nu\ e_L)$	(1,2,-$\frac{1}{2}$)
($\times$3 generations)	$\bar{e}$	$\widetilde{e}^*_R$	$e^\dagger_R$	(1,1,1)
Higgs, higgsinos	H_u	$(H^+_u\ H^0_u)$	$(\widetilde{H}^+_u\ \widetilde{H}^0_u)$	(1,2,+$\frac{1}{2}$)
	H_d	$(H^0_d\ H^-_d)$	$(\widetilde{H}^0_d\ \widetilde{H}^-_d)$	(1,2,-$\frac{1}{2}$)

Table 3.1: Chiral supermultiplets in the MSSM. The spin-0 fields are complex scalars; the spin-1/2 fields are left-handed two-component Weyl fermions.

	spin 1/2	spin 1	$SU(3)_C$,$SU(2)_L$,$U(1)_\gamma$
gluino, gluon	$\widetilde{g}$	g	(8,1,0)
winos, W bosons	$\widetilde{W}^\pm\ \widetilde{W}^0$	$W^\pm\ W^0$	(1,3,0)
bino, B boson	$\widetilde{B}^0$	B^0	(1,1,0)

Table 3.2: Gauge supermultiplets in the MSSM.

- Baryon Number $B = \frac{1}{3}(n_q - n_{\bar{q}})$
- Lepton Number $L = (n_\ell - n_{\bar{\ell}})$

On the contrary, in the supersymmetric theories it is possible to violate both, potentially leading to weak-scale proton decay[4].
The unwanted terms can be eliminated by imposing invariance under a new symmetry, known as R-parity. This new discrete symmetry is defined for each particle as:

$$R = (-1)^{3(B-L)+2J} \tag{3.16}$$

where B,L and J are respectively the baryon number, the lepton number and the spin. Having R = +1 for all SM particles and R = -1 for all SUSY particles, leads to some important phenomenological consequences:

- *Stability of the LSP:* The lightest *sparticle* (supersymmetric particle) with R = -1, referred as the lightest supersymmetric particle (LSP) must be stable, as it cannot decay in any SM particle violating R parity.
- Each sparticle other than the LSP must eventually decay into a state that contains an odd number of LSPs.
- Sparticles, starting with initial state particle, can only be produces in even numbers $R^{n+1} = -1$.

R-parity conservation holds automatically in many GUT models under rather general assumptions. Alternatively, weak-scale proton decay can also be avoided by imposing either baryon or lepton number conservation.

[4] $p^+ \to e^+ + \pi^0$

Supersymmetry breaking

If the supersymmetry is an exact symmetry, fermions and their bosonic superpartners must be degenerate in mass; however the experimental observation show no new particle states in the already observed mass spectrum of the SM. Thus, if supersymmetry is realized in nature, it must be a broken symmetry. Even in presence of symmetry breaking, supersymmetry can still provide a solution to the hierarchy problem if every quadratically divergent radiative correction to the Higgs scalar mass of the form

$$\Delta m_H^2 = \frac{1}{8\pi^2}(\lambda_S - |\lambda_f|^2)\Lambda_{UV}^2 + ... \tag{3.17}$$

gets cancelled. An option is to consider a "soft" supersymmetry breaking, meaning that the effective Lagrangian of the MSSM can be written as:

$$\mathcal{L} = \mathcal{L}_{SUSY} + \mathcal{L}_{soft} \tag{3.18}$$

where $\mathcal{L}_{SUSY}$ contains all of the gauge and Yukawa interactions and preserves supersymmetry invariance, and $\mathcal{L}_{soft}$ violates supersymmetry but contains only mass terms and coupling parameters with positive mass dimension.
In these way, the new soft terms introduces many parameters in the MSSM, such as mass terms for all the superpartners and trilinear A terms:

$$\begin{aligned}\mathcal{L}_{SOFT} = &-m_{H_d}^2|H_d|^2 - m_{H_u}^2|H_u|^2 + \mu B\epsilon_{ij}(H_d^i H_u^j + h.c.) - \frac{1}{2}M_1\widetilde{B}\widetilde{B} - \frac{1}{2}M_2\widetilde{W}\widetilde{W} \\ &-\frac{1}{2}M_3\widetilde{g}\widetilde{g} - M_{\widetilde{Q}}^2(\tilde{u}_L^*\tilde{u}_L + \tilde{d}_L^*\tilde{d}_L) - M_{\widetilde{U}}^2 u_R^* u_R - M_{\widetilde{D}}^2 d_R^* d_R - M_{\widetilde{L}}^2(\tilde{\ell}_L^*\tilde{\ell}_L + \tilde{\nu}_L^*\tilde{\nu}_L) \\ &-M_{\widetilde{E}}^2\ell_R^*\ell_R - \epsilon_{ij}(-\lambda_u A_u H_u^i \widetilde{Q}^j \tilde{u}_R^* + \lambda_d A_d H_d^i \widetilde{Q}^j \tilde{d}_R^* + \lambda_\ell A_E H_d^i \widetilde{L}^j \tilde{\ell}_R^*)\end{aligned} \tag{3.19}$$

where Q, L, H_u and H_d denote SU(2) weak doublets; a summation over generations is implied. From these considerations, we found that there is a total of 105 masses, phases and mixing angles in the MSSM that cannot be removed by redefining the phases and flavour basis from the quark and lepton supermultiplets.
Many of these parameters are however severely restricted by experimental observations and a phenomenologically viable MSSM can be defined by making the following three assumptions:

- All the soft SUSY-breaking parameters are real and therefore there is no new source of CP-violation generated, in addition to the one from the CKM matrix.

- The matrices for the sfermion masses and for the trilinear couplings are all diagonal, implying the absence of flavour-changing neutral current processes at the tree-level.

- First and second sfermion generation universality at low energy from constraints on experimental particle masses.

These assumptions reduce the total of 105 parameters to 22: the ration of the VEVs of the two-Higgs double fields, 2 Higgs mass parameters squared, 3 gaugino mass parameters, 5 first/second generation sfermion mass parameters, 5 third generation sfermion mass parameters, 3 first/second generation trilinear couplings and 3 third generation trilinear couplings.

3.4 The mass spectrum

In perfect parallelism with the SM, the superpartners listed in Tab. 3.1 and 3.2 are not necessarily also the mass eigenstates of the MSSM. After electroweak symmetry breaking and supersymmetry breaking effects are included, particles with the same quantum numbers will in general mix.

Higgs sector

The Higgs scalar fields in the MSSM is way more elaborate than the SM corresponding sector, consisting of two complex $\mathrm{SU}(2)_L$-doublets, H_u and H_d, or eight real, scalar degrees of freedom. After the electroweak symmetry is broken, three of them become the EW Nambu-Goldstone bosons, that are the longitudinal modes of the Z and $\mathrm{W}^{\pm}$ massive vector bosons. The remaining five degrees of freedom yield the physical Higgs bosons of the model:

- $H^{\pm}$*:* charged Higgs boson pair
- A^0*:* CP-odd neutral-charged Higgs boson
- H^0, h^0*:* CP-even neutral-charged Higgs bosons [5]

If $m_{A^0} \gg M_Z$ (decoupling limit), the particles A^0, H^0 and $\mathrm{H}^{\pm}$ are much heavier than h^0, nearly degenerated and decoupled from low-energy experiments.
In contrast, the mass of h^0 is upper bounded, the bound being $m_{h^0} \lesssim 135$ GeV, consistent with the experimental observation. This bound can be weakened if all the couplings in the theory are required to remain perturbative up to the unification scale, or if the top squarks are heavier than ~ 1 Tev, but the upper bound rises only logarithmically with the soft masses in the loop corrections. Thus supersymmetry at the electroweak scale predicts that at least one of the Higgs scalar bosons must be light.

Charginos and neutralinos

The charged Higgsinos ($\widetilde{H}_u^+$ and $\widetilde{H}_d^-$) and winos ($\widetilde{W}^+$ and $\widetilde{W}^-$), due to the effects of electroweak symmetry breaking, mix to form two spin-$\frac{1}{2}$ charged sparticles (with charge ± 1) called "*charginos*" $\widetilde{\chi}_i^{\pm}$ with the matrix in the (W^+,H^+) basis:

$$\begin{pmatrix} M_2 & \sqrt{2}M_W \sin\beta \\ \sqrt{2}M_W \cos\beta & \mu \end{pmatrix}$$

[5] With h^0 being lighter by convention

The neutral Higgsinos ($\widetilde{H}_u^0$ and $\widetilde{H}_d^0$) and neutral electroweak gauginos (($\widetilde{B}$ and $\widetilde{W^+}$)) form four spin-$\frac{1}{2}$ neutral particles called "neutralinos" $\widetilde{\chi}_i^0$ with the mass matrix in the (B, W^0, H_d, H_u) basis:

$$\begin{pmatrix} M_1 & 0 & -M_Z\ \cos\beta\ \sin\theta_W & M_Z\ \sin\beta\ \sin\theta_W \\ 0 & M_1 & M_Z\ \cos\beta\ \cos\theta_W & M_Z\ \sin\beta\ \cos\theta_W \\ -M_Z\ \cos\beta\ \sin\theta_W & M_Z\ \cos\beta\ \cos\theta_W & 0 & -\mu \\ M_Z\ \sin\beta\ \sin\theta_W & -M_Z\ \sin\beta\ \cos\theta_W & -\mu & 0 \end{pmatrix}$$

θ_W being the Weinberg angle of EW mixing and tanβ is the ratio of the VEVs of the two Higgs doublets.

The lightest neutralino χ_1^0 is usually assumed to be the LSP.
In general the mass eigenstates and their corresponding eigenvalues are complicated mixtures of the gauge interaction eigenstates and the phenomenology of the different SUSY models strongly depends on this mixing. However, in most models of supersymmetry breaking it is possible to write the following relations:

$$\frac{M_1}{\alpha_1} = \frac{M_2}{\alpha_2} = \frac{M_3}{\alpha_3} \tag{3.20}$$

with the mass terms μ that is of order of $M_{\tilde{g}}$. The consequence is that the two lighter neutralinos and the lighter chargino are dominantly gaugino, while the heavier states are dominantly Higgsino and weakly coupled to the first two generations.

Gluino

The gluino is a color octet fermion, so it cannot mix with any other particle in the MSSM, even if R-parity is violated. The gaugino mass parameter (M_3) is related to the bino and wino mass parameters (M_1 and M_2, respectively), by Eq. 3.20 with an approximate

$$M_3 : M_2 : M_1 \simeq 6 : 2 : 1 \tag{3.21}$$

ratio [12]. Therefore, in models where relation 3.20 holds, is reasonable to suspect that gluino is considerably heavier than the lighter neutralinos and charginos.

Squark and sleptons

Concerning the sfermion sector, while chiral fermions f_L, f_R must have the same mass by Lorentz invariance, their scalar partners $\widetilde{f_L}, \widetilde{f_R}$ instead may have different masses. Their squared mass matrix get off-diagonal contributions proportional to the fermion mass with the result that this left-right mixing is only important for the third generation. These eigenstates are calles $\widetilde{t}_{1,2}(stop), \widetilde{b}_{1,2}(sbottom), \widetilde{\tau}_{1,2}(stau)$. In general, it is expected a hierarchy like $m_{squark} > m_{sleptons}$ in most of the SUSY models, because the contributions to squark masses from the gluino are always present and usually quite large, since QCD has a larger gauge coupling than the electroweak interactions.

Names	Spin	P_R	Gauge Eigenstates	Mass Eigenstates
Higgs bosons	0	+1	$H_u^0\ H_d^0\ H_u^+\ H_d^-$	$h^0\ H^0\ A^0\ H^\pm$
squarks	0	-1	$\tilde{u}_L\ \tilde{u}_R\ \tilde{d}_L\ \tilde{d}_R$ $\tilde{s}_L\ \tilde{s}_R\ \tilde{c}_L\ \tilde{c}_R$ $\tilde{t}_L\ \tilde{t}_R\ \tilde{b}_L\ \tilde{b}_R$	$\tilde{u}_L\ \tilde{u}_R\ \tilde{d}_L\ \tilde{d}_R$ $\tilde{s}_L\ \tilde{s}_R\ \tilde{c}_L\ \tilde{c}_R$ $\tilde{t}_1\ \tilde{t}_2\ \tilde{b}_1\ \tilde{b}_2$
sleptons	0	-1	$\tilde{e}_L\ \tilde{e}_R\ \tilde{\nu}_e$ $\tilde{\mu}_L\ \tilde{\mu}_R\ \tilde{\nu}_\mu$ $\tilde{\tau}_L\ \tilde{\tau}_R\ \tilde{\nu}_\tau$	$\tilde{e}_L\ \tilde{e}_R\ \tilde{\nu}_e$ $\tilde{\mu}_L\ \tilde{\mu}_R\ \tilde{\nu}_\mu$ $\tilde{\tau}_1\ \tilde{\tau}_2\ \tilde{\nu}_\tau$
neutralinos	$\frac{1}{2}$	-1	$\widetilde{B}^0\ \widetilde{W}^0\ \widetilde{H}_u^0\ \widetilde{H}_d^0$	$\widetilde{N}_1\ \widetilde{N}_2\ \widetilde{N}_3\ \widetilde{N}_4$
charginos	$\frac{1}{2}$	-1	$\widetilde{W}^\pm\ \widetilde{H}_u^+\ \widetilde{H}_d^-$	$\widetilde{C}_1^\pm\ \widetilde{C}_2^\pm$
gluino	$\frac{1}{2}$	-1	$\widetilde{g}$	$\widetilde{g}$
goldstino/gravitino	$\frac{1}{2}/\frac{3}{2}$	-1	$\widetilde{G}$	$\widetilde{G}$

Table 3.3: The supersymmetric partners of the SM particles in the MSSM (with fermion mixing for the first two families assumed to be negligible).

As no experimental evidence of superpartners with masses identicals to the SM particles has been found yet, it becomes clear that if SUSY is realized in nature, it must be a broken symmetry. In the MSSM, there are 32 distinct masses corresponding to the supersymmetric partners of the SM particles (listed in Tab. 3.3), not including the gravitino.
The direct inputs from the LHC experiments have already presented strong limits on the squarks of the first two generations, constraining them to be heavier than 1 TeV [9].
Naturalness points toward the possibility that squark soft masses are not flavour degenerate, therefore shifting the focus on the particles that give the largest contributions to the Higgs mass corrections: the *higgsino*, the *top squark* (and left-handed bottom squark, due to the SM weak isospin symmetry) and *gluino*.
The Naturalness in the MSSM can be summarized by:

$$-\frac{m_Z^2}{2} = |\mu|^2 + m_{H_u}^2 \tag{3.22}$$

The direct consequence of this equation is that higgsinos must be light because their mass is directly controlled by μ. If we define

$$\Delta \equiv \frac{2\delta m_H^2}{m_h^2} \tag{3.23}$$

with $m_h^2 = -2m_H^2$ as a measure of fine-tuning, we get that

$$|\mu| \leq 200\text{GeV} \left(\frac{m_h}{125\ \text{GeV}}\right) \left(\frac{\Delta^{-1}}{20\%}\right)^{-\frac{1}{2}} \tag{3.24}$$

At loop level we find additional constraints. The Higgs potential is corrected by both gauge ($A_t y_t \tilde{q}_3 \tilde{u}_3 H_u$) and Yukawa ($-y_t \tilde{q}_3 u_3 H_u$) interactions, with the largest contribution being the top quark-squark loop. This is given by

$$\delta m_{H_u}^2|_{\tilde{t}} = -\frac{3}{8\pi^2} y_t^2 \left(m_{Q_3}^2 + m_{u_3}^2 + |A_t|^2\right) \log\left(\frac{\Lambda}{\text{TeV}}\right) \tag{3.25}$$

where Λ is the scale at which sfermion masses are generated. This translates in a boundary on the heaviest top squark via

$$\sqrt{m_{\tilde{t}_1}^2 + m_{\tilde{t}_2}^2} \leq 600\text{GeV} \frac{\sin\beta}{(1+x_t^2)^{1/2}} \left(\frac{\log(\Lambda/\text{TeV})}{3}\right)^{-1/2} \left(\frac{m_h}{125\text{GeV}}\right) \left(\frac{\Delta^{-1}}{20\%}\right)^{-1/2} \tag{3.26}$$

where $x_t = \frac{A_t}{\sqrt{m_{\tilde{t}_1}^2 + m_{\tilde{t}_2}^2}}$.

All the other SM particles give much smaller radiative contributions to the Higgs potential and hence less stringent limits on the SUSY spectrum. The only exception to this rule is the gluino, which induces a large correction to the top squark masses at 1-loop and therefore feeds into the Higgs potential at two loops.

This correction, neglecting the mixed $A_t M_3$ contributions, is given by

$$\delta m_{H_u}^2|_{\tilde{g}} = -\frac{2}{\pi^2}\, y_t^2 \, \left(\frac{\alpha_S}{\pi}\right) \, |M_3|^2 \log^2\left(\frac{\Lambda}{\text{TeV}}\right) \tag{3.27}$$

where M_3 is the gluino mass. This corrections can also be translated in a naturalness bound on the gluino mass

$$M_3 \leq 900\text{GeV} \, \sin\beta \left(\frac{\log(\Lambda/\text{TeV})}{3}\right)^{-1} \left(\frac{m_h}{125\text{GeV}}\right)) \left(\frac{\Delta^{-1}}{20\%}\right)^{-1/2} \tag{3.28}$$

corresponding to an upper limit of about 1.5 TeV.

Chapter 4

$\widetilde{t}$ physics

The study of the phenomena introduced in the previous chapter is by itself sterile, if not supported by the observation of the aforementioned states in nature: it is therefore of primary importance to establish the impact of these supersymmetrical objects on the phenomenology of proton-proton interactions at the LHC energies.
The starting point in the search for MSSM particles is that radiative stability between the weak scale and the LHC effective theory scale of $\sim$ 10 TeV does not require a superpartner for every SM particle, but just for those particles with strong ($\sim \mathcal{O}(1)$) coupling to the Higgs Boson and electroweak breaking. In the contest of the masses reachable by this effective theory, the content of a minimal superpartner extension is therefore given [14] by third generation squarks (stop and sbottom), two Higgsinos and gluinos, without sleptons or first and second generations squarks; of these third generation states, the stop squark is also expected to inherit from the t quark a strong coupling with the Higgs boson and its existence at masses lower than the TeV could be a key to solve the naturalness problem. The masses of the omitted superpartners may be well above the LHC reach and not affect the phenomenology of the physics processes at the current achievable energy.
A typical spectrum of a SUSY model, as presented in Fig. 4.1, shows that third generation squarks are expected to be lighter ($\mathcal{O}(TeV)$) than the other squarks and their production may therefore be abudant at the LHC.

4.1 Squark masses and mixing

It is important to notice that the stop squark mass eigenstates are not the helicity eigenstates $\widetilde{t}_L$ and $\widetilde{t}_R$, as these two states have a non negligible mixing. These left-handed and right-handed squarks strongly mix to form the mass eigenstates $\widetilde{t}_1$ and $\widetilde{t}_2$, with $\widetilde{t}_1$ lighter by convention. For a generic sfermion $\widetilde{f}$ the mass matrix determining the magnitude of the mixing is given by:

$$M_f^2 = \begin{bmatrix} m_{LL}^2 & m_f \widetilde{A}_f \\ m_f \widetilde{A}_f & m_{RR}^2 \end{bmatrix} \tag{4.1}$$

whose elements are given, in terms of the soft SUSY-breaking scalar masses $m_{\widetilde{f_L}}$ and $m_{\widetilde{f_R}}$, the trilinear coupling A_f, the higgsino mass parameter μ and

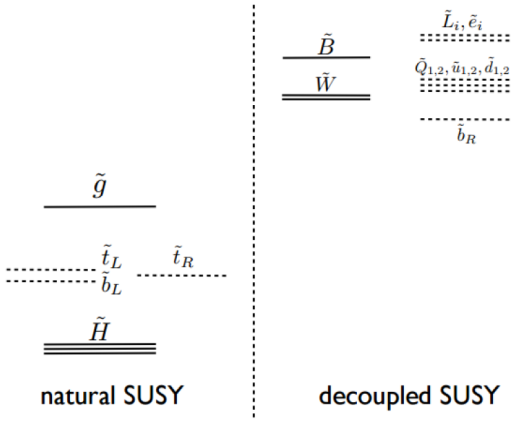

Figure 4.1: Mass hierarchy of a possible MSSM decoupled SUSY model. Masses on the left (Natural SUSY) are expected to have masses not much higher than ∼1 TeV. Masses on the left (decoupled SUSY) may be extremely high, out of the reach of the current (and possibly near future) particle physics experiment.

the ratio of the vacuum expectation values of the two-Higgs doublet fields $\tan(\beta = v_u/v_D)$, by:

$$\begin{aligned} m^2_{LL} &= m^2_f + m^2_{\widetilde{f}_L} + (I^3_f - e_f s^2_W)\cos(2\beta)M^2_Z \\ m^2_{RR} &= m^2_f + m^2_{\widetilde{f}_R} + e_f s^2_W \cos(2\beta)M^2_Z \\ \widetilde{A}_f &= A_f - \mu(\tan(\beta))^{-2I^3_f} \end{aligned} \tag{4.2}$$

where e_f and I^3_f are the electric charge and weak isospin of the sfermion $\widetilde{f}$ and $s^2_W = 1 - c^2_W \equiv sin^2\theta_W$. The sfermionic mass matrices are diagonalized by 2×2 rotation matrices of angle θ_f

$$\begin{aligned} \begin{pmatrix} \widetilde{f}_1 \\ \widetilde{f}_2 \end{pmatrix} &= \mathcal{R}^{\widetilde{f}} \begin{pmatrix} \widetilde{f}_L \\ \widetilde{f}_R \end{pmatrix} \\ \mathcal{R}^{\widetilde{f}} = \begin{pmatrix} c_{\theta_f} & s_{\theta_f} \\ -s_{\theta_f} & c_{\theta_f} \end{pmatrix}, with & \begin{matrix} c_{\theta_f} \equiv \cos(\theta_f) \\ s_{\theta_f} \equiv \sin(\theta_f) \end{matrix} \end{aligned} \tag{4.3}$$

The mixing angle θ_f and the squark mass eigenstates are then given by

$$\begin{aligned} \sin(\theta_f) &= \frac{-m_f \widetilde{A}_f}{\sqrt{(m^2_{LL} - m^2_{\widetilde{f}_1})^2 + m^4_f \widetilde{A}^4_f}} \\ \cos(\theta_f) &= \frac{m^2_{LL} - m^2_{\widetilde{f}_1}}{\sqrt{(m^2_{LL} - m^2_{\widetilde{f}_1})^2 + m^4_f \widetilde{A}^4_f}} \\ m^2_{\widetilde{f}_{1,2}} &= \frac{1}{2}\left[m^2_{LL} + m^2_{RR} \mp \sqrt{(m^2_{LL} - m^2_{RR})^2 + 4m^2_f \widetilde{A}^2_f}\right] \end{aligned} \tag{4.4}$$

To keep the scale of the electroweak symmetry breaking natural, the super-partners are expected to have masses around or beneath the TeV scale. In

particular, since the largest coupling to the Higgs in the SM is from the top quark, the superpartners of the top quark play the most important role in cancelling the quadratic divergence and are expected to be close to the weak scale in a natural theory [64].

On the other hand, the Higgs boson mass of 125 GeV also has important implications for the stop masses. In the minimal supersymmetric standard model (MSSM), the tree-level Higgs boson mass has an upper bound of M_Z. To get to 125 GeV, it requires large radiative contributions from the stop loops. This could happen if the stops are heavy and/or the trilinear A_t term of the stop sector is large. To keep the fine-tuning minimal, it is preferable to have a large A_t term so that the stops masses can be lowered to ~ 1 TeV or below. A large A_t term implies large off-diagonal masses of the stop mass matrix so there will be a substantial mixing between the left-handed and the right-handed stops in the mass eigenstates. As a consequence, there will also be a sizeable mass difference between the two stop mass eigenstates.

4.2 Simplified model decay modes

The foundation of the observation of BSM states lies in the discrimination of the signal that these particles produce by decaying inside our detector in states that we can observe; it is therefore essential to be in full control of the relevant decay modes of the particle of interest in the entire kinematic region accessible by our experiment.
Not wanting to limit our search to a single specific SUSY model, it is possible to notice that in the framework of a generic R-parity-conserving MSSM, supersymmetric particles are always produced in pairs and the lightest superstate, which is usually assumed to be the lightest neutralino $\widetilde{\chi}_1^0$, is stable.

The direct production of top squarks at LHC can be explored using long decay chains, in order be able to discriminate its complex signature from the SM background.
The decay modes of the top squark depend on the SUSY particle mass spectrum. In the rest of this work, for simplicity, only the two top squarks and the lightest neutralino are considered as the active SUSY particles; the other SUSY particles are assumed to be heavy enough (with masses of the order of TeV) such that they decouple and are not accessible by our experiment.

$\widetilde{t}_i$ decay modes

Stop$_1$ $\widetilde{t}_1$**:** The lightest top squark decay modes [23], shown in Fig. 4.2, will be described in the following. Being the stop sensitive to strong interaction, the decay of the stop in a gluino and the respective quark (if kinematically allowed) is expected to dominate, due to the high QCD coupling of the quark-squark-gluino vertex:

$$\widetilde{q} \rightarrow q\widetilde{g} \tag{4.5}$$

As the experimental searches of the gluino pushes higher and higher the lower limit of the gluino masses (Fig. 4.3), it becomes clear that this decay is not

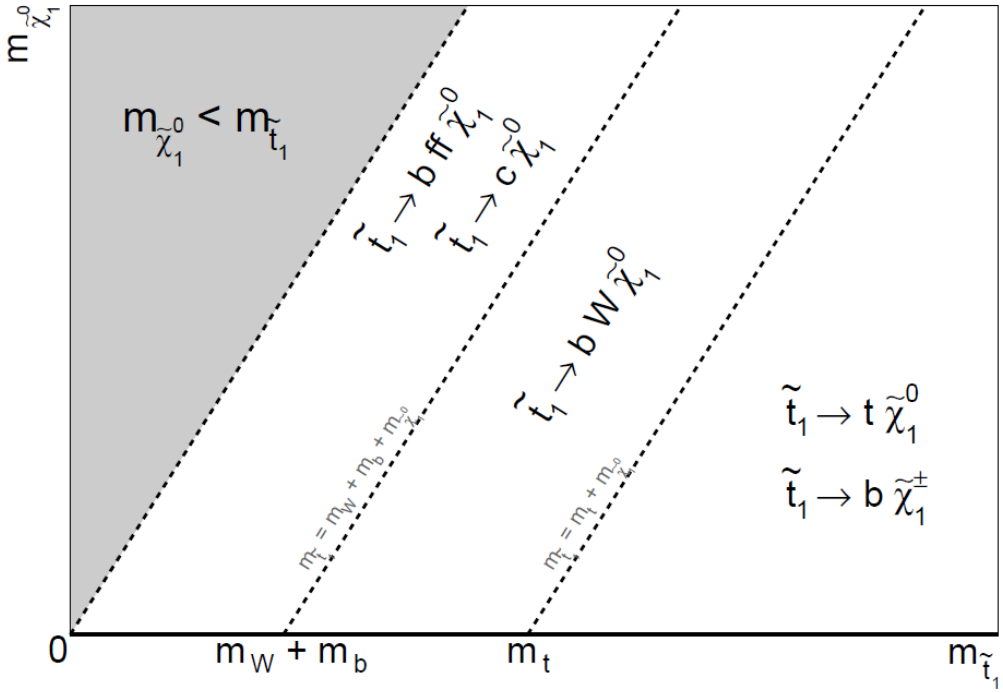

Figure 4.2: Lightest stop squark mass eigenstate $\widetilde{t}_1$ decay modes as a function of the top squark ($\widetilde{t}_1$) and lightest neutralino masses ($\widetilde{\chi}_1^0$).

a feasible way to search for $\widetilde{t}_1$ at LHC. In regions where the gluino decay is not allowed, the squark may decay, depending on its mass, into a quark plus a neutralino $\widetilde{\chi}_i^0$ or a chargino $\widetilde{\chi}_i^{\pm}$; if the top squarks are heavy enough, their main decay modes will be into top quark and neutralinos:

$$\widetilde{t}_i \to\ t\ \widetilde{\chi}_j^0\ [j = 1-4],\ for\ (m_{\widetilde{t}_i} > m_t + m_{\widetilde{\chi}_j^0}) \tag{4.6}$$

and two-body bottom quarks and charginos:

$$\widetilde{t}_i \to\ b\ \widetilde{\chi}_j^{\pm}\ [j = 1-2],\ for\ (m_{\widetilde{t}_i} > m_b + m_{\widetilde{\chi}_j^{\pm}}) \tag{4.7}$$

or three-body decay:

$$\widetilde{t}_1 \to\ b\ W\ \widetilde{\chi}_1^0 \tag{4.8}$$

If even this third decay is kinematically closed, then only the flavour-suppressed decay to a charm quark:

$$\widetilde{t}_1 \to\ c\ \widetilde{\chi}_1^0,\ for\ (m_{\widetilde{t}_1} > m_c + m_{\widetilde{\chi}_1^0}) \tag{4.9}$$

and the four-body decay:

$$\widetilde{t}_1 \to\ b\ f\ f^{'}\ \widetilde{\chi}_1^0 \tag{4.10}$$

remains viable options. These decays are suppressed by phase space, so that the lightest stop can be quasi-stable on the time-scale relevant for collider physics, and can hadronize into bound-states.
Three- and four- body decay of the stop, even though possible, are strongly suppressed with respect to the two- body decays.

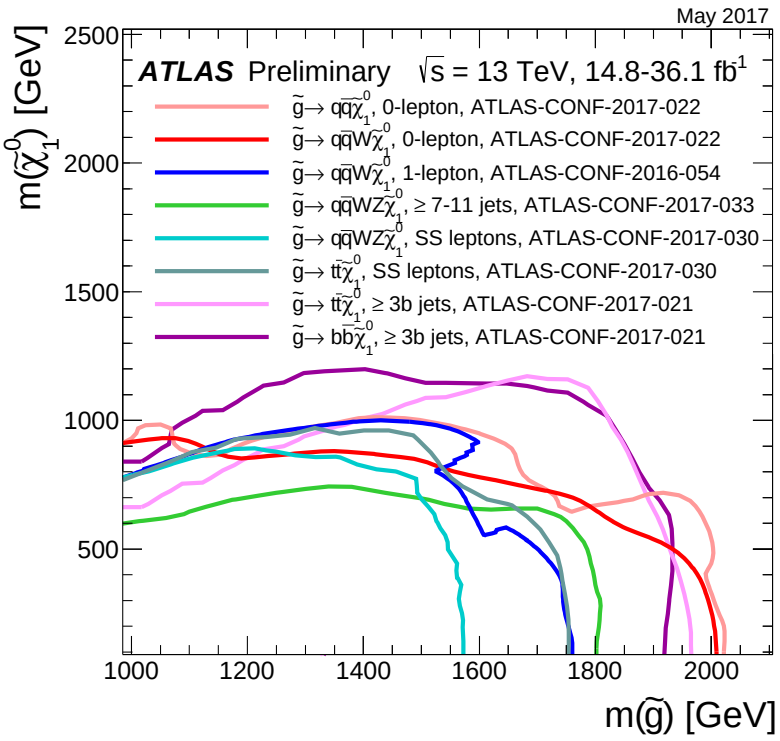

Figure 4.3: Exclusion limits at 95% CL for 13 TeV in the (gluino, lightest neutralino) mass plane for different simplified models featuring the decay of the gluino to the lightest neutralino either directly or through a cascade chain featuring other SUSY particles with intermediate mass. For each line, the gluino decay mode is reported in the legend and it is assumed to have 100% branching ratio.

Stop$_2$ $\widetilde{t}_2$**:** in addition to the decay modes accessible to the $\widetilde{t}_1$, the heavier $\widetilde{t}_2$ can also decay in $\widetilde{t}_1$ plus a Higgs or Z boson, if the mass difference between the two mass eigenstates is big enough:

$$\begin{aligned} \widetilde{t}_2 &\rightarrow \widetilde{t}_1\ h,\ for\ (m_{\widetilde{t}_2} > m_{\widetilde{t}_1} + m_h) \\ \widetilde{t}_2 &\rightarrow \widetilde{t}_1\ Z,\ for\ (m_{\widetilde{t}_2} > m_{\widetilde{t}_1} + m_Z) \end{aligned} \tag{4.11}$$

The $\widetilde{t}_1$ created in this decay is boosted and leaves high E_{T}^{miss} (due to the $\widetilde{\chi}_0^0$ in the decay chain), which can be used, together with the signature of the h or Z decay, to detect the production of $\widetilde{t}_2$ at the collider.

$\widetilde{\chi}_j^0$ decay modes

Neutralinos can contain at least a small admixture of electroweak gauginos $\widetilde{B}$, $\widetilde{W}^0$ or $\widetilde{W}^{\pm}$, inheriting the coupling of weak interaction strenght to scalar pairs. If there is at least a slepton of squark sufficiently light, a neutralino can therefore decay into lepton+slepton or quark+squark.

$$\widetilde{\chi}_i^0 \rightarrow\ \ell\widetilde{\ell},\ \nu\widetilde{\nu} \tag{4.12}$$

A neutralino may also decay into any lighter neutralino plus a Higgs scalar or electroweak gauge boson, because they inherit the gaugino-higgsino-Higgs and $SU(2)_L$ gaugino-gaugino-vector boson couplings of their components.

$$\begin{aligned} \widetilde{\chi}_i^0 &\rightarrow \widetilde{\chi}_j^0 + h \\ \widetilde{\chi}_i^0 &\rightarrow \widetilde{\chi}_j^0 + Z \\ \widetilde{\chi}_i^0 &\rightarrow \widetilde{\chi}_j^{\pm} + W \ , with\ j < i \end{aligned} \tag{4.13}$$

If these decays are kinematically forbidden for a given neutralino, it can be subject to a three-body decay.

$$\widetilde{\chi}_i^0 \rightarrow ff + \widetilde{\chi}_j^0, ff' + \widetilde{\chi}^{\pm} \tag{4.14}$$

where f, f' are generic leptons or quarks, members of the same $SU(2)_L$ multiplet. These decays are mediated by the same gauge bosons, Higgs scalars, sleptons or squarks that appeared in the two-body decay, but the mediator is now off-shell and the decay rate is strongly suppressed.

4.3 Search for the $\widetilde{t}_2$ at the LHC

Assuming that the lightetst neutralino $\widetilde{\chi}_1^0$ is the lightest supersymmetric particle (LSP) and is stable, the search limit for the $\widetilde{t}_1 \rightarrow \widetilde{\chi}_1^0 + t$ decay (assuming 100% branching fraction) has reached $\sim$ 750 GeV for $m_{\widetilde{\chi}_1^0} < 200$ GeV at the Run 1 of LHC. From naturalness point view, some fine-tuning is already required if the lightest stop is heavier than 750 GeV and previous searches for the lightest stop have put strong constraints on its mass[22], as seen in Fig. 4.4[21], but there is still a gap in the low mass region not covered by searches: the gap covers the region in which the spectrum of the stop and the lightest neutralino is compressed, that is if:

$$m_{\widetilde{t}_1} - m_{\widetilde{\chi}_1^0} \simeq m_t \tag{4.15}$$

In this case the top quark and the neutralino from the stop decay are roughly at rest in the stop rest frame. For the stop pair production, the neutralinos travel along with the stops and their momenta tend to balance each other, leaving little E_{T}^{miss} in the signal. Consequently, it is difficult to distinguish the $\widetilde{t}_1$ decay from the SM top pair production background.
A promising strategy is to consider the stop pair production with an hard *Initial State Radiation* (ISR) jet; this would cause the neutralinos to be boosted in the opposite direction to the ISR jet, enhancing the E_{T}^{miss}.
Since naturalness needs both stops to be not too heavy, if $\widetilde{t}_1$ happens to lie in the compressed region, it may be easier to search for $\widetilde{t}_2$ even though it is heavier and closer to the energy limit of the LHC. The targeted decay chain, shown in Fig. 4.5 is:

$$\widetilde{t}_2 \rightarrow \widetilde{t}_1 + h \rightarrow t + \widetilde{\chi}_1^0 + b\bar{b} \tag{4.16}$$

For this search has been adopted a simplified model approach, assuming that the heavier stop $\widetilde{t}_2$ decays to the lighter stop $\widetilde{t}_1$ plus a Higgs boson ($\widetilde{t}_2 \rightarrow \widetilde{t}_1 + h$)

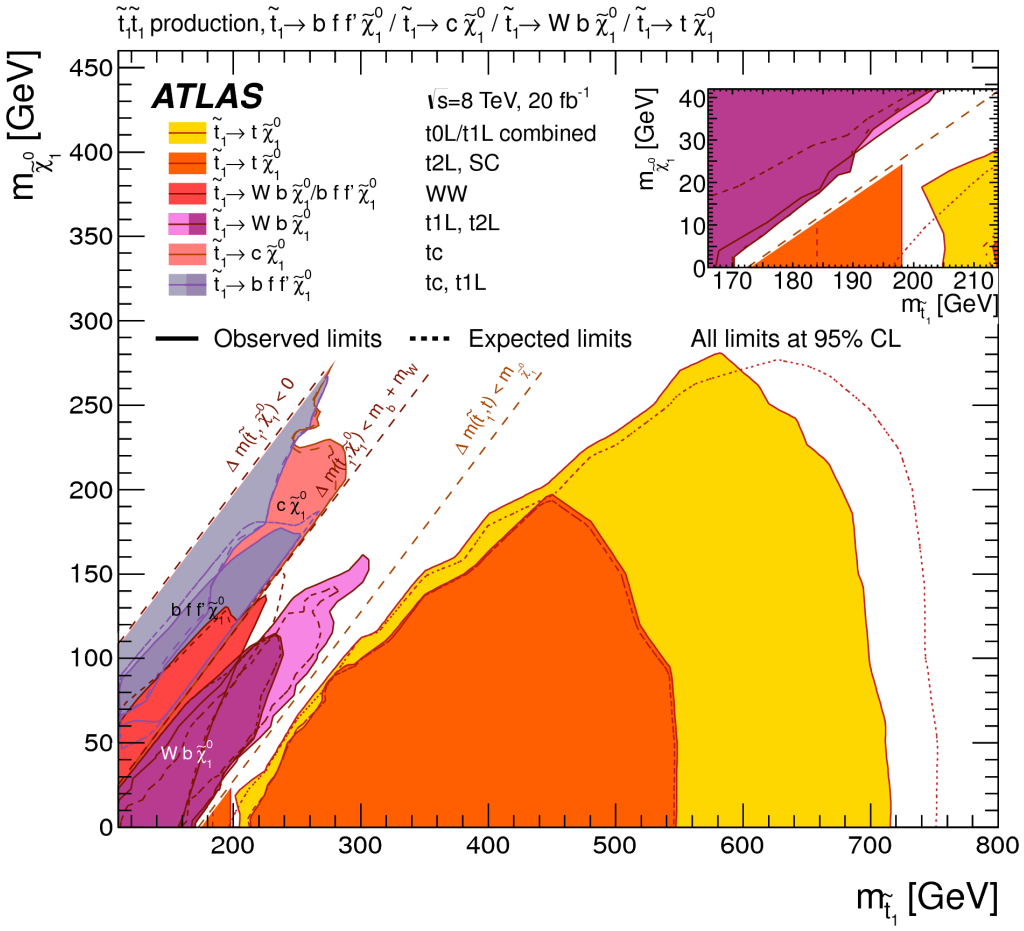

Figure 4.4: Summary of the dedicated ATLAS searches for top squark (stop) pair production based on 20 fb^{-1} of pp collision data taken at $\sqrt{s} = 8$ TeV. Exclusion limits at 95% CL are shown in the $\widetilde{t}_1 - \widetilde{\chi}_1^0$ mass plane. The dashed and solid lines show the expected and observed limits, respectively, including all uncertainties except the theoretical signal cross section uncertainty (PDF and scale). Four decay modes are considered separately with 100% BR: $\widetilde{t}_1 \rightarrow t + \widetilde{\chi}_1^0$, $\widetilde{t}_1 \rightarrow W + b + \widetilde{\chi}_1^0$ (3-body decay for $m_{\widetilde{t}_1} < m_t + m_{\widetilde{\chi}_1^0}$), $\widetilde{t}_1 \rightarrow c + \widetilde{\chi}_1^0$ and $\widetilde{t}_1 \rightarrow f + f' + b + \widetilde{\chi}_1^0$ (4-body decay). The latter two decay modes are superimposed. The region $\widetilde{t}_1$ mass below 100 GeV has not been considered for the 4-body decay. Note that these plots overlay contours belonging to different stop decay channels, different sparticle mass hierarchies, and simplified decay scenarios. Care must be taken when interpreting them.

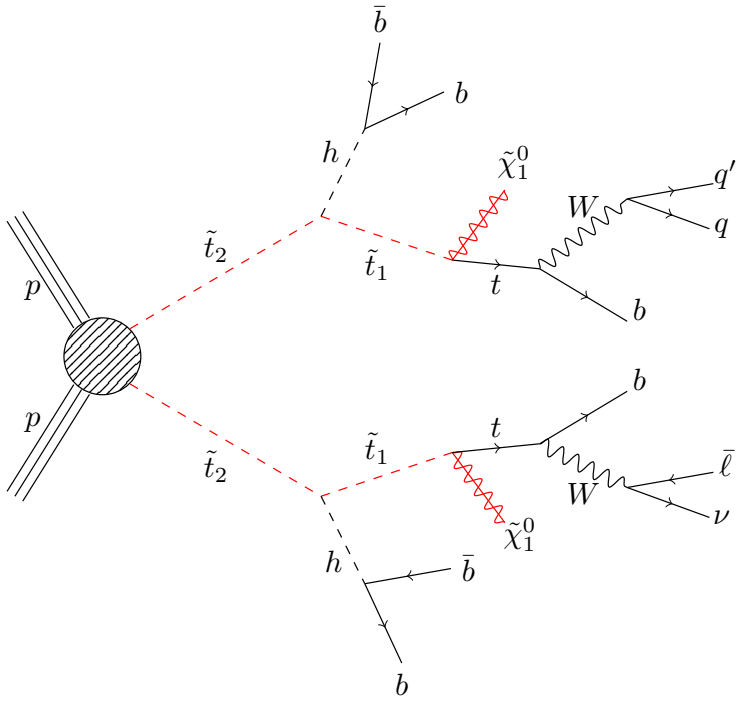

Figure 4.5: Decay chain of a pair produced $\widetilde{t}_2$ quarks in $\widetilde{t}_1$ and a Higgs boson h, assuming $\mathcal{B}(\widetilde{t}_2 \rightarrow \widetilde{t}_1 + h) = 1$. The $\widetilde{t}_1$ decays in a top quark and a lightest LSP neutralino $\widetilde{\chi}_1^0$ with $\mathcal{B}(\widetilde{t}_2 \rightarrow \widetilde{t}_1 + h) = 1$. The Higgs boson is expected to decay into a $b\bar{b}$ pair.

with a 100% branching fraction. In a realistic supersymmetric spectrum, there is always a sbottom lighter than the second stop, hence the decay patterns are usually more complicated than the simplified model assumptions. In particular, there are often large branching ratios of the decays $\widetilde{t}_2 \rightarrow \widetilde{b}_1\, W$ and $\widetilde{b}_1 \rightarrow \widetilde{t}_1 W$ as long as they are open. The decay chains can be even more comples if there are intermediated states of additional charginos and neutralinos in the decays.

Previous ATLAS searches have used 20.3fb^{-1} of pp collisions at $\sqrt{s} = 8$ TeV to place constraints on the $\widetilde{t}_2$ mass, excluding models with $m_{\widetilde{t}_2} < 525$ GeV for $m_{\widetilde{\chi}_1^0} < 240$ GeV and $m_{\widetilde{t}_2} < 600$ GeV for $m_{\widetilde{\chi}_1^0} < 200$ GeV and assuming different branching ratios to the targeted final state. A similar analysis, based on 13.3 fb^{-1} of $\sqrt{s} = 13$ TeV pp collisions recorder by the ATLAS experiment at the LHC in 2015 and 2016 excluded $m_{\widetilde{t}_2} < 730$ GeV for $m_{\widetilde{\chi}_1^0} < 325$ GeV at 95% confidence level.

4.4 Data samples

The experimental data used in this analysis correspond to $\sqrt{s} = 13$ TeV pp collisions collected by ATLAS during 2015 (periods D-H and J) and in 2016 (period A-L), selecting only events from data taking periods in which LHC beams were stable and all ATLAS detectors were operational.
A total of 3.9 fb^{-1} of integrated luminosity were recorded during 2015 (Fig.

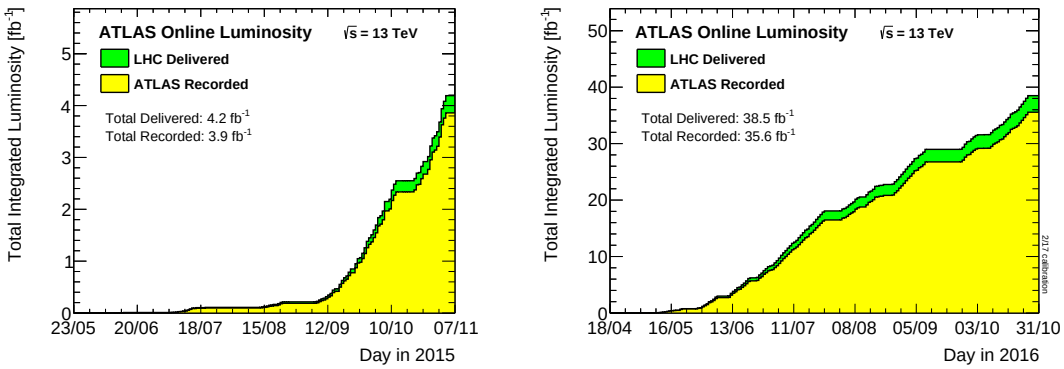

Figure 4.6: Total integrated luminosity delivered by LHC (green) and recorded by ATLAS (yellow) during 2015 (left) and 2016 (right). During both years, the accelerator operated in stable pp beam condition at an energy of 13 TeV centre-of-mass energy.

4.6a) and another $\sim$35.6 fb^{-1} during 2016 (Fig. 4.6b). The analysis was performed on a combined total of 36.1 fb^{-1} of data from these data-taking periods, with an uncertainty of $\pm$2.1% for the entire 2015+2016 period.

4.5 Signal samples

The signal models were generated in the context of a simplified model containing only the $\widetilde{t}_2$, the $\widetilde{t}_1$ and the $\widetilde{\chi}_1^0$. A signal grids has been generated, varying the values of the $\widetilde{t}_2$ and $\widetilde{\chi}_1^0$ masses, while keeping the mass difference between $\widetilde{t}_2$ and $\widetilde{t}_1$ close to the top-quark mass ($\Delta m(\widetilde{t}_2, \widetilde{t}_1) = 180$ GeV). In this simplified signal grid the $\widetilde{t}_2$ is required to decay into $\widetilde{t}_1 + h$ with 100% BR. The signal grid is shown in Fig. 4.7 and for each signal model the total number of generated event is reported.
MonteCarlo (MC) simulated event samples are used to model the SUSY signal and those SM backgrounds with two or more real leptons in the final state. The MC samples are processed by an ATLAS detector simulation based on GEANT4, or a fast simulation that uses a parametrisation of the calorimeter response and GEANT4 for the other parts of the detector, and are reconstructed with the same algorithms as used for the data. The coverage of this new signal grid greatly extends the mass parameter space excluded in Run-1 (Fig. 4.8).
A total of 790.000 events were generated, divided among the 67 different models, for an equivalent integrated luminosity of 250 fb^{-1}.

The SUSY signal samples are generated from Leading Order matrix element with up to two extra partons, using the MADGRAPH5_aMC@NLOv2.2.3 generator interfaced to PYTHIA8.186, with the A14 tune, for the modelling of the SUSY decay chain, parton showering, hadronisation and the description of the underlying events. Parton luminosities are provided by the NNPDF23LO PDF set.

The matching between tree level jets and parton shower is accomplished following the CKKW-L prescription [47], with a matching scale set to one quarter

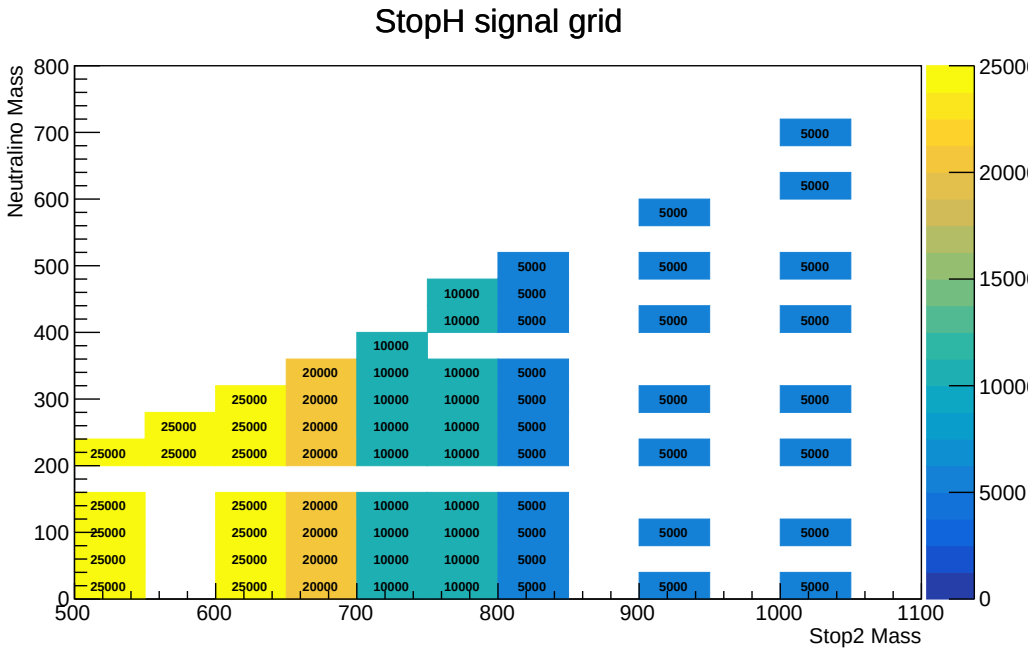

Figure 4.7: Number of events generated for each simplified signal model in the $\widetilde{t}_2 - \widetilde{\chi}_1^0$ mass plane with a 100% BR of $\widetilde{t}_2 \to \widetilde{t}_1 + h$ considered for the optimisation and interpretation of the analysis.

of the pair-produced superpartner mass. Signal cross sections are calculated to next-to-leading order in the strong coupling constant, adding the resummation of soft gluon emission at next-to-leading-logarithmic accuracy (NLO+NLL) [29, 48, 49]. The nominal cross section and the uncertainty are taken from an envelope of cross section predictions using different PDF sets and factorization and renormalisation scales, as described in Ref.[50]. The production cross section of top squark pairs with a mass of 500 GeV is 518 fb at $\sqrt{s} = 13$ TeV (compared with 86 fb at $\sqrt{s} = 8$ TeV).
All the signal MC samples were generated using a 25-ns bunch spacing configuration and simulated with a fast simulation using a parametrisation of the calorimeter response and GEANT4 for the other parts of the detector.

To simulate the effect of additional pp collisions in the same and nearby bunch crossings, additional interactions are generated using the soft QCD processes as provided by PYTHIA8.186 with the A2 tune [51] and the MSTW2008LO PDF set [52], and overlaid onto each simulated hard-scatter event. The MC samples are reweighted so that the pile-up distribution matches the one observed in the data. All MC samples are reconstructed in the same manner as the data.

4.6 Background samples

– **W/Z + jets:** Events containing W or Z bosons with associated jets (W/Z+jets) are simulated using the SHERPA2.2.1 generator with massive b/c-quarks. Matrix elements are calculated for up to two partons

Physics process	Generator	Parton shower	Cross-section normalisation	PDF set	Tune
SUSY Signals	MadGraph5_aMC@NLO 2.2.3 [24]	Pythia 8.186	NLO+NLL [25–29]	NNPDF2.3LO [30]	A14 [31]
W($\to \ell\nu$)+jets	Sherpa 2.2.1 [32]	Sherpa 2.2.1	NNLO [33]	NLO CT10	Sherpadefault
Z/$\gamma^*(\to \ell\ell)$+jets	Sherpa 2.2.1	Sherpa 2.2.1	NNLO	NLO CT10	Sherpadefault
$t\bar{t}$	Powheg-Box v2 [34]	Pythia 6.428 [35]	NNLO+NNLL [36–41]	NLO CT10	Perugia2012
Single-top (t-channel)	Powheg-Box v1	Pythia 6.428	NNLO+NNLL [42]	NLO CT10f4	Perugia2012
Single-top (s- and Wt- channels)	Powheg-Box v2	Pythia 6.428	NNLO+NNLL [43, 44]	NLO CT10	Perugia2012
$t\bar{t}W/Z/\gamma^*$	MadGraph5_aMC@NLO 2.2.2	Pythia 8.186	NLO [24]	NNPDF2.3LO	A14
Diboson	Sherpa 2.2.1	Sherpa 2.2.1	Generator NLO	CT10	Sherpadefault
$t\bar{t}h$	MadGraph5_aMC@NLO 2.2.2	Herwig 2.7.1 [45]	NLO [46]	CTEQ6L1	A14
Wh, Zh	MadGraph5_aMC@NLO 2.2.2	Pythia 8.186	NLO	NNPDF2.3LO	A14
$t\bar{t}WW$,$t\bar{t}t\bar{t}$	MadGraph5_aMC@NLO 2.2.2	Pythia 8.186	NLO	NNPDF2.3LO	A14
$tZ, tWZ, t\bar{t}t$	MadGraph5_aMC@NLO 2.2.2	Pythia 8.186	LO	NNPDF2.3LO	A14
Triboson	Sherpa 2.2.1	Sherpa 2.2.1	Generator LO,NLO	CT10	Sherpadefault

Table 4.1: Simulated signal and background event samples: the corresponding event generator, parton shower, cross-section normalisation, PDF set and underlying-event tune are shown.

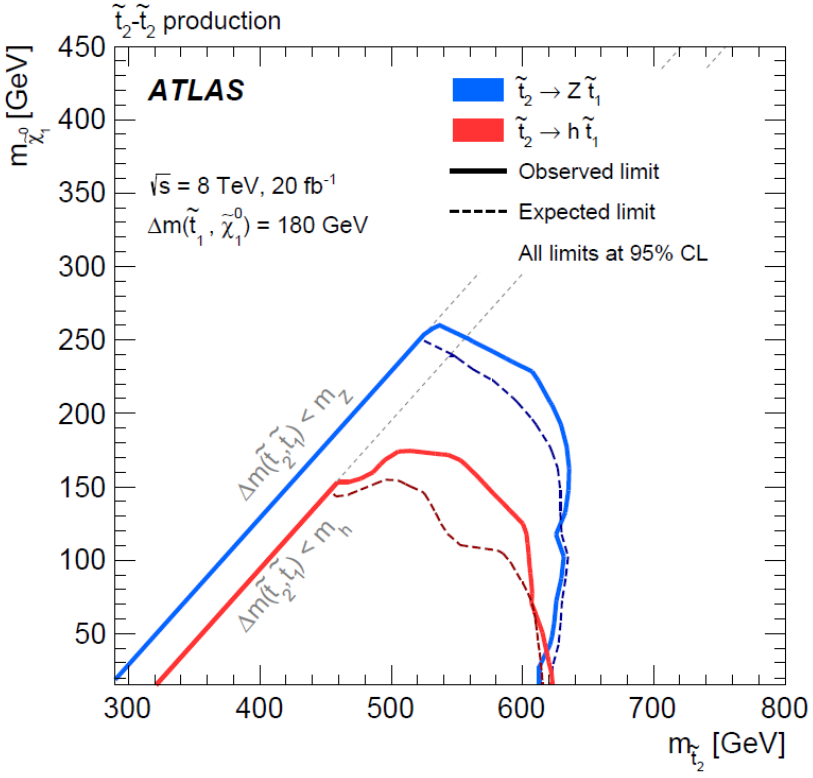

Figure 4.8: Exclusion limits at 95% CL in the scenario where $\widetilde{t}_2$ pair produciton is assumed, followed by the decay $\widetilde{t}_2 \to Z\widetilde{t}_1$ (blue) or $\widetilde{t}_2 \to h\widetilde{t}_1$ (red) and then by $\widetilde{t}_1 \to t\widetilde{\chi}_1^0$ with a branching ratio of 100%, as a function of the $\widetilde{t}_2$ and $\widetilde{\chi}_1^0$ masses. The $\widetilde{t}_1$ mass is determined by the relation m($\widetilde{t}_1$) - m($\widetilde{\chi}_1^0$) = 180 GeV. The dashed lines indicate the expected limit, the solid lines indicate the observed limit, and the dotted lines indicate the sensitivity to $\pm 1\sigma$ variations of the signal theoretical uncertainties.

at NLO and four partons at LO. The matrix elements are calculated using the Comix and OpenLoops generators and merged with the Sherpa 2.2.0 parton shower using the ME+PS@NLO prescription. The samples have been produced with a simplified scale setting prescription in the multi-parton matrix elements, to improve the event generation speed. The NNPDF3.0 NNLO PDF set is used in conjunction with a dedicated parton-shower tuning developed by the Sherpa authors. The W/Z+jets events are normalised to their NNLO cross-sections.
In all MC samples, except those produced by Sherpa, the EVTGEN v1.2.0 program is used to model the properties of the bottom and charm hadron decays.

– $t\bar{t}$**, single-top:** For the generation of $t\bar{t}$ and single top quarks in the Wt and s-channels, the POWHEG-BOX v2 generator with the CT10 PDF sets in the matrix-element calculations is used. Electroweak t-channel single-top-quark events are generated using the POWHEG-BOX v1 generator. This generator uses the four-flavour scheme for the NLO matrix-element calculations together with the fixed four-flavour PDF set CT10f4. For all

top-quark spin correlations are preserved (for the single-top t-channel, top quarks are decayed using MadSpin). The parton shower, fragmentation, and the underlying event are simulated using Pythia 6.428 with the CTEQ6L1 PDF set and the corresponding Perugia2012 tune. The top-quark mass is set to 172.5 GeV. The hdamp parameter, which controls the p_{T} of the first additional emission beyond the Born configuration, is set to the mass of the top-quark. The main effect of this is to regulate the high p_{T} emission against which the $t\bar{t}$ system recoils. The $t\bar{t}$ events are normalised to the NNLO+NNLL cross-sections. The single top quark events are normalised to the NLO+NNLL cross sections for the Wt-channel and to the NLO cross-sections for the t and s-channels.

– $t\bar{t}$ **processes:** Samples of $t\bar{t}+V$ (with $V = W,Z$, including non-resonant Z/γ^*) production are generated at NLO with MadGraph5_aMC@NLO 2.2.2 interfaced with Pythia8.186 parton shower model. Samples of $t\bar{t}+WW$ production are generated at LO with MadGraph5_aMC@NLO+Pythia 8 without additional partons included in the generation. The A14 tune was used together with the NNPDF23LO PDF set. The $t\bar{t}+W, t\bar{t}+Z, t\bar{t}+WW$ events are normalised to their NLO cross section.

– $t\bar{t}H$**:** Production of a Higgs boson in association with a $t\bar{t}$ pair is simulated at NLO using MadGraph5_aMC@NLO 2.2.2 interfaced with Herwig 2.7.1. The UEEE5 underlying event tune is used together with the CTEQ6L1 (matrix element) and CT10 (parton shower) PDF sets.

– $t\bar{t}H+V$**:**Simulated samples of SM Higgs boson production in association with a W or Z boson are produced with Pythia 8.186, using the A14 tune and the NNPDF23LO PDF set. Events are normalised with cross sections calculated at NLO.

– **Diboson:** Diboson processes with two to four charged leptons are simulated using the Sherpa v2.2.1 generator. The matrix elements contain the doubly-resonant WZ and ZZ processes and all other diagrams with four or six electroweak vertices (such as $WWjj$). The $3\ell + 1\nu$ and 4ℓ processes with up to one extra parton are calculated at NLO and additional diagrams involving up to three extra partons at LO using the Comix and OpenLoops matric element generators and merged with the Sherpa parton shower using the ME+PS@NLO presciption.

– **Triboson:** Fully leptonic triboson processes (WWW, WWZ, WZZ and ZZZ) with up to six charged leptons are also simulated using Sherpa v2.2.1. The $WWZ \to 4\ell{+}2\nu, WZZ \to 3\ell{+}3\nu$ or $5\ell{+}1\nu$, $ZZZ \to 6\ell{+}0\nu$ or $4\ell + 2\nu$ processes are calculated with the same configuration as the diboson samples, but with up to only two extra partons at LO. The CT10 parton distribution function (PDF) set is used for all Sherpa samples in conjunction with a dedicated parton shower tuning. The generator cross sections are used when normalising these backgrounds.

4.7 Event Reconstruction

The development of the ATLAS detector carried forward over the course of the last years (with additional progresses expected in the future) and presented in Chapters 1 and 2 is mainly addressed to achieve a continuous improvements to the reconstruction of the physics objects passing through the ATLAS detector. Particles created in the pp collisions (as well as those originating from the subsequent decay chains of the latter) are identified by the combination of the energy deposit signatures left on the various sub-detectors of ATLAS via off-line reconstruction algorithms that evolve together to the hardware of the experiment.
The definition of the objects used in the analysis is presented in this section, as reconstructed by the ATLAS offline software from inputs detected by the ATLAS subdetectors.

Tracks & **Vertices:**
The first level of particle reconstruction described here consists in the identification of the trajectories of charged particles referred to as tracks (*tracking*). The performance of the tracking widely improved between Run-I and Run-II as a result of the upgrade of the pixel detector system. The algorithm to reconstruct the tracks uses measurements taken by both the Inner Detector and the Muon Spectrometer; the collection of sensor measurements, or *hits*, from a single charged particle follows the path of the particle through space. Track reconstruction associates hits to individual particles and measures the trajectory by exploiting a three-dimensional fit to the position of the hits. Particles trajectories are parametrized with a five parameter vector

$$\tau = (d_0, z_0, \phi_0, \theta, \frac{q}{p}) \tag{4.17}$$

where d_0 is the transverse impact parameter defined as the distance of closest approach in the transverse plane of the track to the primary vertex; z_0 is the longitudinal impact parameter, ϕ_0 is the azimuthal angle of the track; θ is the polar angle and $\frac{q}{p}$ is the inverse of the particle momentum multiplied by its charge.
The reconstruction procedure is an iterative process that starts from the reading of *hits* in the PD or SCT detectors[53].

- *Clusterization:* charged-particle reconstruction begins by using charge deposit information to assemble clusters; this is made by grouping the pixels and strips in a given sensor where the deposited energy yields a charge above a threshold obtained by calibrations. From these clusters, three-dimensional measurements referred to as *space-points* are created, representing the point where the charged particle traversed the active material of the ID. In the pixel detector, each cluster equates to one space-point, while in the SCT, clusters from both sides of a strip layer must be combined to obtain a three-dimensional measurement.

- *Iterative combinatorial track finding:* using a set of three space-points obtained by clusterization, *Track seeds* are formed. The impact parameters of a track seed, with respect to the centre of the interaction region,

are estimated by assuming a perfect helical trajectory in a uniform magnetic field. *Track candidates* are then built by using a combinatorial Kalman filter from the chosen seeds by incorporating additional space-points from the remaining layers of the pixel and SCT detectors which are compatible with the preliminary trajectory. This filtering procedure creates multiple track candidates per seed if more than one compatible space-point extension if found on the same ID layer.

- *Ambiguity solving of track candidates:* at each track candidate a track score is assigned, reflecting various consideration regarding the track quality. Clusters assigned to a track increase the track score according to configurable weight fractions reflecting the intrinsic resolutions and expected cluster multiplicities in the different sub-detectors. Track candidates considered to create the reconstructed tracks collection are processed individually in descending order of a track score, favouring tracks with a higher score.

- *Neural-network pixel clustering:* Clusters created by charge deposits from multiple particles are called *merged* clusters. In order to minimize the loss of efficiency due to limitations on the number of shared clusters per track, an artificial neural network (NN) trained to identify merged clusters is used to aid the Ambiguity Solver. The measured charge, which is proportional to the deposited energy, and relative position of pixels in the cluster can be used to identify merged clusters. Additional information about the particle's incident angle, provided from the track candidate, significantly improves the NN's performance

Track candidates are rejected by the ambiguity solver if they fail to meet any of the following basic quality criteria:

- $p_{\mathrm{T}} > 400$ MeV
- $|\eta| < 2.5$
- Minimum of 7 pixel and SCT clusters (12 are expected)
- No more than two holes in the combined pixel and SCT detectors.
- No more than one hole in the pixel detector
- $|d_0^{BL}| < 2.0$ mm
- $|z_0^{BL} \sin\theta| < 3.0$ mm

where d_0^{BL} is the transverse impact parameter calculated with respect to the measured beam-line position, z_0^{BL} is the longitudinal difference along the beam-line between the point where d_0^{BL} is measured and the primary vertex and θ is the polar angle of the track.
Two types of vertex can be distinguished in an ATLAS event:

- *Primary Vertex (PV):* this vertex is characterized by a high particle multiplicity. Vertices due to pile-up interactions may cause the PV reconstruction efficiency to decrease, both for the merging (when the nearby interaction prevents the reconstruction of the vertex) and for the closeness of two vertices that cannot be resolved.

- *Secondary vertex (SV):* vertex corresponding to the decay of short-lived particles, such as $b-$hadrons. These vertices are usually characterized by a lower track multiplicity with respect to PV.

Jets:
collimated sprays of hadrons, also know as jets, are the dominant physics objects arising in proton-proton collisions at the LHC [62]. The correct reconstruction of jets is essential in the presented search, as an high jet multiplicity due to heavy hadronic activity is expected in the final state. The precision of the jet energy measurement directly affects the performance of the missing transverse energy reconstruction.
The algorithms for the jet reconstruction and the *jet energy scale (JES)* calibration, were developed and validated in ATLAS during the LHC Run-1. The proton-proton collisions at the centre-of-mass energy of $\sqrt{s} = 13$ TeV at the LHC Run-2 force the evolution of these algorithms in presence of multi-TeV final states towards the highest precision.
Possible inputs of the reconstruction algorithm are calorimeter energy deposits, inner detector tracks or a combination of both.

b-tagging:
as the Higgs boson in the decay chain of the $\widetilde{t}_2$ is expected to decay in two b-quarks, the identification of jets containing b-hadrons (*b-tagging*) is an essential ingredient in this BSM search. The inputs to the $b-$tagging algorithms are the trajectories of charged particles (tracks) reconstructed in the ID[54] as well as reconstructed jets.
The identification of $b-$quark jets in ATLAS is based on distinct strategies encoded in three basic $b-$tagging algorithms, respectively *IP2/3D*, *SV* and *JetFitter*. The outputs of these $b-$tagging algorithms are combined and fed to a multivariate discriminant ($MV2$) algorithm [55].

  - *IP2D and IP3D:* are impact parameter-based algorithms. The long lifetime of hadrons containing a $b-$quark ($\sim$1.5 ps) can be exploited to build lifetime-based tagging algorithms. This long lifetime permits to separate the contribution of tracks generated from $b-$hadron decay products from that of tracks from the *primary vertex*, due to the large impact parameters of the former. Given that the decay point of the $b-$hadron must lie along its flight path, the transverse impact parameter is signed to further discriminate the tracks from $b-$hadron decay from tracks originating from the primary vertex. The sign is defined as positive if the track intersects the jet axis in front of the primary vertex, and as negative if the intersection lies behind the primary vertex. The background events generates a random sign for the tracks originating from the pri-

mary vertex, while tracks from the $b-/c-$hadron decay normally have a positive sign.

The track selection applied for the impact-parameter algorithm is based on the requirements of a track p_{T} above 1 GeV, $|d_0| < 1$ mm and $|z_0 \sin\theta|$ < 1.5 mm and seven or more silicon hits, with at most two silicon holes, at most one of which is in the pixel detector, where a *hole* is defined as a hit expected to be associated with the track but not present.

- *Secondary Vertex finding algorithm:* The secondary vertex finding algorithm reconstructs an inclusive displaced secondary vertex within the jet. All track pairs within a jet are paired and tested for a two-track vertex hypothesis; any found two track vertices are rejected if it is established they were likely to originate from the decay of a long-lived particle, such as a K_s or a Λ, photon conversions or hadronic interactions with the detector material. If a two-track vertex is not rejected, a new vertex is then fitted with all tracks from the accepted two-track vertices. Each selected track is required to have at least seven silicon hits (sum of pixel and SCT hits) and at most one shared hit in these two detectors.

- *JetFitter:* is a decay chain multi-vertex reconstruction algorithm. It exploits the topological structure of weak $b-$ and $c-$hadron decays inside the jet and tries to reconstruct the full $b-$hadron decay chain. A Kalman filter is used to find a common line on which the primary vertex and the bottom and charm vertices lie, approximating the $b-$hadron flight path, as well as their positions. With this approach, the $b-$ and $c-$hadron vertices, whenever resolution allows, can be resolved, even when only a single track is attached to any of them.

- *Multivariate Algorithm MV2:* To achieve a better discrimination than any of the basic algorithms can exploit individually, a *Boosted Decisions Tree (BDT)* algorithm is employed. It combines the output of the previous taggers. The BDT of the multivariate classifier is trained, in the frame of this search, on jets from $t\bar{t}$events with b-jets being considered as signal, and c- and *light*-flavour jets being considered as background.

The total fraction of b-jets correctly identified by the b-tagging algorithms is called $b-tagging\ efficiency$. In order to limit the acceptance of mistagged jets as b-jets, the b-tagging efficiency is limited to a point in which the mistagged jets constitutes minor contributions to the total. A fixed working point for b-tagging efficiency of 70% is taken in order to limit this contributions, increasing light-[1] and c-jets rejection[2]. The IBL is of extreme importance for b-tagging, since, being close to the interaction point of the beams, it provides a significantly better reconstruction of the track-impact-parameters, leading to an improvement of a factor of 4 (Fig. 4.9) in the rejection of light jets at a b-tagging efficiency of 77%, which is now taken as a working point.

[1]light-jet rejection is defined as $\frac{1}{\epsilon_b^l}$, where ϵ_b^l is the efficiency for a light jet to be tagged as b-jet.

[2]light-jet rejection is defined as $\frac{1}{\epsilon_b^c}$, where ϵ_b^c is the efficiency for a c-jet to be tagged as b-jet.

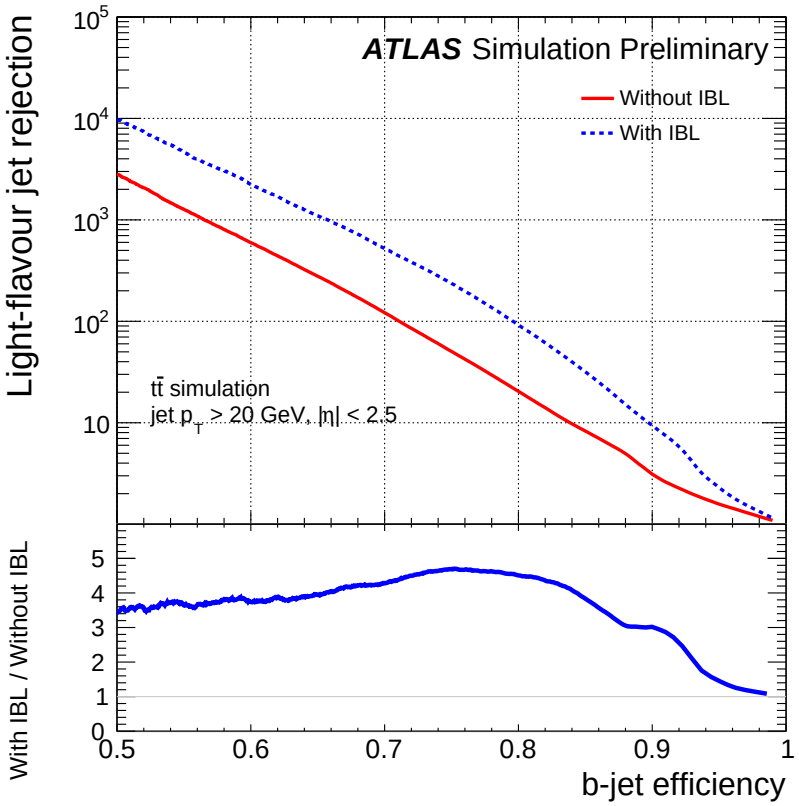

Figure 4.9: Performance of the b-tagging algorithm MV2c20 expressed in terms of light-jet rejection as a function of b-tagging efficiency. The algorithm is applied to jets from top pair events. The performance of the Run-1 ("Without IBL"") and Run-2 (""With IBL") detector layouts are compared, where the latter includes IBL. The underlying algorithms are updated to the detector geometry in each case. Jets are required to be truth matched to a hard scatter jet. The rejection is defined as the inverse of the tagging efficiency.

Electrons:
Electrons passing through the ATLAS detector (also comprising positrons) in the central preudorapidity region $|\eta| < 2.47$ give rise to tracks in the ID and energy deposits in the electromagnetic calorimeter. The calorimeter signals are used in the first level trigger system (L1) and combined with tracks to reconstruct electron candidates used for the high level trigger (HLT) decision algorithms[56].
The electron candidates are then further selected against background, such as hadrons and non-prompt or other background electrons originating predominantly from photon conversions and heavy flavour hadron decays. This is achieved by using multiple sets of identification criteria with different levels of background rejection and signal efficiency. These identification criteria rely on the shapes of electromagnetic showers in the calorimeter as well as on variables related to the match to tracks and track-to-cluster. Additionally, electrons can be required to be isolated from other activity in the calorimeter or inner detector to further distinguish them from background objects. Electron reconstruction in the central region of the ATLAS detector proceed in

several steps:

- *Seed-cluster reconstruction:* electron cluster "seeds" are composed in the EM calorimenter by sliding a sampling window with a size of 3×5 in units of 0.025×0.025, corresponding to the granularity of the middle layer of the detector, in $\eta \times \phi$ space. The sliding window creates clusters with total transverse energy above 2.5 GeV. The clusters are then formed around the seeds using a clustering algorithm that allows for duplicates to be removed.

- *Track reconstruction:* the following step is based on a re-interpretation of a track seed (consisting of three hits in different layers of the silicon detectors) with a transverse momentum larger than 1 GeV. If the latter cannot be successfully extended to a full track and it falls within one of the EM cluster region of interest, a second attempt is performed with the new pattern recognition using an electron hypothesis that allows for larger energy loss.

- *Electron specific track fit:* in case a track seed is re-interpreted as an electron, the obtained tracks are loosely matched to EM clusters using the distance in η and ϕ between the position of the track, after extrapolation, in the calorimeter middle layer and the cluster barycentre. The matching conditions account for energy-loss due to bremsstrahlung and the number of precision hits in the silicon detector.

- *Electron candidate reconstruction:* the reconstruction of the electron is completed when there's a matching of the track candidate to the cluster seed. A similar matching as the one described above is repeated for the refit track with stricter conditions. If several tracks fulfil the matching condition, one track is chosen as "primary" track. The choice is based on an algorithm using the cluster-track distance R calculated using different momentum hypotheses, the number of pixel hits and the presence of a hit in the first silicon layer. Electron candidates without any associated precision hit tracks are removed and considered to be photons.

- *Electron identification:* in order to determine whether the reconstructed electron candidates are signal-like objects (electrons) or background-like objects (hadronic jets or converted photons), algorithms for electron identification (ID) are applied. Five levels of identification operating points are typically provided for electron ID. These are referred to, in order of increasing background rejection, as `VeryLooseLH, LooseLH, LooseAndBlayerLH, MediumLH, TightLH`. In the specific frame of this analysis, the operating points will refer to the `LH`(likelihood-based) identification algorithm. The five operating points are defined such that the samples selected by them are subsets of one another. Thus, electrons selected by `MediumLH` are all selected by `LooseLH`, and `TightLH` electrons are all selected by `MediumLH`.

- *Electron Isolation:* in addition to the identification criteria described above, electrons are required to fulfil isolation requirements, to further

discriminate between signal and background. The isolation variables quantify the energy of the particles produced around the electron candidate and allow to disentangle prompt electrons (from heavy resonance decays, such as $W \rightarrow e\nu$, $Z \rightarrow ee$) from other, non-isolated electron candidates such as electrons originating from converted photons produced in hadron decays, electrons from heavy flavour hadron decays, and light hadrons misidentified as electrons.

Muons:
Muons are reconstructed by hits on the Inner Detector and tracks in the Muon Spectrometer [57] and are selected for analysis using a set of requirements developed to reject delayed muons coming from pion and kaon decays and to guarantee a reliable momentum measurement. Four muon selections are currently maintained for use in physics analyses: `Loose`, `Medium`, `Tight`, and `High-`p_{T}. The `Loose` identification criteria are designed to maximize muon reconstruction efficiency and are specifically optimized for reconstructing Higgs boson candidates in the four-lepton final state. The `Medium` criteria, representing the default selection for muons in ATLAS, is designed to minimize systematic uncertainties associated with muon reconstruction and calibration. The `Tight` criteria minimize the fake muon rate to optimize sample purity and finally, the `High-`p_{T} selection aims to maximize momentum resolution for tracks with transverse momentum above 100 GeV.

Missing transverse momentum:
Missing transverse momentum and its magnitude, the missing transverse energy E_{T}^{miss}, is a measure of the transverse momentum imbalance created by detected and well measured objects in an event. Invisible particles, such as neutrinos and neutralinos, can be reconstructed from the vector form of the E_{T}^{miss}, meaning that a good performance of missing transverse energy reconstruction is crucial for many SUSY (as well as dark matter) searches.
The missing transverse momentum vector ($\vec{E_{\mathrm{T}}^{miss}}$) is reconstructed as the negative vector sum of transverse momenta (p_{T}^{miss}) of reconstructed physics objects. The magnitude of the missing transverse energy is denoted by E_{T}^{miss} and is defined as:

$$E_{\mathrm{T}}^{miss} = \sqrt{(E_x^{miss})^2 + (E_y^{miss})^2} \tag{4.18}$$

where $E_x^{miss} = -\Sigma E_x$ and $E_y^{miss} = -\Sigma E_y$. The physics objects considered in the E_{T}^{miss} calculation are electrons, photons, muons, τ-leptons and the hard terms of jets. The reconstructed momentum not associated to any of the hard terms is referred as the *soft term* and is also considered in the E_{T}^{miss} calculation as a separate term.
Several algorithms can be used to reconstruct the E_{T}^{miss} soft term using calorimeter energy deposits or tracks. The main algorithm for the soft term reconstruction used by ATLAS during Run-II fully relies on tracks, reconstructing the so-called *Track Soft Term (TST)* [63].

Chapter 5

Search for direct $\widetilde{t}_2$ pair production in events with a Higgs boson

This chapter presents the search strategy for direct pair production of $\widetilde{t}_2$ and its subsequent decay in a $\widetilde{t}_1$ plus a Higgs boson in the decay chain. An overview of the kinematic variables acting as discriminants between the SUSY signal and the SM background is presented, as well as the requirements that the events detected by the ATLAS detector must satisfy to be considered candidates for this study.
Being the kinematic of the produced Higgs boson a powerful discriminating tool, extensive studies addressing its reconstruction have been performed and led to results that sensibly increase the significance of the signal over the background. In order to maximize the latter, the phase space accessible by this decay for the models we are taking into account has been divided in three event selections, called *Signal Regions* (SR), on each of which a different search strategy has been set up and implemented.
Furthermore, it is essential to have the full control over the modelling of the SM background; the MC simulation of our main background ($t\bar{t}$) has been then studied in a separate kinematic region and normalized to the observed data yields.
Finally, the main systematic uncertainties affecting this search, due to both experimental and theoretical inefficiencies, have been estimated and presented.

5.1 Event selection

Candidate events are required to have a reconstructed vertex with at least two associated tracks with $p_{\mathrm{T}} > 400$ MeV which are consistent with originating from the beam collision region in the $x-y$ plane. The vertex with the highest scalar sum of the squared transverse momentum of the associated tracks is considered to be the primary vertex of the event.

Leptons: Two categories of leptons (electrons and muons) are defined: *"candidate"*and *"signal"* (the latter being a subset of the *"candidate"* leptons satisfying tighter selection criteria). Electron candidates are reconstructed from isolated electromagnetic calorimeter energy deposit matched to ID tracks and are required to have $|\eta|< 2.47$, a transverse momentum $p_{\mathrm{T}} > 10$ GeV, and

Object	Selection
Jets	$p_{\mathrm{T}} > 30$ GeV $\lvert\eta\rvert < 2.5$ `Medium JVT` if $p_{\mathrm{T}} < 60$ GeV and $\lvert\eta\rvert < 2.4$
Candidate Electrons	$\frac{E^{clust}}{cosh(\eta)} > 10$ GeV $\lvert\eta\rvert < 2.47$ (if no. silicon hits > 4, $\eta = \eta^{track}$ else $\eta = \eta^{clust}$) `LooseLH`
Signal Electrons	$\frac{E^{clust}}{cosh(\eta)} > 20$ GeV `MediumLH` `FixedCutTight` isolation
Candidate Muons	$p_{\mathrm{T}} > 10$ GeV $\lvert\eta\rvert < 2.4$
Signal Muons	$p_{\mathrm{T}} > 20$ GeV `MediumLH` `FixedCutTightTrackOnly` isolation

Table 5.1: Summary of jet, electron (candidate and signal) and muon (candidate and signal) selection criteria for the $\widetilde{t}_2$ search.

to pass a `LooseLH` likelihood-based identification requirement. The likelihood input variables include measurements of shower shapes in the calorimeter and track properties in the ID.
In MonteCarlo generated samples a multiplicative event weight is applied for each selected electron to the overall event weight in order to correct for differences in reconstruction, identification and isolation efficiency between data and MC.

Muons: Muon candidates are reconstructed in the region $|\eta|< 2.5$ from muon spectrometer tracks matching ID tracks. Candidate muons must have $p_{\mathrm{T}} > 10$ GeV and pass the `MediumLH` identification requirements, based on the number of hits in the different ID and muon spectrometer subsystems, and on the significance of the charge to momentum ratio q/p.
In order to correct for differences in efficiency between Data and MC a smearing procedure is applied to the muon p_{T} and multiplicative event weight is applied for each selected muon in MC.

Jets: Jets are reconstructed from three dimensional energy clusters in the calorimeter using the anti-k_t jet clustering algorithm [59] with a radius parameter R = 0.4. Only jet candidates with $p_{\mathrm{T}} > 30$ GeV and $|\eta|< 2.5$ are considered as selected jets in the analysis. Jets are calibrated as described in Sec. 4.7 and the expected average energy contribution from pile-up clusters is subtracted according to the jet area. In order to reduce the effects of pile-up, for jets with $p_{\mathrm{T}} < 60$ GeV and $|\eta|< 2.4$ a significant fraction of the tracks associated with each jet must have an origin compatible with the primary vertex, as defined by the JVT [60].

In order to remove events with fake E_{T}^{miss}, an event is vetoed when jet not satisfying the `VeryLoose`[61] condition is present within $|\eta| < 4.9$.
Events are discarded if they contain any jet with $p_{\mathrm{T}} > 20$ GeV not satisfying basic quality selection criteria designed to reject detector noise and non-collision backgrounds.

b-jets: Identification of jets containing b-hadrons is performed with the `MV2c10` tagging algorithm, indicating a version of the MV2 (as presented in Section 4.7) algorithm whose training has been performed with a sample with a $c-$jet fraction of 10%.
A requirement is chosen corresponding to a 77% average efficiency obtained for b-quark gets in simulated $t\bar{t}$ events. The rejection factors for light-quark and gluon jets, c-quark jets and $\tau \rightarrow hadrons + \nu$ decays in simulated $t\bar{t}$ events are approximately 380, 12 and 54, respectively. To compensate for differences between data and MC simulation in the b-tagging efficiencies and mis-tag rates, correction factors are applied to the simulated samples.
The bulk of the b-jets entering the SR and CR for this analysis lie in the region $50 < p_{\mathrm{T}} < 250$ GeV.

E_{T}^{miss} : The magnitude of the missing transverse momentum vector is defined as the negative vector sum of the transverse momenta of all identified electrons, photons, muons and jets, and an additional soft term. The soft term is constructed from all tracks originating from the primary vertex which are not associated with any identified particle or jet. In this way, the E_{T}^{miss} is adjusted for the best calibration of particles and jets listed above, while maintaining pile-up independence in the soft-term.

Tighter requirements on the lepton candidates are imposed, which are then referred to as *"signal"* electrons or muons. Signal electrons must satisfy the `MediumLH` likelihood-based identification requirement. Signal leptons must have $p_{\mathrm{T}} > 20$ GeV. The associated tracks must have a significance of the transverse impact parameter with respect to the reconstructed primary vertex, d_0, of $|d_0|/\sigma(d_0)| < 5$ for electrons and $|d_0|/\sigma(d_0)| < 3$ for muons, and a longitudinal impact parameter with respect to the reconstructed primary vertex, z_0, satisfying $|z_0 \sin(\theta)| < 0.5$ mm. Isolation requirements are applied to both the signal electrons and muons.

The scalar sum of the p_{T} of tracks within a variable-size cone around the lepton, excluding its own track, must be less than 6% of the lepton p_{T}. The size of the track isolation cone for electrons (muons) is given by the smaller of $\Delta R = 10\ GeV/p_{\mathrm{T}}$ and $\Delta R = 0.2(0.3)$, that is, a cone of size 0.2 (0.3) at low p_{T} but narrower for high-p_{T} leptons. In addition, in the case of electrons the energy of calorimeter energy clusters in a cone of $\Delta R_\eta = \sqrt{(\Delta\eta)^2 + (\Delta\phi)^2} = 0.2$ around the electron (excluding the deposition from the electron itself) must be less than 6% of the electron p_{T}.
Simulated events are corrected to account for minor differences in the signal lepton trigger, reconstruction, identification and isolation efficiencies between data and MC simulation.

Overlap Removal : The overlap removal (OR) is performed with candidate, non-isolated electrons, muons and jets with $p_{\mathrm{T}} > 20$ GeV, as presented in Tab.5.1. We rely on a standardized implementation of the OR, following ATLAS-level harmonization efforts, including the usage of a shrinking cone for jet-muon overlap removal. The removal of pile-up jets is essential for E_{T}^{miss} resolution. This is done with the JVT technique which extracts the pile-up jets using track-to-vertex association method.
The OR procedure can roughly be described as:

- Jets within $\Delta R = \sqrt{(\Delta y)^2 + (\Delta\phi)^2} = 0.2$ of a lepton are discarded as they mostly originate from calorimeter deposits from electron shower or muon bremsstrahlung (where only jets with few associated tracks and modest p_{T} relatively to the muon may be discarded).

- If a jet is b-tagged, it is kept and the lepton discarded since it likely comes from a semi-leptonic b-quark decay.

- Subsequently, electrons and muons within $\Delta R = 0.4$ (for electrons) or $\Delta R = \min(0..4, 0.04 + p_{\mathrm{T}}(\mu)/10 \text{ GeV})$ (for muons) of the remaining jets are discarded, to reject non-prompt or fake leptons originating from hadron decays.

- Any muons tagged in the calorimeter sharing an ID track with an electron are removed. Any electrons sharing an IS track with remaining muons are removed.

Preselection:

The events are classified in a further step by requiring at least four b-tagged jets and one or two leptons, aiming at the decay of the Higgs boson in a $b\bar{b}$ pair and the decay of the top quark in a b quark for each of the two $\widetilde{t}_2$ produced in the direct pair production. In addition, events are required to pass a trigger requiring an isolated lepton or muon. The trigger-level requirements on the p_{T}, identification and isolation of the leptons involved in the trigger decision are looser than those applied off-line to ensure that trigger efficiencies are constant in the relevant phase space.
Additional requirements are applied depending on the final state, as described in the following. These requirements are optimised for the best discovery significance using the simplified models featuring $\widetilde{t}_2$ production with the $\widetilde{t}_2 \to h\widetilde{t}_1$ decay.

5.2 Higgs boson reconstruction methods

The 67 mass models $(m_{\widetilde{t}_2}, m_{\widetilde{t}_1}, m_{\widetilde{\chi}_1^0})$ on which the search as been performed cover a wide phase space and therefore an extensive phenomenology. Being the mass difference between $\widetilde{t}_1$ and $\widetilde{\chi}_1^0$ fixed in our models, as the search is performed in the compressed region $m_{\widetilde{t}_1} - m_{\widetilde{\chi}_1^0} \simeq m_t = 180$ GeV, the two only defining variables of the kinematic of the decay chain (for each mass model)

are the massed of the $\widetilde{t}_2$ and $\widetilde{\chi}_1^0$.
In the two-body decay $\widetilde{t}_2 \to \widetilde{t}_1 + h$ this translates in a different kinematic of the Higgs boson. The correct reconstruction of this scalar (or rather, of the two b-quarks originating from its decay) is therefore of primary importance and four different reconstruction methods have been tested. The impact of each one of which has been tested during the optimisation of the signal-to-background significance.

Highest p_{T} reconstruction

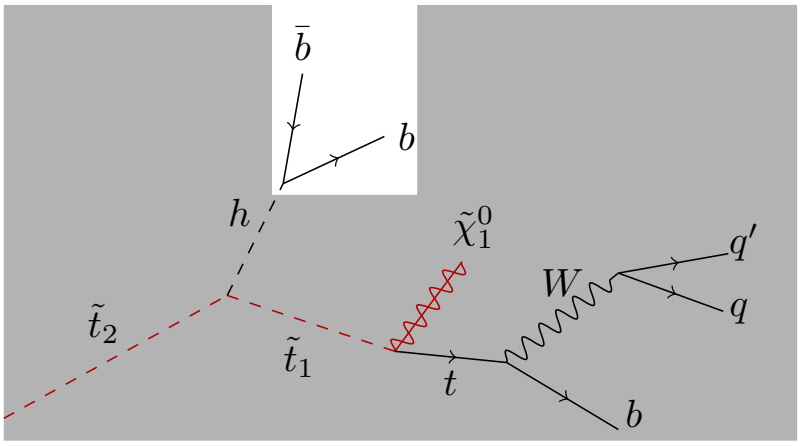

Figure 5.1: Diagram of the Higgs boson top candidate reconstruction method. b-jets from the Higgs decay are identified by taking the two b-tagged jets with highest combined transverse momentum $p_{\mathrm{T}}^{bjet1\ +\ bjet2}$.

At least 2 b-tagged jets are required, with $p_{\mathrm{T}} \geq 30$ GeV and $|\eta| \leq 2.5$. B-jets from the Higgs decay are identified by taking the two b-tagged jets with highest combined transverse momentum $p_{\mathrm{T}}^{bjet1\ +\ bjet2}$. This reconstruction method is expected to be efficient in high-boosted scenarios, where the mass splitting between $\widetilde{t}_2$ and $\widetilde{t}_1$ is large enough to produce high-p_{T} Higgs bosons.

χ^2 minimization

Based on the reconstruction of multiple decay products (top quark, W boson, Higgs boson). At least 2 light jets and 3 b-tagged jets are required. Both the light jets and the b-tagged jets must have $p_{\mathrm{T}} \geq 30$ GeV and $|\eta| \leq 2.5$.
By looping over the available light jets in an event, a W candidate is reconstructed by taking the pair of lught jets J_1, J_2 with the smallest ΔR between them. The W candidate must have a mass $M_{J_1+J_2}$ satisfying

$$|M_{J_1+J_2} \ - \ M_W| \ < \ 30\ GeV \tag{5.1}$$

where M_W is the mass of the W boson.
For every W boson candidate W^{cand}, a set of top candidates t_i^{cand} are reconstructed by looping over the available b-tagged jets b_i.

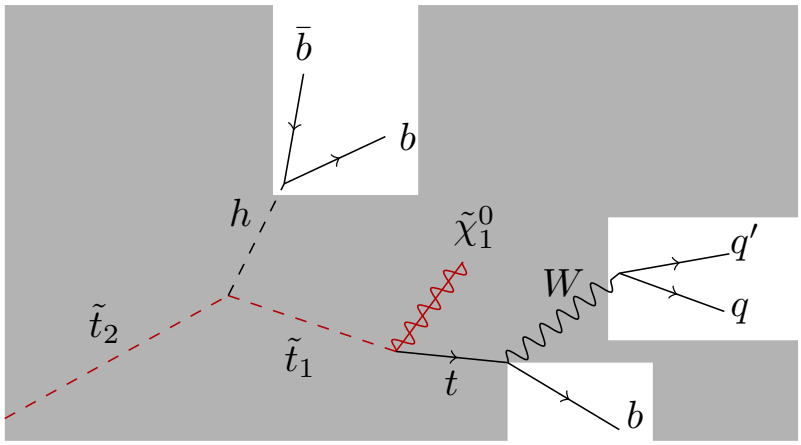

Figure 5.2: Diagram of the Higgs boson χ^2 minimization reconstruction method. The subsequent reconstruction of a W boson candidate, a t quark candidate and an h boson candidate is tested through a χ^2 minimization of each of the reconstructed h and t candidates.

Using the remaining b-tagged jets, a set of Higgs boson candidates H_i^{cand} is reconstructed by taking the two remaining b-tagged jets b_i with the combined invariant mass closer to the Higgs boson mass $M_H = 125$ GeV.
The set of reconstructed top quarks candidates t_i^{cand} and Higgs boson candidates H_i^{cand} are used to calculate a set of χ_i^2 values

$$\chi_i^2 = \frac{(m_{t_i^{cand}} - m_t)^2}{10\% m_t} + \frac{(m_{H_i^{cand}} - m_H)^2}{10\% m_H} \tag{5.2}$$

The Higgs boson candidate with the smallest χ^2 value is used as reconstructed Higgs boson.

Top candidate reconstruction

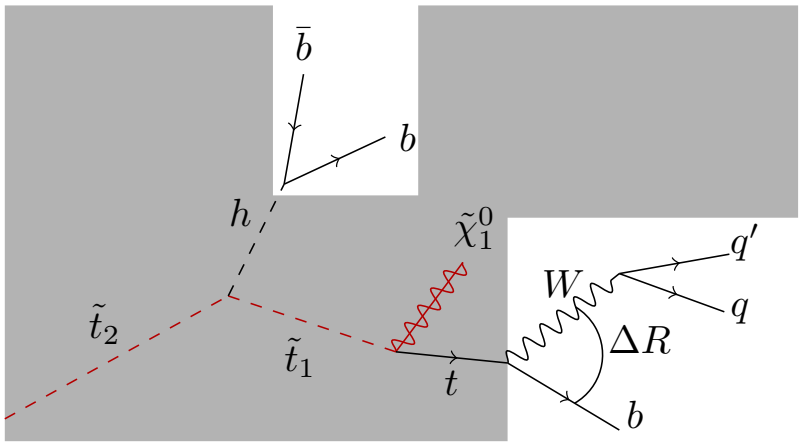

Figure 5.3: Diagram of the Higgs boson top candidate reconstruction method. From the subsequent reconstruction of a W boson candidate and a t quark candidate, a H boson candidate is reconstructed by taking the $b\bar{b}$ pair with the combined invariant mass closer to 125 GeV.

Based on the reconstruction of multiple decay products (top quark, W boson, Higgs boson). At least 2 light jets and 3 b-tagged jets are required. Both the light jets and the b-tagged jets must have $p_{\mathrm{T}} \geq 30$ GeV and $|\eta| \leq 2.5$.
By looping over the available light jets in an event, a W candidate is reconstructed by taking the pair of light jets J_1, J_2 with the smallest ΔR between them. The W candidate must have a mass $M_{J_1+J_2}$ satisfying Eq.5.1. For every W boson candidate W^{cand}, a top candidate t^{cand} is reconstructed by taking the b-tagged jet with smallest ΔR with respect to W^{cand}
Using the remaining b-tagged jets, a Higgs boson candidate H^{cand} is reconstructed by looping over the b_i and taking the pair with the combined invariant mass closer to the Higgs boson mass M_H.

Minimum ΔR reconstruction

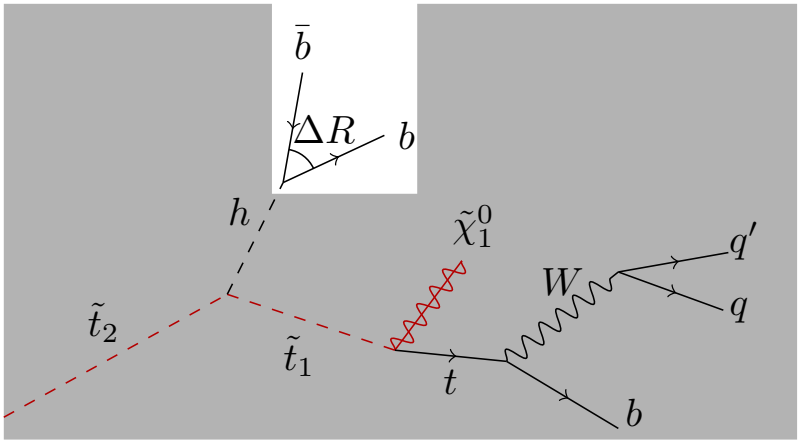

Figure 5.4: Diagram of the Higgs boson top candidate reconstruction method. b-jets from the Higgs decay are identified by taking the two more collimated b-tagged jets.

At least 2 b-tagged jets are required, with $p_{\mathrm{T}} \geq 30$ GeV and $|\eta| \leq 2.5$. b-jets from the Higgs decay are identified by taking the two more collimated b-tagged jets. As the method presented above, this reconstruction method is expected to be efficient in high-boosted scenarios, where the mass splitting between $\widetilde{t}_2$ and $\widetilde{t}_1$ is big enough to create high-p_{T} Higgs bosons and therefore collimated $b-$jets.
This reconstruction method proved to be the best one to increase the sensitivity in boosted scenarios and has therefore been used as a standard reconstruction method for Higgs boson candidates.
From now on, every Higgs boson-related variable is implied to have been reconstructed with this method.

5.3 Signal regions definition

The mass splitting between $\widetilde{t}_2$ and $\widetilde{\chi}_1^0$ give rise to different kinematics of the decay, as the Higgs boson from the $\widetilde{t}_2$ decay will pass from a rest production (in the $\widetilde{t}_2$ rest frame) to a boosted scenario.
To maximize the sensitivity in different regions of the mass parameter space, three overlapping signal regions (SR) are defined, exploiting the different distributions of various kinematic discriminants.
$SR_A^{1\ell 4b}$ is focused on covering the high-p_{T} region, where the mass splitting between $\widetilde{t}_2$ and $\widetilde{t}_1$ is large and the objects in the decay chain are boosted; $SR_B^{1\ell 4b}$ targets the intermediate mass splitting region; $SR_C^{1\ell 4b}$ targets the low-p_{T} mass splitting region, where the decay products are produced (almost) at rest in the $\widetilde{t}_2$ rest frame.

Different discriminators and kinematic variables are used in the analyses to separate the SUSY signal from the SM background.

- m_{bb}: the invariant mass of the b-jet pair forming the Higgs boson candidate. Multiple techniques have been considered to identify the Higgs boson candidate as presented in Sec.5.2.

- p_{T}^{bb}: the transverse momentum of the b-jet pair forming the Higgs boson candidate. This variable is helpful in rejecting the SM backgrounds that don't include boosted Higgs boson.

- H_T: the scalar sum of the p_{T} of all the jets above 30 GeV. This variable is sensitive to the large expected hadronic activity for the signal.

$$H_T \equiv \sum p_{\mathrm{T}} \ , \ for\ jet\ p_{\mathrm{T}} \ > \ 30\ GeV \tag{5.3}$$

As the analysis strategy is based on the definition of discriminating variables in order to maximize the significance of the expected signal over the SM background. The discovery significance z_N is computed as:

$$z_N = \texttt{binomialExpZ}(S, B, \delta B) \tag{5.4}$$

where S is the signal rate, B the total background predicted by the simulations, δB the systematic uncertainty on the background and `binomialExpZ` is defined in [68].
Optimization was performed on three different signal models, each representing a portion of $m_{\widetilde{t}_2}, m_{\widetilde{\chi}_1^0}$ phase space and targeting a different kinematic of the Higgs boson in the decay chain, by simultaneously scanning all the kinematic discriminants and finding the combination of requirements that maximizes z_N.
For each Signal Region, the expected distribution for all SM backgrounds are shown in Fig.5.5 (for $SR_A^{1\ell 4b}$), Fig.5.6 (for $SR_B^{1\ell 4b}$) and Fig.5.8 (for $SR_C^{1\ell 4b}$), with the simulated processes normalised to their theoretical cross sections for an integrated luminosity of 36.5 fb^{-1}. The bottom pad shows the expected z_N as a function of the selection on the plotted variable, assuming a flat 30% systematic uncertainty on the background yield. A full description of the statistical significance of this search method is given in Appendix B.

- **Signal region** $SR_A^{1\ell 4b}$ is optimised for large $\widetilde{t}_2 - \widetilde{\chi}_1^0$ mass splitting, where the Higgs boson in the $\widetilde{t}_2 \to \widetilde{t}_1 h$ decay is boosted. In this signal region, the pair of b-tagged jets with the smallest ΔR^{bb} is required to have an invariant mass consistent with the Higgs boson mass ($|m_{bb} - m_h| < 15$ GeV, with $m_h = 125$ GeV), and the transverse momentum of the system formed by these two b-tagged jets (p_{T}^{bb}) is required to be above 300 GeV. It also include requirements on H_T, due to the high expected hadronic activity. The optimization of the boosted signal region, $SR_A^{1\ell 4b}$, is based on the study of the signal model with $m_{\widetilde{t}_2} = 800$ GeV, $m_{\widetilde{t}_1} = 180$ GeV, $m_{\widetilde{\chi}_1^0} = 0$ GeV, shown as dashed line in (Fig.5.5).

- **Signal region** $SR_B^{1\ell 4b}$ covers the intermediate mass splitting case, featuring slightly harder kinematic requirements than $SR_A^{1\ell 4b}$. It includes a requirement on the lepton transverse mass m_T, defined as:

$$m_T = \sqrt{2 p_{\mathrm{T}}^{\ell} E_{\mathrm{T}}^{miss} (1 - \cos[\Delta\phi(\ell, E_{\mathrm{T}}^{miss})])} \tag{5.5}$$

  and computed using the missing-momentum and lepton-momentum vectors. The optimization of the intermediate signal region, $SR_B^{1\ell 4b}$, is based on the study of the signal model with $m_{\widetilde{t}_2} = 750$ GeV, $m_{\widetilde{t}_1} = 230$ GeV, $m_{\widetilde{\chi}_1^0} = 50$ GeV, shown as dashed line in (Fig.5.6).

- **Signal region** $SR_C^{1\ell 4b}$ is designed to be sensisitve to the compressed spectrum $m_{\widetilde{t}_2} \gtrsim m_{\widetilde{\chi}_1^0} + m_t + m_h$, where the mass splitting is small or negligible. This region has softer jet p_{T} requirements and an upper bound on the p_{T} of the leading b-tagged jet. As $SR_B^{1\ell 4b}$, it includes requirements on m_T. The optimization of the resolved signal region, $SR_C^{1\ell 4b}$, is based on the study of the signal model with $m_{\widetilde{t}_2} = 650$ GeV, $m_{\widetilde{t}_1} = 380$ GeV, $m_{\widetilde{\chi}_1^0} = 200$ GeV, shown as dashed line in (Fig.5.8).

In $SR_A^{1\ell 4b}$, the Higgs candidate is formed by the b-jet pair with smaller ΔR separation, using the method described in Sec.5.2. This variable is helpful in rejecting non-resonant backgrounds. This selection is not used in other SRs considering less boosted topologies because of the large combinatorial background.

Only events with one or two signal leptons are selected to ensure orthogonality with the $\widetilde{t}_2$ decay in $\widetilde{t}_1 + Z$ (presented in the next Chapter). At least one lepton is required to have $p_{\mathrm{T}} > 30$ GeV and the electron candidates must also satisfy the `TightLH` likelihood-based identification requirements. The final selection for each SR is shown in Tab.5.2.

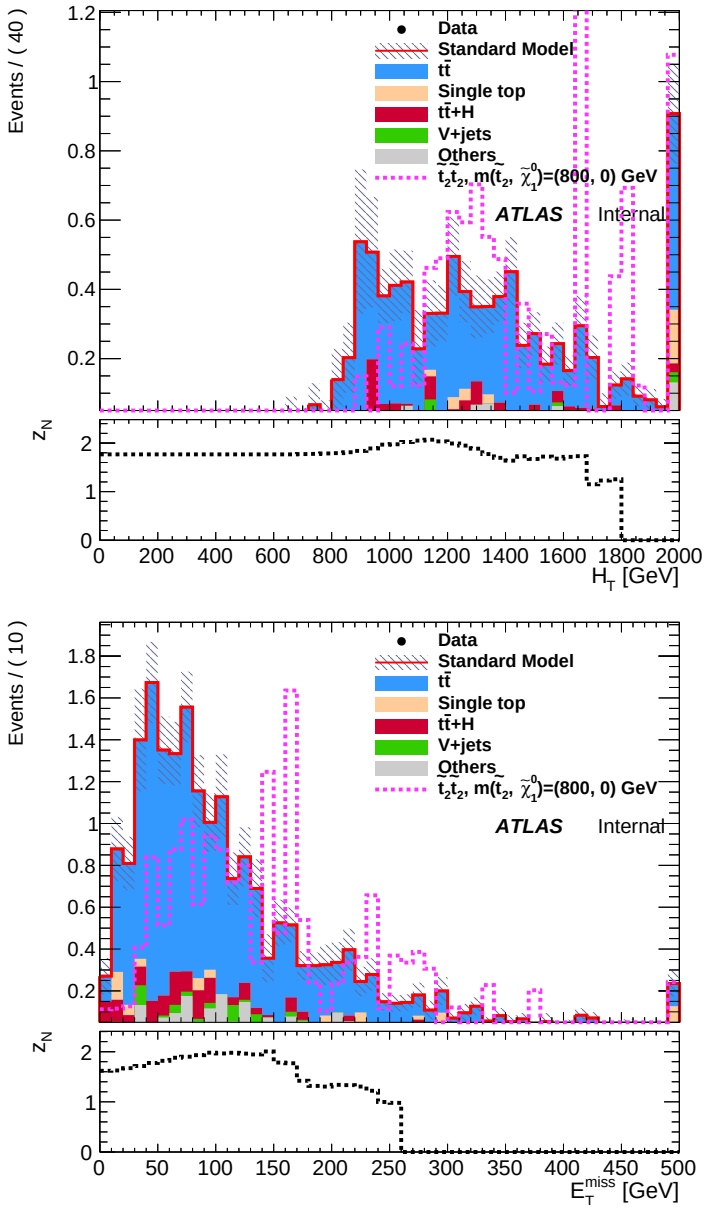

Figure 5.5: Distribution of the scalar sum of jet momenta H_T (top) and E_{T}^{miss} (bottom) for events lying in $SR_A^{1\ell 4b}$. The contribution from all SM backgrounds are shown; the bands represent the total uncertainty. The expected distributions for the signal model with $(m_{\tilde{t}_2}, m_{\tilde{\chi}_1^0}) = (800,0)$ GeV is also shown as a dashed line. The last bin in each figure contains the overflow. The lower panels show the significance of the signal model to the total SM background prediction.

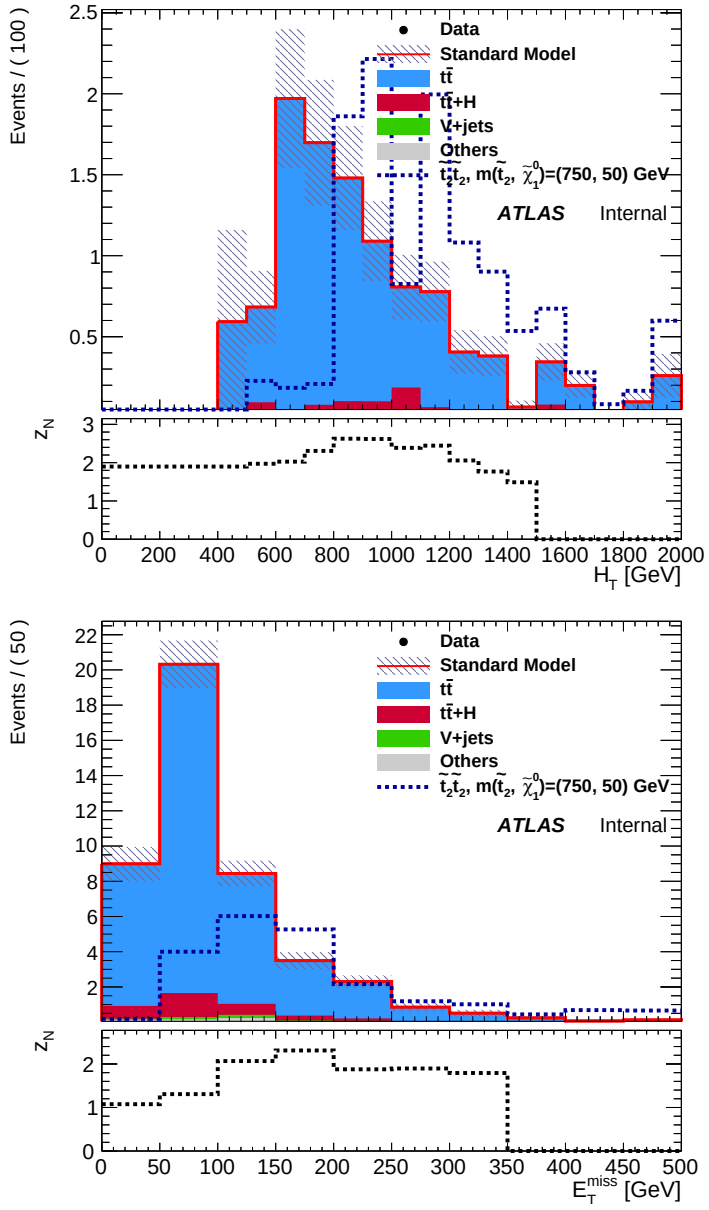

Figure 5.6: Distribution of the scalar sum of jet momenta H_T (top) and E_{T}^{miss} (bottom) for events lying in $SR_B^{1\ell 4b}$. The contribution from all SM backgrounds are shown; the bands represent the total uncertainty. The expected distributions for the signal model with $(m_{\tilde{t}_2}, m_{\tilde{\chi}_1^0}) = (750,50)$ GeV is also shown as a dashed line. The last bin in each figure contains the overflow. The lower panels show the significance of the signal model to the total SM background prediction.

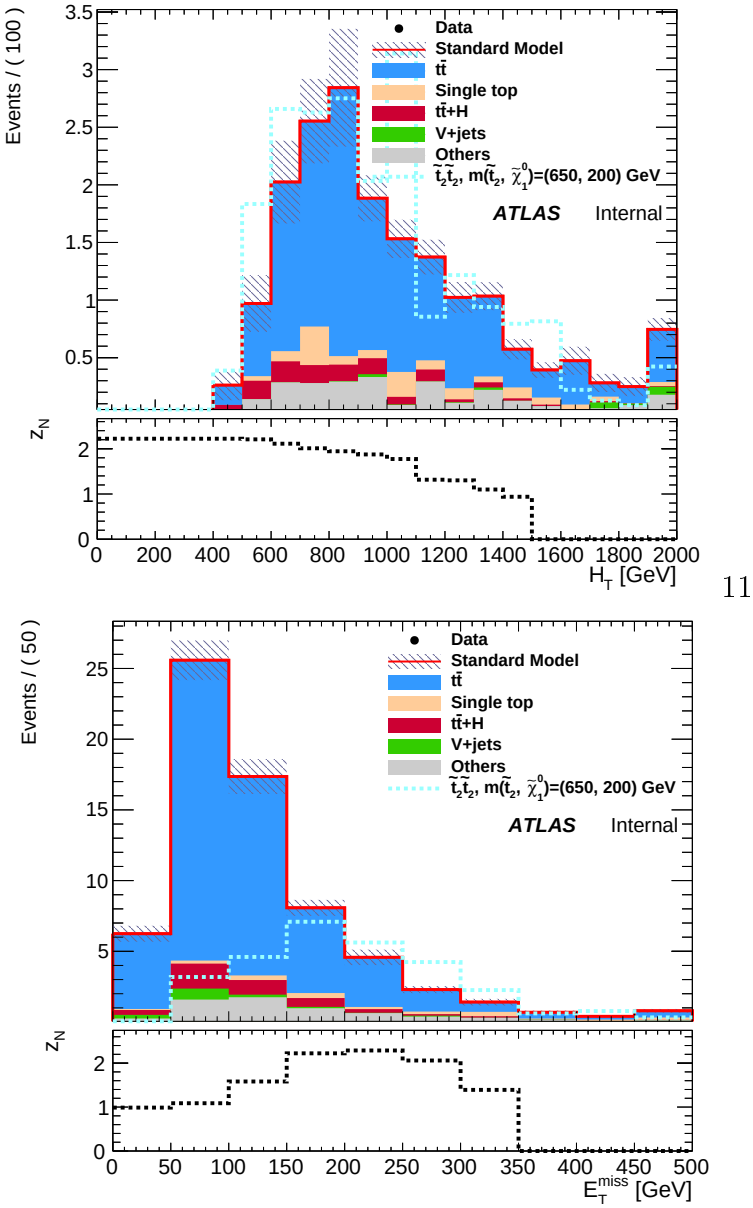

11

Figure 5.7: Distribution of the scalar sum of jet momenta H_T (top) and E_{T}^{miss} (bottom) for events lying in $SR_C^{1\ell 4b}$. The contribution from all SM backgrounds are shown; the bands represent the total uncertainty. The expected distributions for the signal model with $(m_{\tilde{t}_2}, m_{\tilde{\chi}_1^0}) = (650,200)$ GeV is also shown as a dashed line. The last bin in each figure contains the overflow. The lower panels show the significance of the signal model to the total SM background prediction.

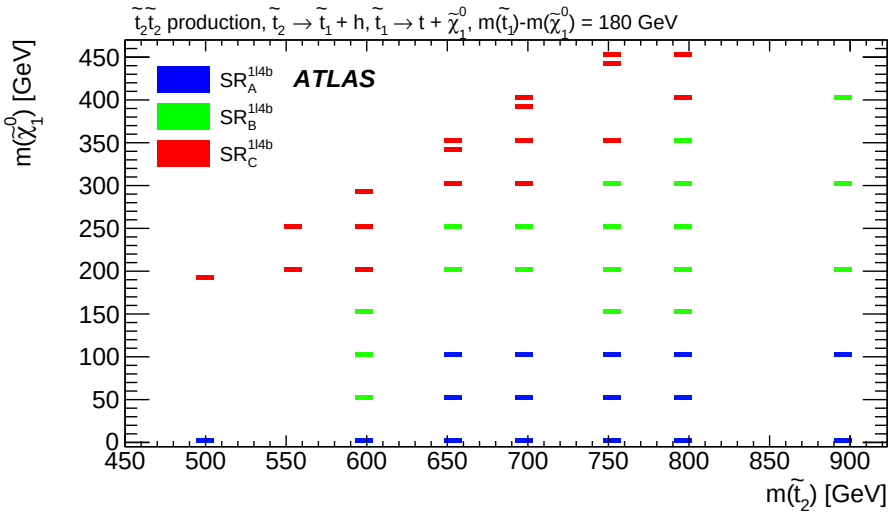

Figure 5.8: Signal Region with the highest significance for each of the mass models on the $\widetilde{t}_2 - \widetilde{\chi}_1^0$ mass plane, given the SR definitions in Tab.5.2.

Requirement/Region	$SR_A^{1\ell 4b}$	$SR_B^{1\ell 4b}$	$SR_C^{1\ell 4b}$
$n_{leptons}$	1–2	1–2	1–2
$n_{b-tagged\ jets}$	≥ 4	≥ 4	≥ 4
m_T [GeV]	–	> 150	> 125
H_T [GeV]	>1000	–	–
E_{T}^{miss} [GeV]	>120	> 150	>150
Leading b-tagged jet p_{T} [GeV]	–	–	<140
m_{bb} [GeV]	95–155	–	–
p_{bb}^T [GeV]	>300	–	–
$n_{jets}(p_{\mathrm{T}} > 60$ GeV)	≥6	≥5	–
$n_{jets}(p_{\mathrm{T}} > 30$ GeV)	–	–	≥7

Table 5.2: Definition of the three Signal Regions used in this anaysis. The three regions are based on the mass splitting between the $\widetilde{t}_2$ and the $\widetilde{t}_1$, aiming at different kinematics of the Higgs boson originating from the decay.

5.4 Background estimation

The main SM background processes satisfying the SR requirements are estimated by simulation, which is normalised and verified (whenever possible) with events from data in separate statistically independent regions of the phase space.
Dedicated control regions (*CRs*) enhanced in a particular background component, such as the production of $t\bar{t}$ pairs, are used for the normalisation. For each signal region, a simultaneous "background fit" is performed to the numbers of events found in the CRs, using a minimisation based on likelihoods with the HistFitter [67] package.
In each fit, the normalisation of the background contributions having dedicated CRs are allowed to float freely, while the other backgrounds are determined directly using simulation from independent studies in data. This way the total post-fit prediction is forced to be equal to the number of data events in the CR and its total uncertaintly is given by the data statistical uncertainty. When setting 95% confidence level (*CL*) upper limits on the cross-section of specific SUSY models, the simultaneous fits also include the observed yields in the SR. Systematic uncertainties in the MC simulation affect the ratio of the expected yields in the different regions and are taken into account to determine the uncertainty in the background prediction. Each uncertainty source is described by a single nuisance parameter, and correlations between background processes and selections are taken into account. The fit affects neither the uncertainty nor the central value of these nuisance parameters.
Whenever possible, the level of agreement of the background prediction with data is compared in dedicated validation regions (*VRs*), which are not used to constrain the background normalisation or nuisance parameters in the fit.

The dominant SM background contribution is expected to be top quark pair ($t\bar{t}$) production, amounting to more than 80% of the total background. The normalisation of the $t\bar{t}$ background for each of the three SRs is obtained by fitting the yield to the observed data in a dedicated CR, then extrapolating this yield to the SRs as described above. Other background sources (single top, $t\bar{t}h$ and rare SM processes), which provide a subdominant contribution to the SRs, are determined from MC simulation only.
The background yields N^{obs}(CR) observed in each control region is related to the backgrounds yields by the equation

$$N^{obs}(CR) = \mu_{t\bar{t}} N^{MC}_{t\bar{t}}(CR) + N^{MC}_{others}(CR) \tag{5.6}$$

where $N^{MC}_{t\bar{t}}$(CR) is the yield predicted by MC in the CR for $t\bar{t}$ events. The μ terms is the scale factor which is applied to this background. N^{MC}_{others}(CR) is the MC yield for the minor background processes.
The scale factor $\mu_{t\bar{t}}$ is determined from Eq.5.6 in the CR. The expected background in the SRs is then given by the same equation

$$N^{obs}(SR) = \mu_{t\bar{t}} N^{MC}_{t\bar{t}}(SR) + N^{MC}_{others}(SR) \tag{5.7}$$

With this approach, the main background source in the SRs is measured by

	$\mu_{t\bar{t}}$
$SR_A^{1\ell 4b}$	1.7415 ± 0.0726
$SR_B^{1\ell 4b}$	1.8981 ± 0.116
$SR_C^{1\ell 4b}$	1.8579 ± 0.0693

Table 5.3: Scale factors for the $t\bar{t}$ background in the three SRs. The scale factors are obtained by comparing SM predictions with data in regions where the background is dominant. This process involved the use of 36.5 fb^{-1} of data coming from $\sqrt{s}$ = 13 TeV acquired by the ATLAS detector in the 2015 + 2016 period.

weighting the MC predictions with a scale factor derived from the normalisation of the MC to the data of the CR.
The contribution from events with fake or non-prompt leptons is found to be negligible in this selection. The three $t\bar{t}$ CRs (named $CR_A^{1\ell 4b}$, $CR_B^{1\ell 4b}$ and $CR_C^{1\ell 4b}$) are described in Tab.5.4. They are designed to have kinematic properties resembling as closely as possible those of each of the three SRs ($SR_A^{1\ell 4b}$, $SR_B^{1\ell 4b}$, $SR_C^{1\ell 4b}$, respectively), while having a high purity in $t\bar{t}$ background and only a small contamination from signal. The CRs are built by inverting the SR requirements on E_{T}^{miss} and relaxing or inverting those on m_{bb} or m_T. Fig.5.10 shows the jet multiplicity distributions in these CRs after the background fit.

Requirement/Region	$CR_A^{1\ell 4b}$	$CR_B^{1\ell 4b}$	$CR_C^{1\ell 4b}$
$n_{leptons}$	1–2	1–2	1–2
$n_{b-tagged\ jets}$	≥ 4	≥ 4	≥ 4
m_T [GeV]	–	> 100	<125
E_{T}^{miss} [GeV]	<120	< 150	<150
Leading b-tagged jet p_{T} [GeV]	–	–	<140
m_{bb} [GeV]	95–155	–	–
p_{bb}^T [GeV]	>300	–	–
$n_{jets}(p_{\mathrm{T}} > 60$ GeV)	≥ 5	≥ 5	–
$n_{jets}(p_{\mathrm{T}} > 30$ GeV)	–	–	≥ 7

Table 5.4: Definition of the three Control Regions for the $t\bar{t}$ background fit used in this anaysis.

In a similar manner, three validation regions (named $VR_A^{1\ell 4b}$, $VR_B^{1\ell 4b}$, $VR_C^{1\ell 4b}$) are defined, each of them corresponding to a different CR, with the same requirements on E_{T}^{miss} as the SR and relaxing or inverting the requirements on m_{bb}, m_T or jet multiplicity, as shown in Tab. 5.5. These VRs are used to provide a statistically independent cross-check of the extrapolation in a selection close to that of the SR but with small signal contamination. The large correction to $t\bar{t}$ normalisation after the background fit has also been observed in other analyses and is due to a mismodelling of the $t\bar{t} + b\bar{b}$, $c\bar{c}$ component in the MC simulation.
Fig. 5.11 shows the jet multiplicity distributions in these VRs after the background fit.

Requirement/Region	$VR_A^{1\ell 4b}$	$VR_B^{1\ell 4b}$	$VR_C^{1\ell 4b}$
$n_{leptons}$	1–2	1–2	1–2
$n_{b-tagged\ jets}$	≥ 4	≥ 4	≥ 4
m_T [GeV]	–	> 150	<125
E_{T}^{miss} [GeV]	>120	> 150	>150
Leading b-tagged jet p_{T} [GeV]	–	–	<140
m_{bb} [GeV]	$\notin[95,155]$	–	–
p_{bb}^T [GeV]	>300	–	–
$n_{jets}(p_{\mathrm{T}} >60$ GeV)	≥ 5	≤ 4	–
$n_{jets}(p_{\mathrm{T}} >30$ GeV)	–	–	≥ 7

Table 5.5: Definition of the three Validation Regions for the $t\bar{t}$ background fit used in this anaysis.

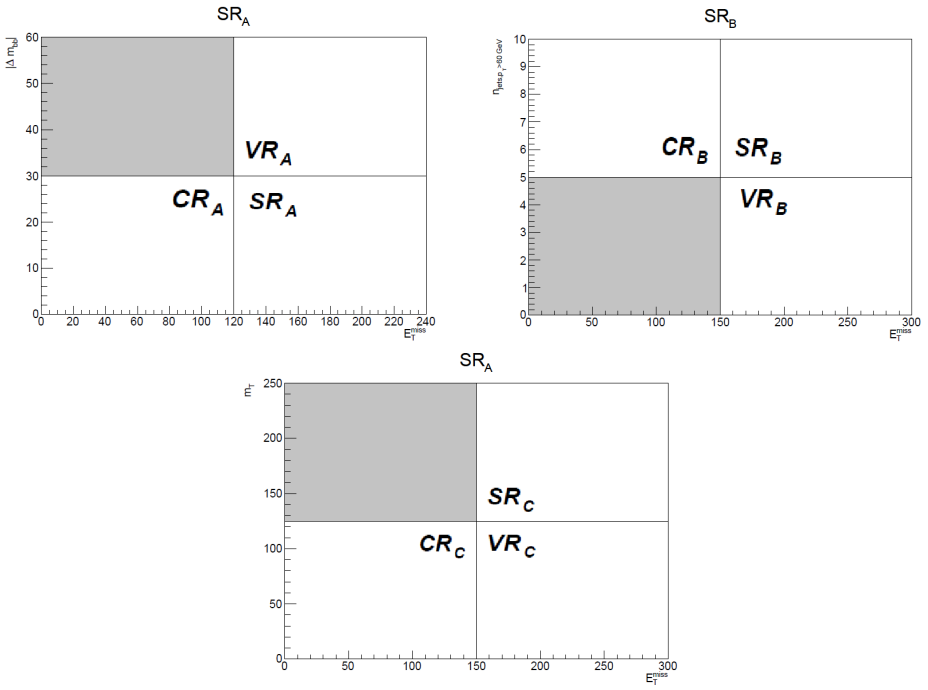

Figure 5.9: Block visualization of the requirement difference between the SR, the CR and the VR for each of the three selections $SR_A^{1\ell 4b}$, $SR_B^{1\ell 4b}$ and $SR_C^{1\ell 4b}$. The CRs and VRs for each selection are statistically independent and are built by inverting the requirement on E_{T}^{miss} plus a second requirement, depending on the selection. For $SR_A^{1\ell 4b}$, the requirement of a reconstructed bb pair close to the Higgs boson mass in inverted for $VR_A^{1\ell 4b}$. For $SR_B^{1\ell 4b}$, the requirement on the number of high-p_{T} (> 60 GeV) jets in inverted for $VR_B^{1\ell 4b}$. For $SR_C^{1\ell 4b}$, the requirement on the transverse mass in inverted for both $CR_C^{1\ell 4b}$ and $VR_C^{1\ell 4b}$.

The background prediction is in agreement with the observed data in all VRs. A visualization of the requirement difference between the SR, the CR and the VR for each of the three selections $SR_A^{1\ell 4b}$, $SR_B^{1\ell 4b}$ and $SR_C^{1\ell 4b}$ is presented in Fig. 5.9.

Figure 5.10: Jet multiplicity distributions in control regions $CR_A^{1\ell 4b}$ (a), $CR_B^{1\ell 4b}$ (b) and $CR_C^{1\ell 4b}$ (c) after normalising the $t\bar{t}$ background process via the simultaneous fit described in Sec. 5.4. The contributions from all SM backgrounds are shown as a histogram stack; the bands represent the total uncertainty. The "*Others*" category contains the contributions from $t\bar{t}h$, $t\bar{t}WW$, $t\bar{t}t$, $t\bar{t}t\bar{t}$, Wh, and Zh production. The lower panels show the ratio of the observed data to the total SM background prediction, with the bands representing the total uncertainty in the background prediction

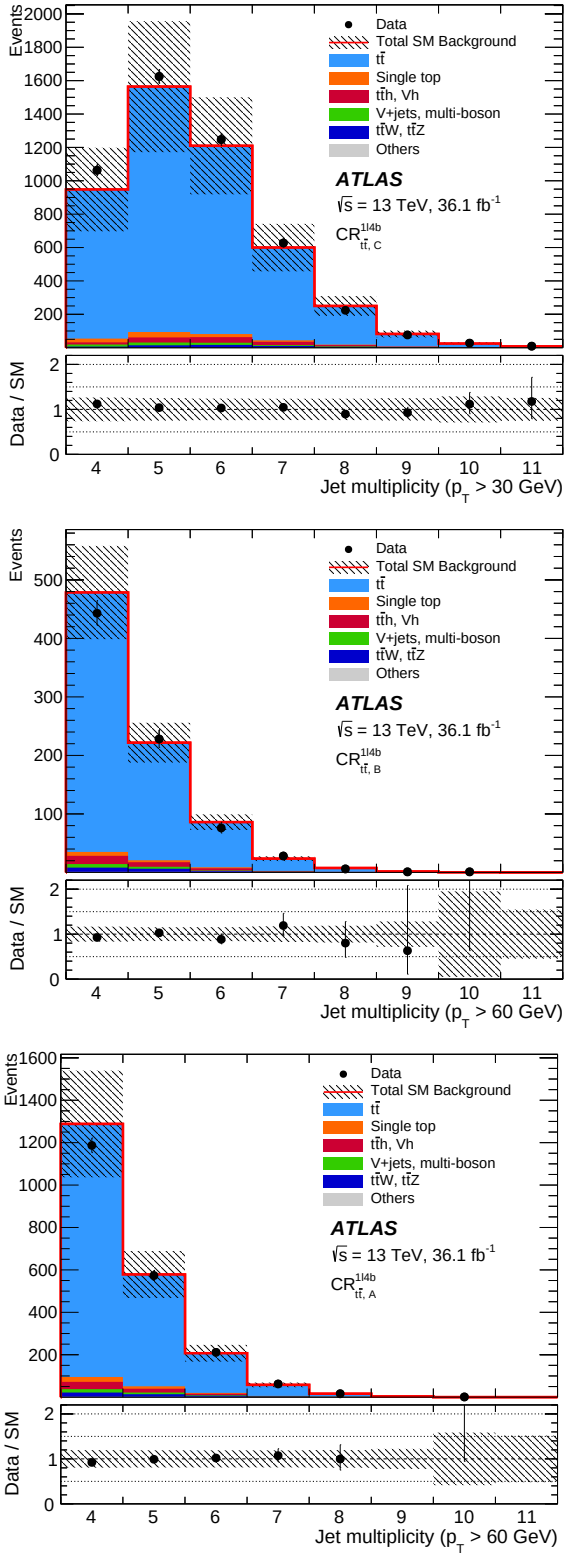

Figure 5.11: Missing transverse energy distributions in validation regions $VR_A^{1\ell 4b}$ (a), $VR_B^{1\ell 4b}$ (b) and $VR_C^{1\ell 4b}$ (c) after normalising the $t\bar{t}$ background process via the simultaneous fit described in Sec. 5.4. The contributions from all SM backgrounds are shown as a histogram stack; the bands represent the total uncertainty. The "*Others*" category contains the contributions from $t\bar{t}h$, $t\bar{t}WW$, $t\bar{t}t$, $t\bar{t}t\bar{t}$, Wh, and Zh production. The lower panels show the ratio of the observed data to the total SM background prediction, with the bands representing the total uncertainty in the background prediction

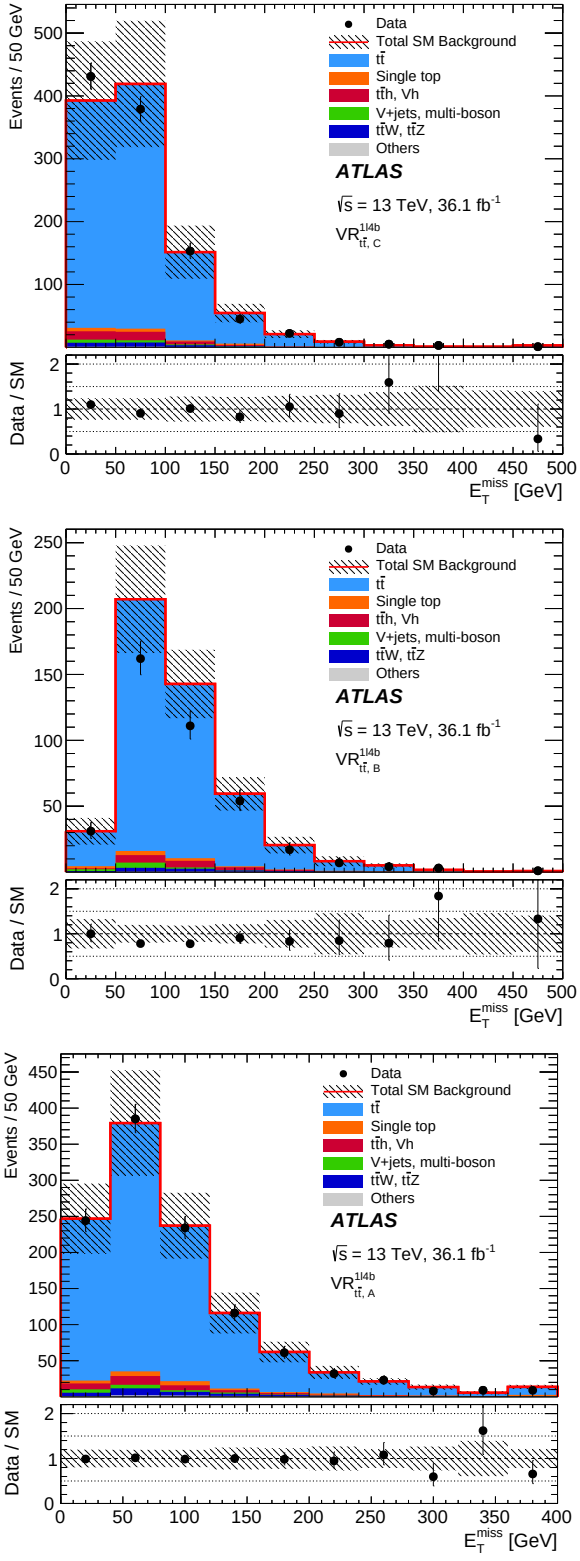

5.5 Systematic uncertainties

Systematic uncertainties are associated with the predictions of all background components and the expected signal yields. The systematic uncertainties can be categorized into two sources: experimental and theoretical uncertainties.
In this section the impact on the analysis of various sources of systematic uncertainties is described. In addition to these, also the statistical uncertainty coming from the limited MC statistics, which is often denoted as "stat.", has to be considered.
The primary sources of systematic uncertainty are related to the jet energy scale, the jet energy resolution, the theoretical and the MC modelling uncertainties in the background determined using CRs ($t\bar{t}$). The statistical uncertainty of the simulated event samples is taken into account as well.
The effects of the systematic uncertainties are evaluated for all signal samples and background processes. Since the normalisation of the dominant background processes is extracted in dedicated CRs, the systematic uncertainties only affect the extrapolation to the SRs in these cases.

Jet energy uncertainties: The jet energy scale and resolution uncertainties are derived as a function of the p_{T} and η of the jet, as well as of the pile-up conditions and the jet flavour composition (more quark-like or gluon-like) of the selected jet sample. They are determined using a combination of simulated and data samples.

- **Jet energy scale (JES):** The absolute jet energy scale and η calibration corrects the reconstructed jet four-momentum to the particle-level energy scale and accounts for biases in the jet η reconstruction [65]. Such biases are primarily caused by the transition between different calorimeter technologies and sudden changes in calorimeter granularity. The calibration is derived from the PYTHIA MC sample using reconstructed jets after the application of the origin and pile-up corrections. The JES calibration is derived first as a correction of the reconstructed jet energy to the truth jet energy.

- **Jet energy resolution (JER):** An extra p_{T} smearing is added to the jets based on their p_{T} and η to account for a possible underestimate of the jet energy resolution in the MC simulation, as done by the `JERSmearingTool` in the `JetResolution` package [66].

E_{T}^{miss}**:** The systematic uncertainties related to the modelling of E_{T}^{miss} in the simulation are estimated by propagating the uncertainties in the energy and momentum scale of all identified electrons, photons, muons and jets, as well as the uncertainties in the soft-term scale and resolution.

Pile-up reweighting: computed varying the nominal pile-up value scaling, as presented in Sec. 2.1.

$b-$**tagging:** Uncertainties associated with the modelling of the $b-$tagging efficiencies for $b-$jets, $c-$jets and $light-$flavour jets are also considered.

	$SR_A^{1\ell 4b}$	$SR_B^{1\ell 4b}$	$SR_C^{1\ell 4b}$
Total systematic uncertainty (%)	22	17	30
$t\bar{t}$ theoretical uncertainty (%)	17	14	22
Other theoretical uncertainty (%)	1.6	2.4	1.7
MC statistical uncertainty (%)	7.3	5.2	1.7
$t\bar{t}$ fitted normalisation (%)	3.4	5.1	3.3
Fake or non-prompt leptons (%)	–	–	–
Pile-up (%)	<1	1.4	<1
Jet energy resolution (%)	5.3	<1	13
Jet energy scale (%)	3.2	5.3	6.1
E_{T}^{miss} resolution (%)	6.8	6.5	4.0
b-tagging (%)	6.8	2.9	3.5

Table 5.6: Summary of the main systematic uncertainties and their impact (in %) on the total SM background prediction in each of the signal regions studied. The total systematic uncertainty can be different from the sum in quadrature of individual sources due to the correlations between them resulting from the fit to the data. The quoted theoretical uncertainties include modelling and cross-section uncertainties.

Luminosity: The integrated luminosity was established from a preliminary calibration of the luminosity scale using a pair of $x-y$ beam separation scans performed in June 2015 and May 2016.

Other detector-related systematic uncertainties, such as those in the lepton reconstruction efficiency, energy scale and energy resolution, and in the modelling of the trigger, are found to have a small impact on the results.

Regarding theoretical systematics uncertainties, the approach for Run-2 data is based on truth level generator comparisons for all those background sources which are not fully estimated from data.

$t\bar{t}$ **Generator/Hard scatter:** the uncertainty arising from the choice of parton level generator is estimated by comparing the predictions from POWHEG-BOX with MADGRAPH5_aMC@NLO 2.1.1. The full difference between the two generators is used and symmetrized.

$t\bar{t}$ **Fragmentation/Hadronization:** the uncertainty associated with the parton shower modelling is assessed as the difference between the predictions from POWHEG with PYTHIA 6.428 and HERWIG 2.7.1.

$t\bar{t}$ **QCD scale and Additional Radiation:** the uncertainty related to the choice of QCD normalisation and factorisation scales are assessed by varying the corresponding generator parameters up and down by a factor of two around their nominal values using POWHEG+PYTHIA samples with variable shower radiation (P2012 RADLO and RADHI).

$t\bar{t}$ + **Heavy Flavours fraction uncertainty:** the uncertainty is assessed

with an (independent) truth level reweighting of the $t\bar{t}+ \geq 1b$ and $t\bar{t}+ \geq 1c$ components in the nominal $t\bar{t}$ sample varied up by 50%. The background fit is repeated with the re-weighted samples and the prediction difference in the SR is symmetrized and taken as uncertainty.

The cross-sections used to normalise the MC samples are varied according to the uncertainty in the cross-section calculation. Tab. 5.6 summarises the contributions of the different sources of systematic uncertainty for the total SM background predictions in the signal regions. The dominant systematic are due to $t\bar{t}$ modelling.

Chapter 6

Results and Interpretations

The studies presented in the previous chapter are here applied to data obtained by the ATLAS experiment in the period 2015-16. A first step is the search for excesses or deviations from the SM predictions caused by possible BSM physics. The distributions of the main kinematic variables of this decay are analyzed after the selections presented in Chapter 5 are applied to both the Data and the simulated SM background. Lower exclusion limits are then extracted from these distributions for the masses of $\widetilde{t}_2$, $\widetilde{t}_1$ and $\widetilde{\chi}_1^0$.

The kinematic likeness of the $\widetilde{t}_2 \rightarrow \widetilde{t}_1 + h$ decay with the corresponding EW mediated $\widetilde{t}_2 \rightarrow \widetilde{t}_1 + Z$, allows to combine the limits obtained for both channels and to strenghten the exclusion of mass models for the aforementioned particles. Finally, it is presented a decay channel with an identical signature with respect to the ones presented, allowing for re-interpretation of the results: the decay $\widetilde{t}_1 \rightarrow t + \widetilde{\chi}_2^0$, with subsequent decay $\widetilde{\chi}_2^0 \rightarrow \widetilde{\chi}_1^0 + h/Z$.

6.1 Kinematic distributions

In this section, the kinematic distribution of the variables used in this analysis is presented, after the selections presented in Sec.5.1 are applied, the $t\bar{t}$background is re-weighted and the uncertainties are estimated. Under each distribution, the ratio of the observed data to the total SM prediction is shown. For a purely SM distribution, only statistical fluctuations around the value of 1 are expected for this ratio. On the other hand, a significant discrepancy between the Data and the SM predictions could suggest the presence of BSM physics.
As can be seen in Fig.6.1 and 6.2, the expected SM background fits data within uncertainty.

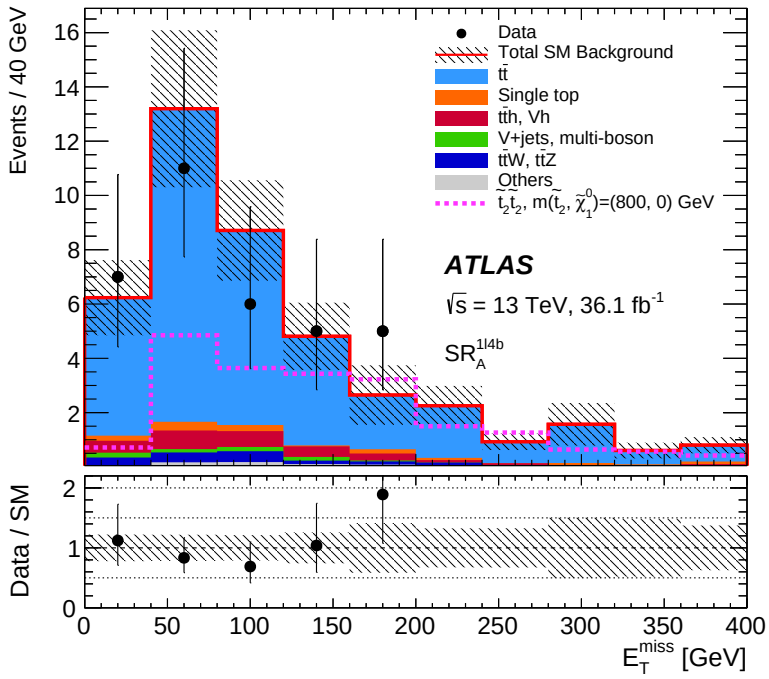

Figure 6.1: Distribution of E_{T}^{miss} for events passing all the signal candidate selection requirements, except that on E_{T}^{miss}, for the signal region SR_A after the background fit described in Subsection 5.4. The contribution from all SM backgrounds are shown; the bands represent the total uncertainty. The expected distributions for a signal model with $(m_{\tilde{t}_2}, m_{\tilde{\chi}_1^0}) = (800,0)$ GeV is also shown as dashed line. The last bin in each figure contains the overflow. The lower panels show the ratio of the observed data to the total SM background prediction, with the bands representing the total uncertainty in the background prediction.

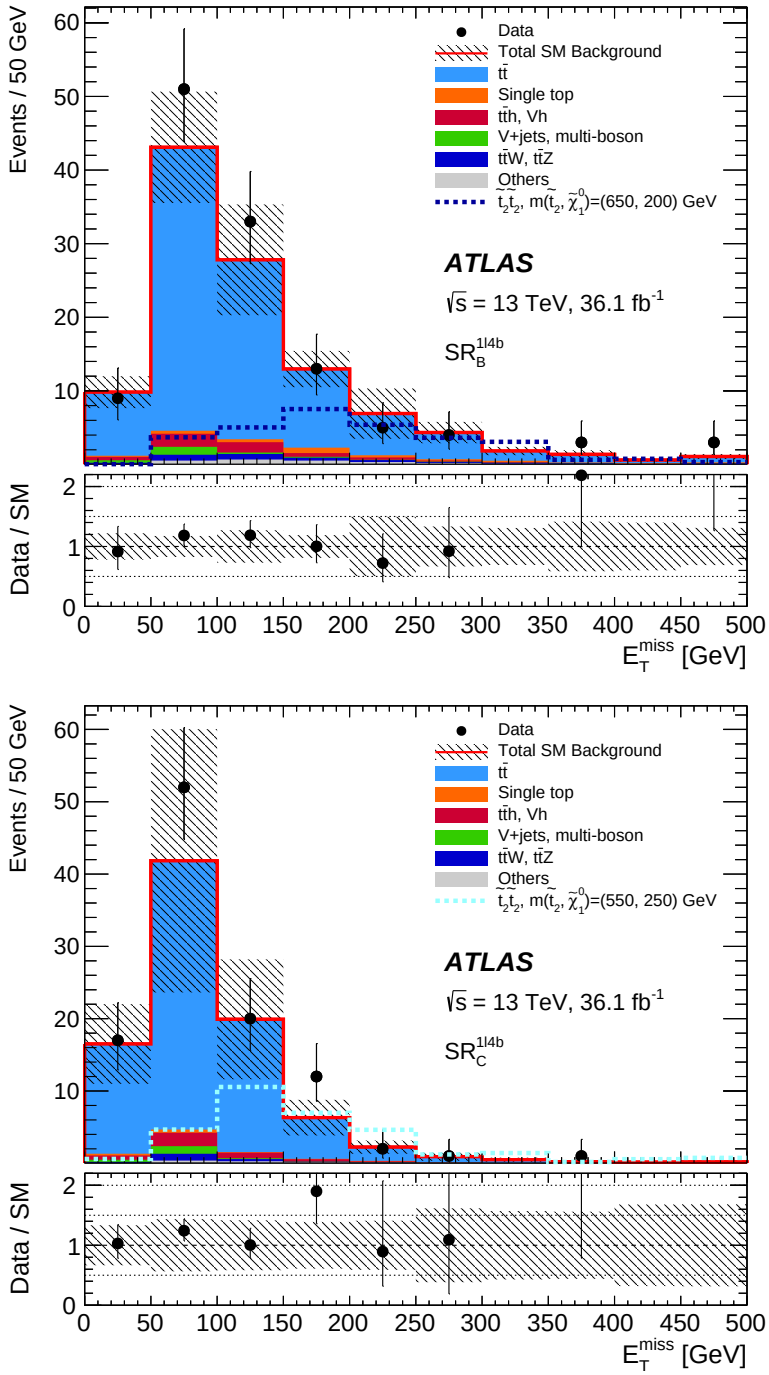

Figure 6.2: Distribution of E_{T}^{miss} for events passing all the signal candidate selection requirements, except that on E_{T}^{miss}, for the signal regions SR_B(top) and SR_C(bottom) after the background fit described in Sec. 5.4. The contribution from all SM backgrounds are shown; the bands represent the total uncertainty. The expected distributions for signal models with $(m_{\tilde{t}_2}, m_{\tilde{\chi}_1^0}) = (650,200)$ GeV and $(m_{\tilde{t}_2}, m_{\tilde{\chi}_1^0}) = (550,250)$ GeV are also shown as dashed lines. The last bin in each figure contains the overflow. The lower panels show the ratio of the observed data to the total SM background prediction, with the bands representing the total uncertainty in the background prediction.

6.2 Signal yield and limit setting

The observed number of events and expected yields are shown in Tab.6.1 for each of the three signal regions. Data agree with the SM background prediction within uncertainties and thus exclusion limits for several beyond-the-SM (BSM) scenarios are extracted.

The HistFitter framework, which utilises a profile-likelihood-ratio-test statistic, is used to estimate 95 % confidence intervals using the CL_S prescription. The likelihood is built as the product of a probability density function describing the observed number of events in the SR and the associated CR(s) and, to constrain the nuisance parameters associated with the systematic uncertainties, Gaussian distributions whose widths correspond to the sizes of these uncertainties; Poisson distributions are used instead to model statistical uncertainties affecting the observed and predicted yields in the CRs. Tab.6.1 also shows upper limits (at the 95% CL) on the visible BSM cross-section $\sigma_{vis} = S^{95}_{obs}/\mathcal{L}dt$, defined as the product of the production cross-section, acceptance and efficiency.

Model-dependent limits are also set in specific classes of SUSY models. For each signal hypothesis, the background fit is redone taking into account the signal contamination in the CRs, which is found to be below 15% for signal models close to the Run-1 exclusion limits. All uncertainties in the SM prediction are considered, including those that are correlated between signal and background (for instance, jet energy scale uncertainties), as well as all uncertainties in the predicted signal, excluding PDF- and scale-induced uncertainties in the theoretical cross-section. Since the three SRs are not orthogonal, only the SR with best expected sensitivity is used for each signal point. "Observed limits" are calculated from the observed event yields in the SRs. "Expected limits" are calculated by setting the nominal event yield in each SR to the corresponding mean expected background.

Limits for simplified models, in which pair-produced $\widetilde{t}_2$ decay with 100% branching ratio into the $\widetilde{t}_1$ and a h boson, with $\widetilde{t}_1 \rightarrow t\ \widetilde{\chi}^0_1$, in the $\widetilde{t}_2 - \widetilde{\chi}^0_1$ plane are shown in Fig.7.1. Assuming 100% branching ratio into $\widetilde{t}_1$ and a h boson, $\widetilde{t}_2$ masses up to 880 GeV are excluded at 95% CL for a $\widetilde{\chi}^0_1$ of about 50 GeV, and $\widetilde{\chi}^0_1$ masses up to 260 GeV are excluded for $\widetilde{t}_2$ masses between 650 and 710 GeV. These results extend the previous limits on the $\widetilde{t}_2$ mass from ATLAS $\sqrt{s} = 8$ TeV analyses by up to 250 GeV depending on the $\widetilde{\chi}^0_1$ mass.

	SR_A	SR_B	SR_C
Observed events	10	28	16
Total (post-fit) SM events	13.6 ± 3.0	29 ± 5	10.5 ± 3.2
Fit output, $t\bar{t}$	11.3 ± 2.9	24 ± 5	9.3 ± 3.1
Single top	0.50 ± 0.18	1.7 ± 0.4	0.24 ± 0.07
V+jets, multi-boson	0.20 ± 0.15	0.23 ± 0.10	0.01 ± 0.01
$t\bar{t}h$, Vh	0.89 ± 0.16	1.19 ± 0.35	0.56 ± 0.13
$t\bar{t}W$, $t\bar{t}Z$	0.36 ± 0.21	1.09 ± 0.31	0.10 ± 0.10
Others	0.37 ± 0.20	1.33 ± 0.69	0.34 ± 0.18
Fit input, $t\bar{t}$	7.1	14	6.0
S^{95}_{obs}	7.8	14.6	15.6
S^{95}_{exp}	$9.6^{+4.1}_{-2.3}$	$15.5^{+5.6}_{-4.4}$	$10.4^{+4.2}_{-2.6}$
σ_{vis} [fb]	0.21	0.40	0.43
$p(s = 0)$	0.63	0.82	0.11

Table 6.1: Observed and expected numbers of events in the three signal regions. The nominal predictions from MC simulation are given for the $t\bar{t}$background. The "Others" category contains the contributions from $t\bar{t}WW$, $t\bar{t}t$, $t\bar{t}t\bar{t}$, tZ, and tWZ production. Combined statistical and systematic uncertainties are given. Signal model-independent 95% CL upper limits on the visible BSM cross-section (σ_{vis}), the visible number of signal events (S^{95}_{obs}), the number of signal events (S^{95}_{exp}) given the expected number of background events (and $\pm 1\sigma$ variations of the expected background), and the discovery p-value ($p(s = 0)$), all calculated with pseudo-experiments, are also shown for each signal region.

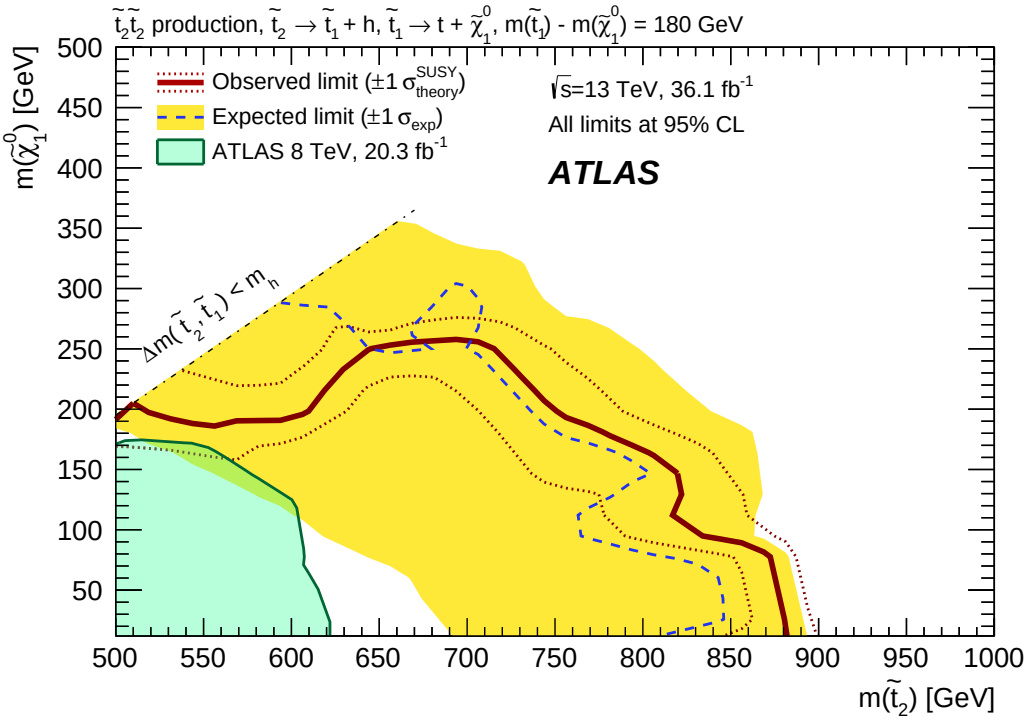

Figure 6.3: Exclusion limits at 95% CL from the analysis of 36.1 fb^{-1} of 13 TeV pp collision data on the masses of the $\widetilde{t}_2$ and $\widetilde{\chi}_1^0$, for a fixed mass splitting $m_{\widetilde{t}_1} - m_{\widetilde{\chi}_1^0} = 180$ GeV and assuming $\mathcal{B}(\widetilde{t}_2 \to \widetilde{t}_1 + Z) = 1$. The dashed line and the shaded band are the expected limit and its $\pm 1\sigma$ uncertainty, respectively. The thick solid line is the observed limit for the central value of the signal cross-section. The expected and observed limits do not include the effect of the theoretical uncertainties in the signal cross-section. The dotted lines show the effect on the observed limit when varying the signal cross-section by $\pm 1\sigma$ of the theoretical uncertainty. The shaded area in the lower-left corner shows the observed exclusion from the ATLAS $\sqrt{s} = 8$ TeV analysis.

6.3 The $\widetilde{t}_2 \to \widetilde{t}_1 + Z$ decay

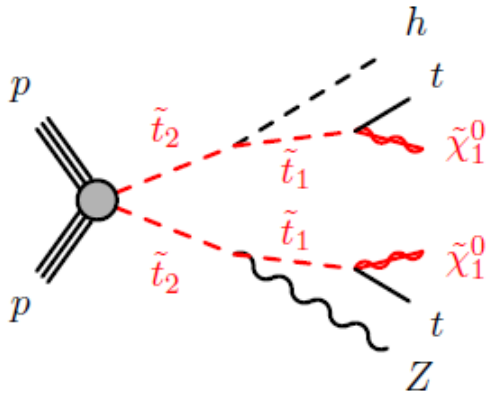

Figure 6.4: Diagram for the top squark pair production process $\widetilde{t}_2 \to \widetilde{t}_1 + Z$.

In alternative to the process involving an Higgs boson $\widetilde{t}_2 \rightarrow \widetilde{t}_1 + h$, the $\widetilde{t}_2$ could also decay into a $\widetilde{t}_1$ with a Z boson in the decay chain:

$$\widetilde{t}_2 \rightarrow \widetilde{t}_1 + Z \tag{6.1}$$

with the subsequent decay of the $\widetilde{t}_1$ following the same dynamics as the decay explained in the last chapter.
Such signals can be discriminated from the SM top quark pair production ($t\bar{t}$) background by requiring a same-flavour opposite-sign lepton pair originating from the decay of the Z (Fig. 6.4):

$$Z \rightarrow \ell^+\ell^- \tag{6.2}$$

Due to the relative similarities between the two searches, it proved to be possible to share part of the analysis approach. This joined-effort eventually led to a shared paper [69] detailing the combined results of the two search branches. While just a brief overview of the analysis strategy is given below, an extensive discussion of the subject can be found in [69]. The selection of events used in this analysis is identical to the one presented in Sec. 5.1 and the general approach is shared between the two searches, except for the pre-selection requirements, which are focused on the reconstruction of the leptonic decay of the Z boson. Events of interest are selected if they contain at least three signal leptons (electrons or muons), with at least one same-flavour opposite-sign lepton pair whose invariant mass is compatible with the Z boson mass ($|m_{\ell\ell} - m_Z| < 15$ GeV, with $m_Z = 91.2$ GeV).

In the same fashion as the Higgs boson branch, in order to maximize the sensitivity in different regions of the mass parameter space, three overlapping signal regions are defined as shown in Tab. 6.2. Signal region $SR_{A,Z}$ is optimised for large $\widetilde{t}_2 - \widetilde{\chi}_1^0$ mass splitting, where the Z boson in the $\widetilde{t}_2 \rightarrow \widetilde{t}_1 + Z$ decay is boosted, and large $p_T^{\ell\ell}$ and leading-jet p_T are required. Signal region $SR_{B,Z}$ covers the intermediate case, featuring slightly softer kinematic requirements than in $SR_{A,Z}$. Signal region $SR_{C,Z}$ is designed to improve the sensitivity for compressed spectra ($m_{\widetilde{t}_2} \geq m_{\widetilde{\chi}_1^0} + m_t + m_Z$) with softer jet-$p_T$ requirements and an upper bound on $p_T^{\ell\ell}$.

The dominant SM background contribution to the SRs for the $\widetilde{t}_2 \rightarrow \widetilde{t}_1 + Z$ search is expected to be from $t\bar{t}Z$, with minor contribution from multi-boson production (mainly WZ) and backgrounds containing jets misidentified as leptons (hereafter referred to as "fake" leptons) or non-prompt leptons from decays of hadrons (mainly in $t\bar{t}$events). The normalisation of the main backgrounds ($t\bar{t}Z$, multi-boson) is obtained by fitting the yield to the observed data in two control regions, then extrapolating this yield to the SRs. Backgrounds from other sources ($t\bar{t}W$, $t\bar{t}h$ and rare SM processes), which provide a subdominant contribution to the SRs, are determined from MC simulation only.

The background from fake or non-prompt leptons is estimated from data. Two types of lepton identification criteria are defined for this evaluation: "tight"

Requirement/Region	$SR_{A,Z}$	$SR_{B,Z}$	$SR_{C,Z}$
$n_{leptons}$	≥ 3	≥ 3	≥ 3
$n_{b-tagged\ jets}$	≥ 1	≥ 1	≥ 1
$\lvert m_{\ell\ell} - m_Z \rvert$ [GeV]	< 15	< 15	< 15
Leading lepton p_T [GeV]	> 40	> 40	> 40
Leading jet p_T [GeV]	> 250	> 80	> 60
Leading b-tagged jet p_T [GeV]	> 40	> 40	> 40
$n_{jets}(p_T > 30$ GeV)	≥ 6	≥ 6	≥ 5
E_{T}^{miss} [GeV]	>100	> 180	>140
$p_T^{\ell\ell}$ [GeV]	> 150	–	< 80

Table 6.2: Definition of the three Signal Regions used in the Z-decay anaysis. The three regions are based on the mass splitting between the $\widetilde{t}_2$ and the $\widetilde{t}_1$, aiming at different kinematics of the Z boson originating from the decay.

and "loose", corresponding to the signal and candidate electrons and muons described in Sec. 4.7. The leading lepton is considered to be prompt, which is a valid assumption in more than 95% of the cases according to simulations. The method makes use of the number of observed events with the second and third leading leptons being loose–loose, loose–tight, tight–loose and tight–tight in each region. The probability for prompt leptons satisfying the loose selection criteria to also satisfy the tight selection is measured using a data sample enriched in $Z \rightarrow \ell^+\ell^-$ ($\ell = e, \mu$) decays. The equivalent probability for fake or non-prompt leptons is measured using events with one electron and one muon with the same charge.

The number of events with one or two fake or non-prompt leptons is calculated from these probabilities and the number of observed events with loose and tight leptons. The modelling of the background from fake or non-prompt leptons is validated in events passing a selection similar to the SRs, but removing the E_{T}^{miss} requirements and inverting the $m_{\ell\ell}$ requirements.

Results: The observed number of events and expected yields are shown in Tab. 6.3 for each of the three signal regions. Data agree with the SM background prediction within uncertainties and thus exclusion limits for several beyond-the-SM (BSM) scenarios are extracted.

In analogy with the results of the search involving a decay with the Higgs boson, limits for simplified models, in which pair-produced $\widetilde{t}_2$ decay with 100% branching ratio into the $\widetilde{t}_1$ and a Z boson, with $\widetilde{t}_1 \rightarrow t\ \widetilde{\chi}_1^0$, in the $\widetilde{t}_2 - \widetilde{\chi}_1^0$ mass plane have been computed.In this case, $\widetilde{t}_2$ masses up to 800 GeV are excluded at 95% CL for a $\widetilde{\chi}_1^0$ of about 50 GeV and $\widetilde{\chi}_1^0$ masses up to 350 GeV are excluded for $\widetilde{t}_2$ masses below 650 GeV.

Exclusion limits as a function of the $\widetilde{t}_2$ branching ratios are shown in Fig. 6.6 for representative values of the masses of $\widetilde{t}_2$ and $\widetilde{\chi}_1^0$. For $\widetilde{t}_2$ mass of 600 GeV, SUSY models with $\mathcal{B}(\widetilde{t}_2 \rightarrow Z + \widetilde{t}_1)$ above 58% are excluded. For higher top squark mass ($m_{\widetilde{t}_2} = 650$ GeV), models with $\mathcal{B}(\widetilde{t}_2 \rightarrow Z + \widetilde{t}_1)$ above 50% or

	$SR_{A,Z}$	$SR_{A,Z}$	$SR_{A,Z}$
Observed events	2	1	3
Total (post-fit) SM events	1.9 ± 0.4	2.7 ± 0.6	2.0 ± 0.3
Fit output, multi-boson	0.26 ± 0.08	0.28 ± 0.10	0.23 ± 0.05
Fit output, $t\bar{t}Z$	1.1 ± 0.3	1.4 ± 0.5	1.2 ± 0.3
tZ, tWZ	0.43 ± 0.23	0.36 ± 0.19	0.19 ± 0.10
Fake or non-prompt leptons	$0.00^{+0.30}_{-0.00}$	0.45 ± 0.19	$0.00^{+0.30}_{-0.00}$
Others	0.09 ± 0.02	0.23 ± 0.06	0.36 ± 0.06
Fit input, multi-boson	0.35	0.37	0.30
Fit input, $t\bar{t}Z$	1.2	1.5	1.4
S^{95}_{obs}	4.5	3.8	5.8
S^{95}_{exp}	$4.2^{+1.9}_{-0.4}$	$4.9^{+1.5}_{-1.1}$	$4.4^{+1.8}_{-0.5}$
σ_{vis} [fb]	0.13	0.10	0.16
$p(s = 0)$	0.42	0.93	0.23

Table 6.3: Observed and expected numbers of events in the three signal regions. The nominal predictions from MC simulation are given for the $t\bar{t}Z$ and multi-boson background. The "Others" category contains the contributions from $t\bar{t}WW$, $t\bar{t}t$, $t\bar{t}t\bar{t}$, tZ, and tWZ production. Combined statistical and systematic uncertainties are given. Signal model-independent 95% CL upper limits on the visible BSM cross-section (σ_{vis}), the visible number of signal events (S^{95}_{obs}), the number of signal events (S^{95}_{exp}) given the expected number of background events (and $\pm 1\sigma$ variations of the expected background), and the discovery p-value ($p(s = 0)$), all calculated with pseudo-experiments, are also shown for each signal region.

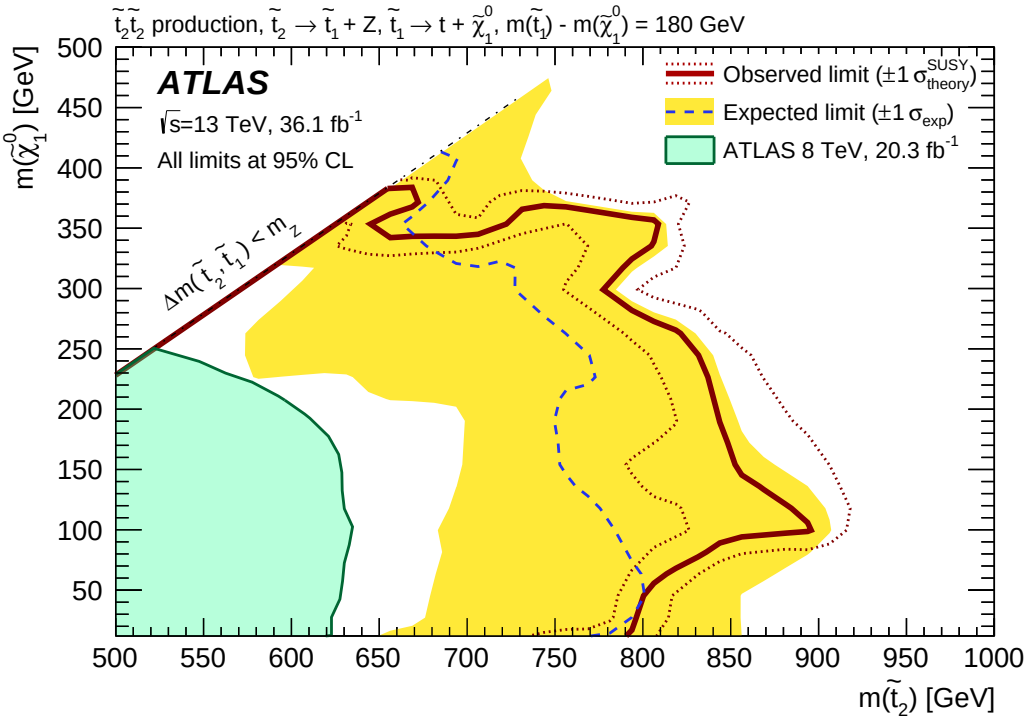

Figure 6.5: Exclusion limits at 95% CL from the analysis of 36.1 fb^{-1} of 13 TeV pp collision data on the masses of the $\widetilde{t}_2$ and $\widetilde{\chi}_1^0$, for a fixed mass splitting $m_{\widetilde{t}_1} - m_{\widetilde{\chi}_1^0} = 180$ GeV and assuming $\mathcal{B}(\widetilde{t}_2 \to \widetilde{t}_1 + Z) = 1$. The dashed line and the shaded band are the expected limit and its $\pm 1\sigma$ uncertainty, respectively. The thick solid line is the observed limit for the central value of the signal cross-section. The expected and observed limits do not include the effect of the theoretical uncertainties in the signal cross-section. The dotted lines show the effect on the observed limit when varying the signal cross-section by $\pm 1\sigma$ of the theoretical uncertainty. The shaded area in the lower-left corner shows the observed exclusion from the ATLAS $\sqrt{s} = 8$ TeV analysis.

$\mathcal{B}(\widetilde{t}_2 \to h + \widetilde{t}_1)$ above 80% are excluded. The region with large $\mathcal{B}(\widetilde{t}_2 \to t + \widetilde{\chi}_1^0)$ can be probed by searches targeting direct $\widetilde{t}_1$ pair production.

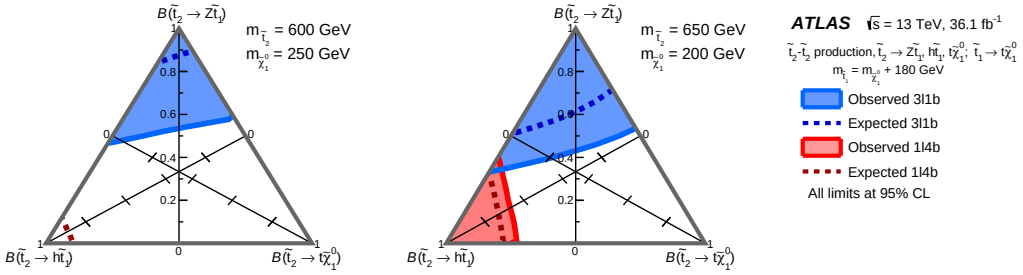

Figure 6.6: Exclusion limits at 95% CL from the analysis of 36.1 fb^{-1} of 13 TeV pp collision data as a function of the $\widetilde{t}_2$ branching ratio for $\widetilde{t}_2 \to \widetilde{t}_1 + h$ and $\widetilde{t}_2 \to \widetilde{t}_1 + Z$. The blue and red exclusion regions correspond to the h channel and the Z selections respectively. The limits are given for two different values of the $\widetilde{t}_2$ and $\widetilde{\chi}_1^0$ masses. The dashed lines are the expected limit and the solid lines are the observed limit for the central value of the signal cross-section.

6.4 The $\widetilde{t}_1$ interpretation

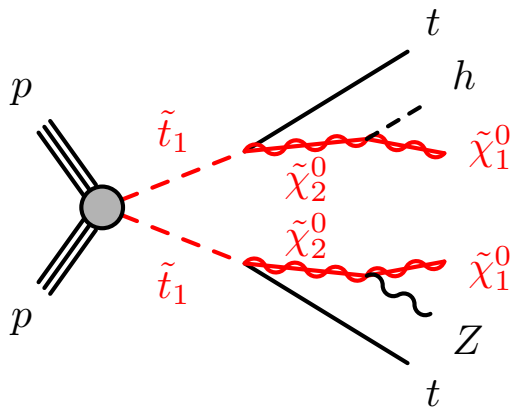

Figure 6.7: Diagram for the top squark pair production process $\widetilde{t}_1 \to t + \widetilde{\chi}_2^0$.

Top squark production with Higgs (h) or Z bosons in the decay chain can appear in production of the lighter top squark mass eigenstate ($\widetilde{t}_1$) decaying via $\widetilde{t}_1 \to t + \widetilde{\chi}_2^0$ with $\widetilde{\chi}_2^0 \to \widetilde{\chi}_1^0 + h/Z$. Again, the results are interpreted in the context of simplified models in which pair-produced $\widetilde{t}_1$ decay with 100 % branching ratio into the $\widetilde{\chi}_2^0$ and a top quark, assuming BR($\widetilde{\chi}_2^0 \to h\widetilde{\chi}_1^0$) = 0.5 and BR($\widetilde{\chi}_2^0 \to Z\widetilde{\chi}_1^0$) = 0.5. A massless LSP and a minimum mass difference between the $\widetilde{\chi}_2^0$ and $\widetilde{\chi}_1^0$ of 130 GeV, needed to have on-shell decays for the Higgs boson, are assumed in this model. As shown in Fig. 6.7, the final signature of this decay is identical with respect to the $\widetilde{t}_2$ direct production targeted by this study; simplified models featuring direct $\widetilde{t}_1$ production can be considered for a reinterpretation of the results obtained so far.

The results exclude at 95% confidence level $\widetilde{t}_2$ and $\widetilde{t}_1$ masses up to about 800 GeV, greatly extending the region of supersymmetric parameter space covered

by previous LHC searches. No specific analysis strategy have been applied for this reinterpretation, as the two SRs with best expected sensitivity from the Higgs decay and Z decay selections are statistically combined to derive the limits on this model. Fig. 7.2 shows the limits for these simplified models in the $\widetilde{t}_1 - \widetilde{\chi}_2^0$ mass plane. For a $\widetilde{\chi}_2^0$ mass above 200 GeV, $\widetilde{t}_1$ masses up to about 800 GeV are excluded at 95% CL.

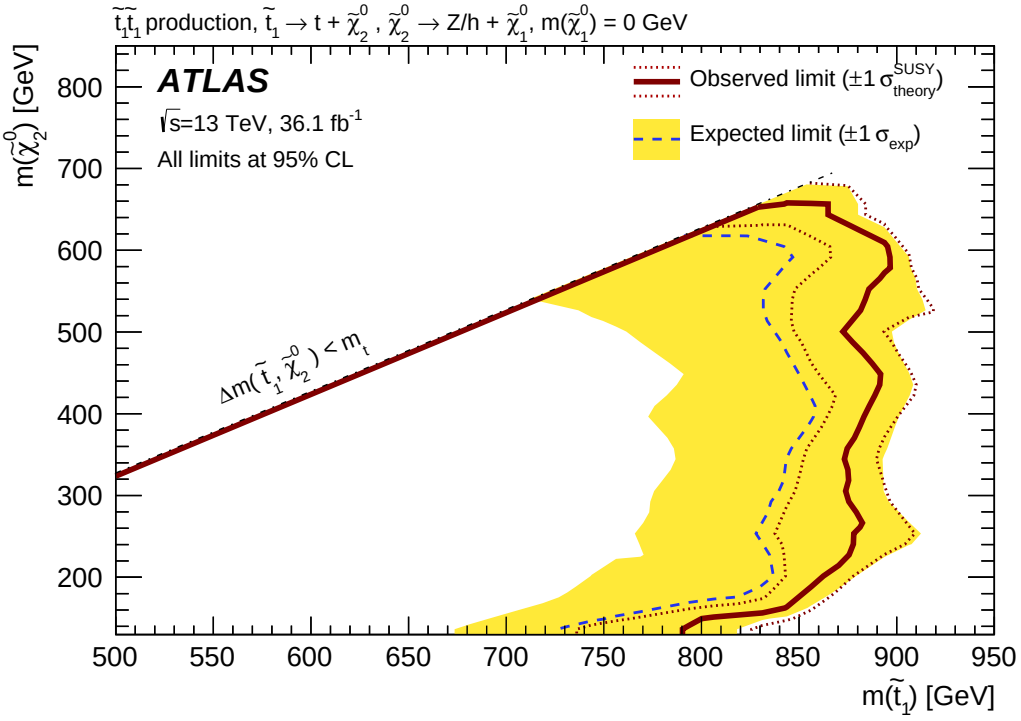

Figure 6.8: Exclusion limits at 95% CL from the analysis of 36.1 fb^{-1} of 13 TeV pp collision data on the masses of the $\widetilde{t}_1$ and $\widetilde{\chi}_2^0$, for a fixed $m_{\widetilde{\chi}_1^0} = 0$ GeV, assuming $\mathcal{B}(\widetilde{\chi}_2^0 \to \widetilde{\chi}_1^0 + h) = 0.5$ and $\mathcal{B}(\widetilde{\chi}_2^0 \to \widetilde{\chi}_1^0 + Z) = 0.5$. The dashed line and the shaded band are the expected limit and its $\pm 1\sigma$ uncertainty, respectively. The thick solid line is the observed limit for the central value of the signal cross-section. The expected and observed limits do not include the effect of the theoretical uncertainties in the signal cross-section. The dotted lines show the effect on the observed limit when varying the signal cross-section by $\pm 1\sigma$ of the theoretical uncertainty.

The limits exclude, at 95% confidence level, beyond-the-SM processes with visible cross-sections above 0.21 fb for the selections optimized for the $\widetilde{t}_2 \to \widetilde{t}_1 + h$ decay, and above 0.11 fb for the selections optimized for the $\widetilde{t}_2 \to \widetilde{t}_1 + Z$ decay.

Chapter 7

Conclusions

In this thesis I reported my PhD thesis work during a Joint-Supervision PhD program at the Universities of Bern (UniBe, LHEP - Laboratory for High Energy Physics and AEC - Albert Einstein Center for Fundamental Physics) and Bologna (UniBo and INFN - Istituto Nazionale di Fisica Nucleare) in the framework on the ATLAS experiment at the CERN LHC.

My effort focused on the search of the production of supersymmetric (SUSY) particles in proton-proton collisions at the LHC, using data acquired by the ATLAS detector. The small production cross-section of these processes requires both a huge quantity of data to be analysed and a way to efficiently discriminate the possible SUSY signal using kinematic variables of the decay products. In order to expand the data statistics, LHC increased the beam luminosity with respect to the first data taking period. This evolution led to the necessity of an upgrade of the ATLAS Pixel Detector, as the expanded data throughput caused de-synchronization issues and high-bandwidth occupancy with subsequent data loss. In addition, radiation damages occurred to the pixel subsystem during Run-I, leading to degraded b-tagging capabilities and thus requiring the installation of a new pixel detector layer, the IBL. When I started my activities at the end of 2014, the IBL already proved to be a reliable solution for data-taking and an effort to upgrade the pre-existing pixel detector layers, namely Layer-1 and Layer-2, has been set up.

I directly worked on the renewal of the Layer-1 and Layer-2 read-out system by testing a custom Opto-Electrical RX Plugin, designed and produced by LHEP, which interfaces the optical fibres coming from the Front End electronics to the Read-Out boards. This operation required the design of two custom testing boards: the first one, for which I wrote the entirety of the RX-INO suite software, was used to check the electrical connectivity and insulation of the RX Plugin PCB; the second one, known as GoNoGo board, served as a functionality test of the optical capabilities of each completed RX. I personally designed the GoNoGo board, tested it and created the software control suite GoNoGoIno.

In addition to this, I also worked on the commissioning of the read-out board of this system, called Read-Out Driver, designed and built by the ATLAS

Bologna Electronics Laboratories. I personally tested all the Read-Out Drive and Back-Of-Crate boards used for Layer-2 and developed software for the data-taking system. The ROD and BOC boards are currently operating in the ATLAS pixel detector, outperforming the previous versions and showing great resilience with respect to de-synchronization issues and an increased data bandwidth. As future upgrades for the Pixel Detector read-out are foreseen for the near future (like the *Inner Tracker* detector), my work will continue towards the next generation of pixel detectors read-out system, already in advanced stage of development.

The insertion of the IBL in conjunction with the renewed layers led to an improvement up to a factor of 4 in the light-jets rejection for b-tagging, thus improving the reconstruction of b-quarks. Thanks also to these improvements, it proved to be possible to perform a search for a third generation supersymmetric particle, the stop squark. Previous searches excluded masses for the stop lightest mass eigenstate $\widetilde{t}_1$ up to 700 GeV, but failed to homogeneously cover the $\widetilde{t}_1 - \widetilde{\chi}_1^0$ mass space, due to a severe lack of sensibility in the compressed region where where $m_{\widetilde{t}_1} - m_{\widetilde{\chi}_1^0} = m_t$. In this region, the top quark from the stop decay is produced at rest, leaving little E_{T}^{miss} and making it difficult to distinguish its signature from the SM $t\bar{t}$ production.
My work focused on covering this kinematic region; this has been done by searching for $\widetilde{t}_1$ in the decay chain of the heavier eigenstate $\widetilde{t}_2$, so that the boost of the produced neutralinos could give rise to some E_{T}^{miss}. These search adopted the simplified model approach, assuming that the heavier stop $\widetilde{t}_2$ decays to the lighter stop $\widetilde{t}_1$ plus a Higgs boson ($\widetilde{t}_2 \rightarrow \widetilde{t}_1 + h$) with a 100% branching fraction or plus a Z boson ($\widetilde{t}_2 \rightarrow \widetilde{t}_1 + Z$) with a 100% branching fraction. In this simplified model, only $\widetilde{t}_1$, $\widetilde{t}_2$, $\widetilde{\chi}_1^0$ and $\widetilde{\chi}_2^0$ were considered as active SUSY particles, as the mass of the other SUSY states is expected to be too high to be probed by the LHC. A set of different models is taken into account, each targeting a different mass splitting between the $\widetilde{t}_2$ and the $\widetilde{t}_1$, creating different kinematics of the decay products.
I defined multiple Signal Regions in order to increase the statistical significance for models with different $\widetilde{t}_2 - \widetilde{t}_1$ mass splitting. For each of these Signal Regions, a dedicated statistically independent Control Region has been set in place in order to normalize to data the expected yield of the main background of the analysis, the $t\bar{t}$ SM production. The method proved to be successful, and good agreement is found between the yield of observed events and the SM predictions after the Signal Region selections are applied.

Model independent limits (Fig. 7.1) allows to reinterpret the results in generic models predicting similar final states in association with invisible particles. Assuming 100% branching ratio into $\widetilde{t}_1$ and a h boson, $\widetilde{t}_2$ masses up to 880 GeV are excluded at 95% CL for a $\widetilde{\chi}_1^0$ of about 50 GeV, and $\widetilde{\chi}_1^0$ masses up to 260 GeV are excluded for $\widetilde{t}_2$ masses between 650 and 710 GeV. These results extend the previous limits on the $\widetilde{t}_2$ mass from ATLAS $\sqrt{s} = 8$ TeV analyses by up to 250 GeV depending on the $\widetilde{\chi}_1^0$ mass.

In analogy with the results of the search involving a decay with the Higgs bo-

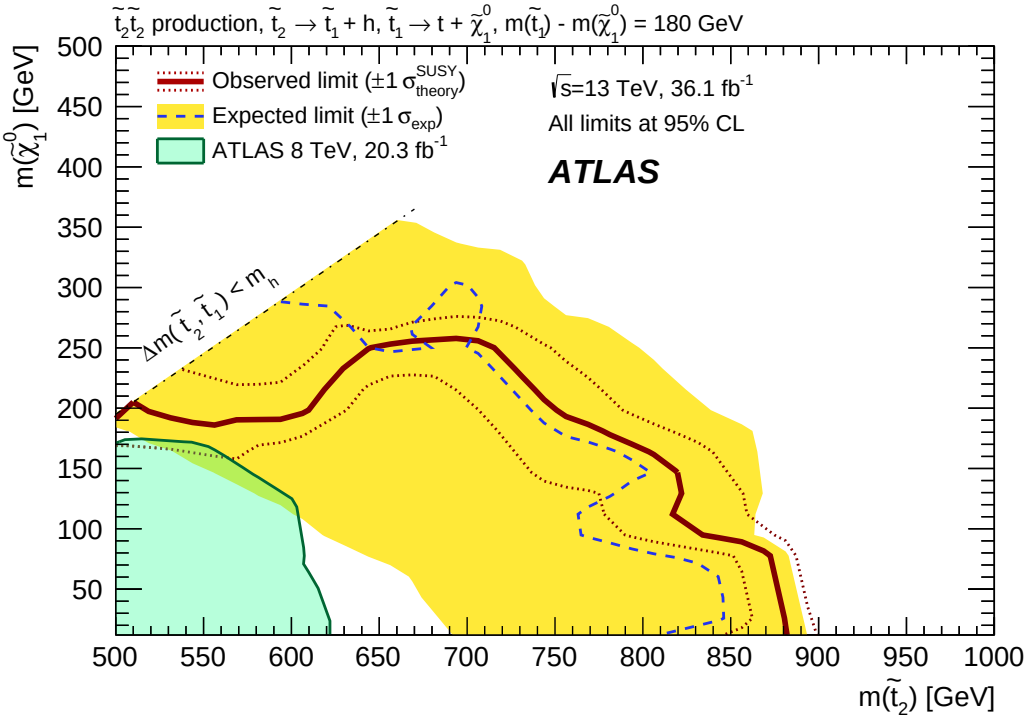

Figure 7.1: Exclusion limits at 95% CL from the analysis of 36.1 fb^{-1} of 13 TeV pp collision data on the masses of the $\widetilde{t}_2$ and $\widetilde{\chi}_1^0$, for a fixed mass splitting $m_{\widetilde{t}_1} - m_{\widetilde{\chi}_1^0} = 180$ GeV, with the Higgs boson in the decay chain.

son, limits for simplified models, in which pair-produced $\widetilde{t}_2$ decay with 100% branching ratio into the $\widetilde{t}_1$ and a Z boson, with $\widetilde{t}_1 \to t\ \widetilde{\chi}_1^0$, in the $\widetilde{t}_2 - \widetilde{\chi}_1^0$ mass plane have been computed.In this case, $\widetilde{t}_2$ masses up to 800 GeV are excluded at 95% CL for a $\widetilde{\chi}_1^0$ of about 50 GeV and $\widetilde{\chi}_1^0$ masses up to 350 GeV are excluded for $\widetilde{t}_2$ masses below 650 GeV. The limits exclude, at 95% confidence level, beyond-the-SM processes with visible cross-sections above 0.21 fb for the selections optimized for the $\widetilde{t}_2 \to \widetilde{t}_1 + h$ decay, and above 0.11 fb for the selections optimized for the $\widetilde{t}_2 \to \widetilde{t}_1 + Z$ decay. Limits for the $\widetilde{t}_2$

Results are also interpreted in the context of simplified models characterised by the decay chain $\widetilde{t}_1 \to \widetilde{\chi}_2^0 + t$ with $\widetilde{\chi}_2^0 \to \widetilde{\chi}_1^0 + h/Z$, or $\widetilde{t}_2 \to \widetilde{t}_1 + h/Z$ with $\widetilde{t}_1 \to t + \widetilde{\chi}_1^0$. The results exclude at 95% confidence level $\widetilde{t}_2$ and $\widetilde{t}_1$ masses up to about 800 GeV, greatly extending the region of supersymmetric parameter space covered by previous LHC searches. No specific analysis strategies have been applied for this reinterpretation, as the two SRs with best expected sensitivity from the Higgs decay and Z decay selections are statistically combined to derive the limits on this model.

Fig. 7.2 shows the limits on simplified models in which pair-produced $\widetilde{t}_1$ decay with 100 % branching ratio into the $\widetilde{\chi}_2^0$ and a top quark, assuming $\mathrm{BR}(\widetilde{\chi}_2^0 \to h\widetilde{\chi}_1^0) = 0.5$. A massless LSP and a minimum mass difference between the $\widetilde{\chi}_2^0$ and $\widetilde{\chi}_1^0$ of 130 GeV, needed to have on-shell decays for the Higgs boson, are assumed in this model. Limits are presented in the $\widetilde{t}_1 - \widetilde{\chi}_2^0$ mass

plane. For a $\widetilde{\chi}_2^0$ mass above 200 GeV, $\widetilde{t}_1$ masses up to about 800 GeV are excluded at 95% CL.

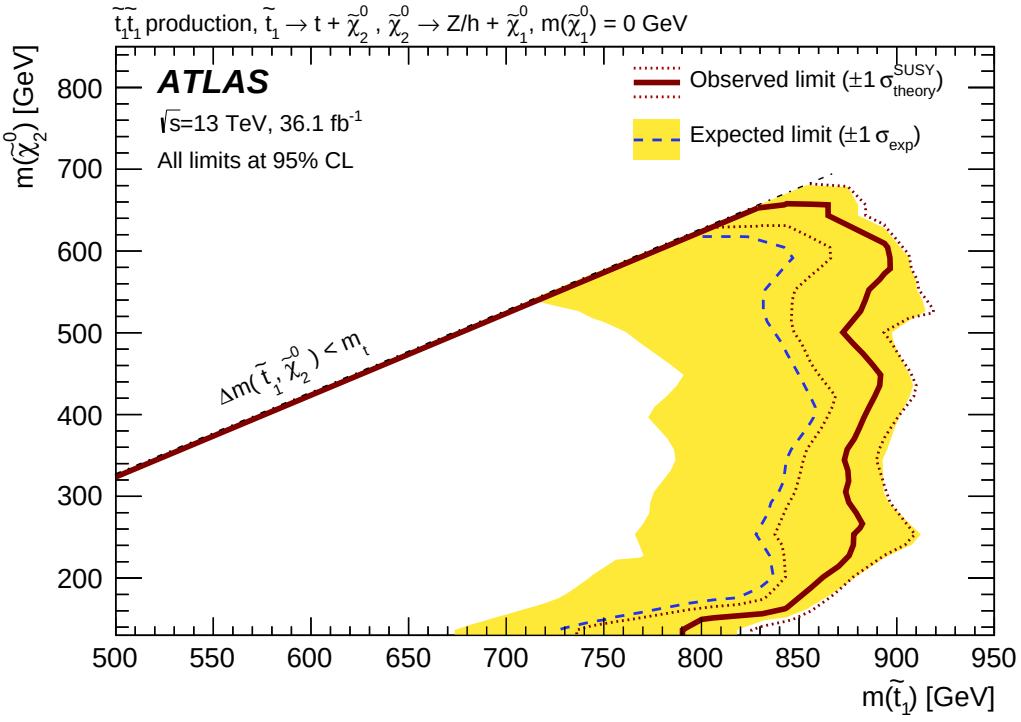

Figure 7.2: Exclusion limits at 95% CL from the analysis of 36.1 fb^{-1} of 13 TeV pp collision data on the masses of the $\widetilde{t}_1$ and $\widetilde{\chi}_2^0$.

Thanks to the results presented, I have been able to cover the compressed region in the $\widetilde{t}_1 - \widetilde{\chi}_1^0$ mass plane, as shown in Fig. 7.3; masses for the $\widetilde{t}_1$ are excluded up to almost 1 TeV. In many SUSY models, the lightest $\widetilde{t}_1$ is expected to be not too much heavier than 1 TeV, due to the amount of fine-tuning necessary for the cancellation of its radiative contributions to the Higgs mass. This makes the limits sets by this work relevant in setting strong constraints on the increasingly thinner possible mass spectrum of a natural SUSY theory.

7.1 Future developments

As we approach this limit value for $m_{\widetilde{t}_1}$, we should start considering how to proceed next; the decay chain of the stop squark in our simplified models does not take in account the fact that there could be at least one sbottom mass eigenstate lighter than the second stop. In this case, the patterns of the decay $\widetilde{t}_2 \to \widetilde{t}_1 + h/Z$ are usually more complicated than those I assumed. Stop decays to sbottom states are expected to have large branching ratios, as long as they are open. The decay chains can be even more complex if there are intermediate states of additional charginos and neutralinos in the decays. It is also worth remembering that the mixing of the right-handed

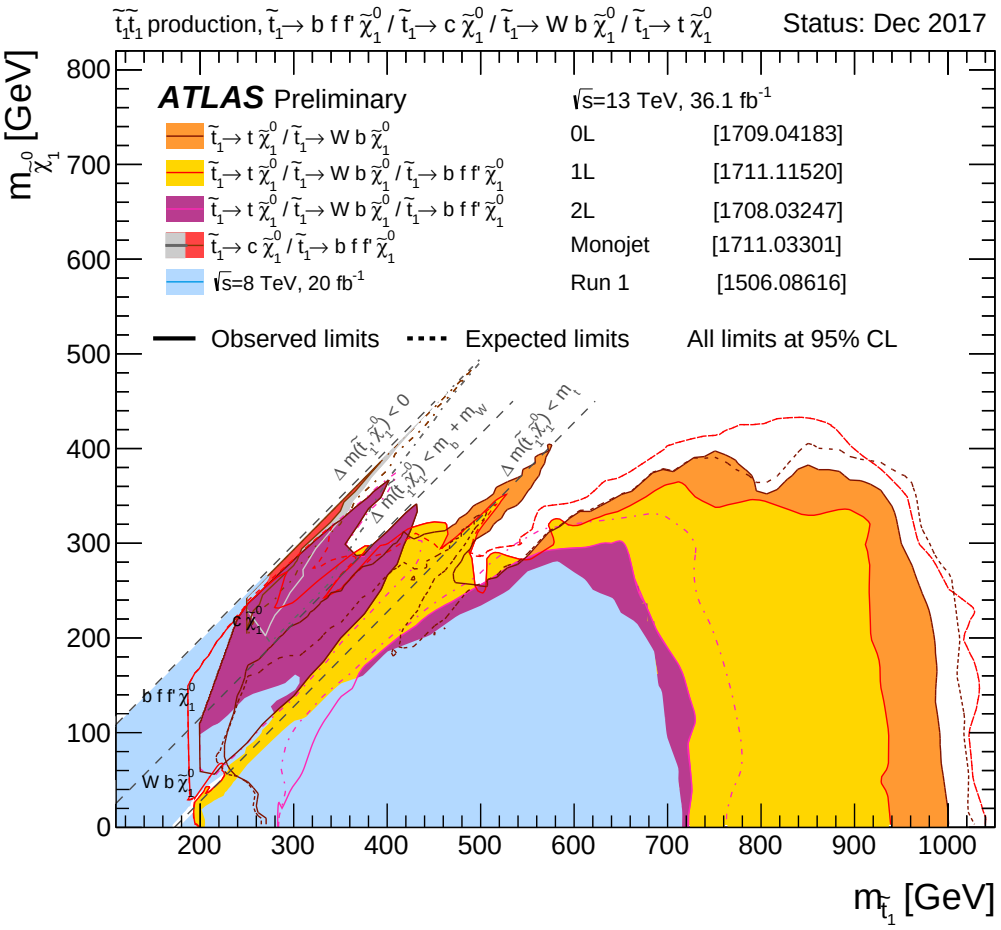

Figure 7.3: Summary of the dedicated ATLAS searches for top squark (stop) pair production based on 3.2 to 36 fb^{-1} of pp collision data taken at $\sqrt{s} = 13$ TeV. Exclusion limits at 95% CL are shown in the $\widetilde{t}_1 - \widetilde{\chi}_1^0$ mass plane. The dashed and solid lines show the expected and observed limits, respectively, including all uncertainties except the theoretical signal cross section uncertainty (PDF and scale). Four decay modes are considered separately with 100% BR: $\widetilde{t}_1 \to t + \widetilde{\chi}_1^0$, $\widetilde{t}_1 \to W + b + \widetilde{\chi}_1^0$ (3-body decay allowed for $m_{\widetilde{t}_1} < m_t + m_{\widetilde{\chi}_1^0}$), $\widetilde{t}_1 \to c + \widetilde{\chi}_1^0$ and $\widetilde{t}_1 \to f + f' + \widetilde{\chi}_1^0$ (4-body decay), with the latter two decay modes are superimposed.

and left-handed stops in the two mass eigenstates previously introduced is bound to the framework of MSSMs and non minimal extensions of the SM could result in heavily different decay chains and states. A third data-taking period, Run-III, is expected to start in 2019 and collect a total of $\approx$ 300 fb^{-1} and is expected to cover stop masses up to 1 TeV for MSSM extensions, strenghtening the exclusion limits presented in this work. While the increase of statistics is expected to improve the significance of the search, the lack of significant upgrades in the detector itself will render impossibile an expansion of the excluded region by a factor comparable with the one observed between Run-I and Run-II. Even if a projection of these limits for Run-III and beyond is not feasible without dedicated simulations, it is possible to predict that with an higher integrated luminosity will be possible to re-optimize the search with

tighter selections on the main kinematic variables, such as the E_{T}^{miss}. With the near-future upgrade of the LHC to the HL-LHC phase, stop masses up to 1.5 TeV are expected to be probed during Run-4, giving a definitive answer on the existence of natural minimal supersymmetrics extensions of the Standard Model.

Part III

Appendix

Appendix A

Selection Efficiency and Acceptance

A.1 Efficiency

The selection efficiency is defined as the ratio between the reconstructed events by the ATLAS detector and the total expected events by MonteCarlo simulations, and is a measure of the quality of the detector reconstruction in different kinematic regions and under different selections.

$$Selection\ Efficiency = \frac{yield_{MC}}{yield_{SR}} * 100\% \tag{A.1}$$

Fig. A.1 shows the efficiency for the entire signal model grid after $SR_A^{1\ell 4b}$

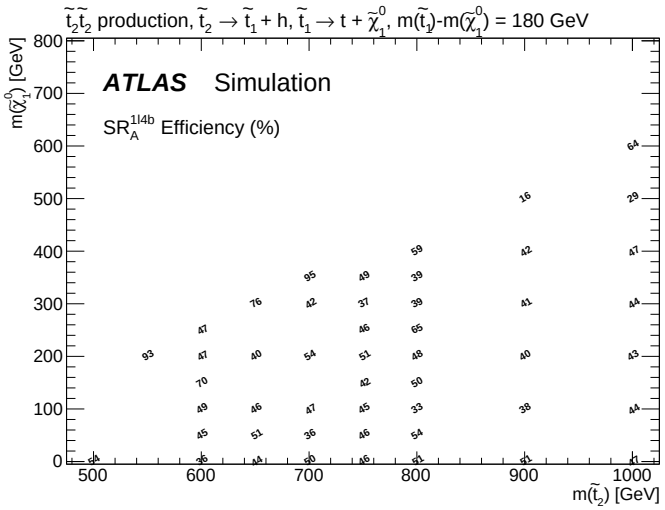

Figure A.1: Selection efficiency, defined as the ratio between the reconstructed events by the ATLAS detector and the total expected events by MonteCarlo simulations in events of the $\widetilde{t}_2 - \widetilde{\chi}_1^0$ mass models passing $SR_A^{1\ell 4b}$ selections.

selection are applied. Fig. A.2 shows the efficiency for the entire signal model grid after $SR_B^{1\ell 4b}$ selection are applied, while Fig. A.3 shows the efficiency for the entire signal model grid after $SR_C^{1\ell 4b}$ selection are applied.

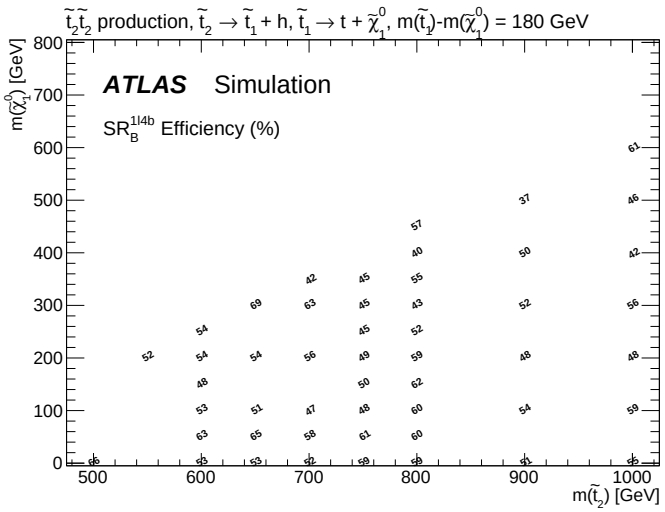

Figure A.2: Selection efficiency, defined as the ratio between the reconstructed events by the ATLAS detector and the total expected events by MonteCarlo simulations in events of the $\widetilde{t}_2 - \widetilde{\chi}_1^0$ mass models passing $SR_B^{1\ell 4b}$ selections.

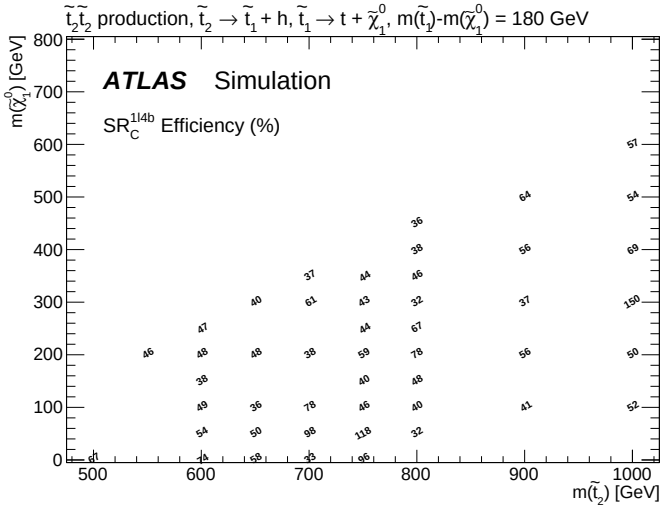

Figure A.3: Selection efficiency, defined as the ratio between the reconstructed events by the ATLAS detector and the total expected events by MonteCarlo simulations in events of the $\widetilde{t}_2 - \widetilde{\chi}_1^0$ mass models passing $SR_C^{1\ell 4b}$ selections.

A.2 Acceptance

The selection acceptance is defined as the ratio between the reconstructed events passing Signal Region requirements and the total reconstructed events for each mass model of the $\widetilde{t}_2 - \widetilde{\chi}_1^0$ mass plane.

$$Selection\ Acceptance = \frac{yield_{SR}}{yield_{Reco}} * 100\% \tag{A.2}$$

Fig. A.4 shows the efficiency for the entire signal model grid after $SR_A^{1\ell 4b}$ selection are applied. Fig. A.5 shows the efficiency for the entire signal model grid after $SR_B^{1\ell 4b}$ selection are applied, while Fig. A.6 shows the efficiency for

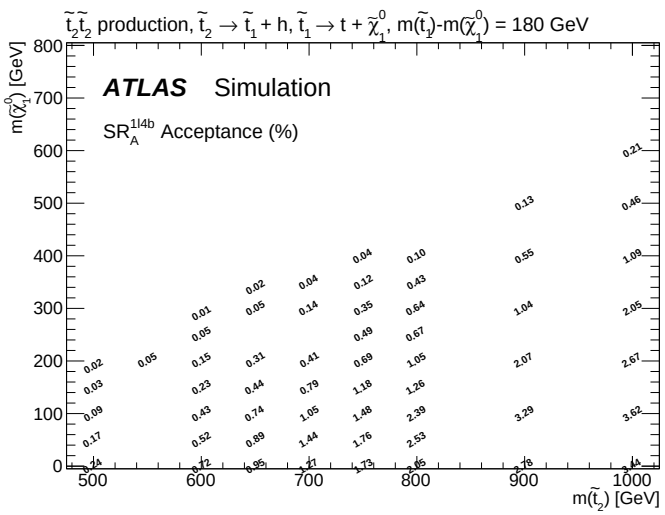

Figure A.4: Selection acceptance, defined as the ratio between the reconstructed events passing Signal Region requirements and the total reconstructed events for each mass model in events of the $\widetilde{t}_2 - \widetilde{\chi}_1^0$ mass models passing $SR_A^{1\ell 4b}$ selections.

the entire signal model grid after $SR_C^{1\ell 4b}$ selection are applied.

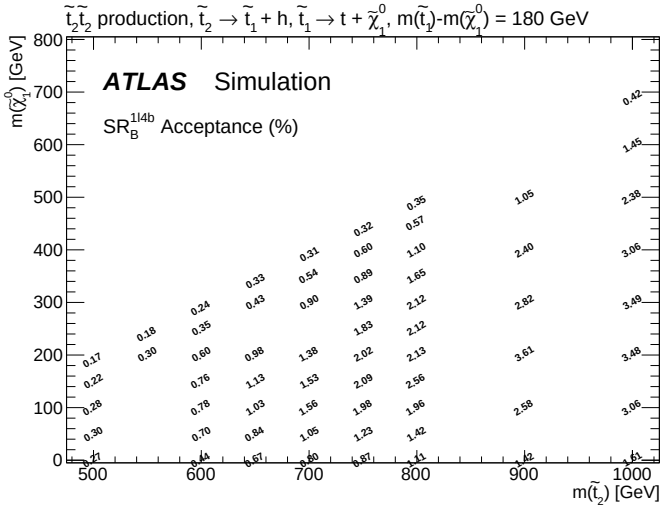

Figure A.5: Selection acceptance, defined as the ratio between the reconstructed events passing Signal Region requirements and the total reconstructed events for each mass model in events of the $\widetilde{t}_2 - \widetilde{\chi}_1^0$ mass models passing $SR_B^{1\ell 4b}$ selections.

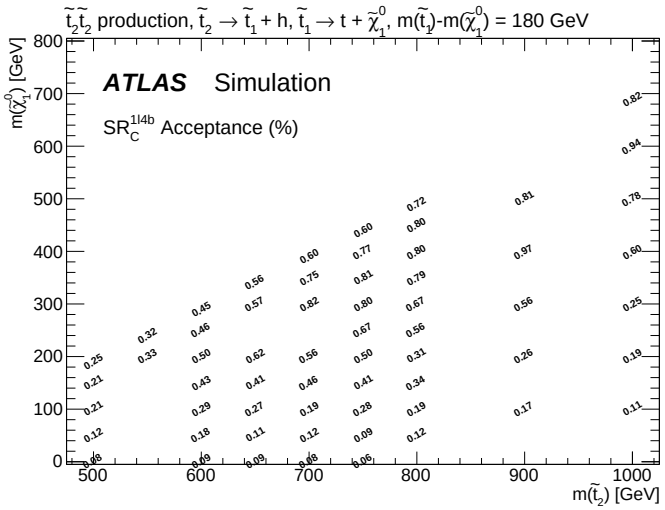

Figure A.6: Selection acceptance, defined as the ratio between the reconstructed events passing Signal Region requirements and the total reconstructed events for each mass model in events of the $\widetilde{t}_2 - \widetilde{\chi}_1^0$ mass models passing $SR_C^{1\ell 4b}$ selections.

Appendix B

Hypothesis testing

This appendix reports the basic concepts of the statistical treatment of data. The focus will be on a precise definition and notation of the key components for setting exclusion limits on new physics processes.
The level of agreement of the observed data with a given hypothesis H is quantified by computing the probability ($p-value$) that, assumed the hypothesis H to be correct, obtained data can be found with equal or greater incompatibility with the predictions of H:

$$p - value = P(q > q^{obs}|H) \tag{B.1}$$

where q^{obs} is the value of the test statistic obtained from comparing the observed data with a hypothesis H.
The hypothesis is regarded as excluded if its p-value is observed below a specified threshold given by the size of the test $\alpha \in [0, 1]$. It is possible to define the $Z - value$ corresponding to a given p-value as the number of standard deviation Z at which a Gaussian random variable of zero mean would give a one-sided tail area equal to the p-value.
The particle physics community has tended to regard rejection of the background hypothesis with a significance of at least Z = 5 as an appropriate level to constitute a discovery. This corresponds to p-value = 2.8 $\times 10^{-7}$. For purposes of excluding a signal hypothesis, a threshold p-value of $\alpha = 0.05$, is often used, which corresponds to Z = 1.64.

B.1 Profile likelihood-ratio

In addition to parameters of interest such as rate of the signal process (i.e., cross section), the predictions for both the signal and background yields, prior to the scrutiny of the observed data entering the statistical analysis, are subject to multiple uncertainties that are handled by introducing nuisance parameters, denoted by $\overrightarrow{\theta}$.
Therefore, the signal and background expectation become functions of these parameters: $S = S(\overrightarrow{\theta})$ and $B = B(\overrightarrow{\theta})$. In order to handle the nuissance parameters in the likelihoods for testing the compatibility of the data with the background-only and the signal+background hypotheses, the LHC has chosen

the profile likelihood-ratio test statistic, defined as:

$$\widetilde{q}_\mu = -2log\widetilde{\lambda}(\mu) \equiv -2log\frac{\mathcal{L}(\overrightarrow{x}|\mu,\widehat{\theta}_\mu)}{\mathcal{L}(\overrightarrow{x}|\widehat{\mu},\widehat{\theta}_\mu)}, \quad with\ the\ requirement\ 0 \leq \widehat{\mu} \leq \mu \tag{B.2}$$

Here, $\widehat{\theta}_\mu$ refers to the conditional maximum likelihood estimators of θ, given the signal strength parameter μ, and $\overrightarrow{x}$ may refer to the actual experimental observation or pseudo-data events. The pair of parameters $\widehat{\mu}$ and $\widehat{\theta}$ gives the global maximum of the likelihood. The lower constraint $0 \leq \widehat{\mu}$ is imposed by physics, since signal rate is defined positive. On the other hand, the upper constraint $\widehat{\mu} \leq \mu$ is added by hand in order to guarantee a one-sided confidence interval.11 The presence of the nuisance parameters broadens the profile likelihood as a function of μ relative to what one would have if their values were fixed. This reflects the loss of information about μ due to the systematic uncertainties.

B.2 Limit setting

Having defined the test statistic, one constructs probability density functions of $\widetilde{q}_\mu$ under the signal+background hypothesis assuming a signal with strength m. The test-statistic $\widetilde{q}_\mu$ can be constructed to decrease monotonically for decreasing signal-like experiments so that the confidence in the signal+background hypothesis is given by the probability that the test-statistic is bigger than or equal to the value observed in the experiment, $\widetilde{q}_\mu^{obs}$ for a given tested μ.
This probability is referred to as CL_{s+b}:

$$p_\mu = CL_{s+b} = P(\widetilde{q}_\mu \geq \widetilde{q}_\mu^{obs}|\mu S + B) = \int_{\widetilde{q}_\mu^{obs}}^{\infty} f(\widetilde{q}_\mu^{obs}|\mu,\widehat{\theta}_\mu^{obs})dq_\mu \tag{B.3}$$

Similarly, the confidence in the background only hypothesis, referred to as CL_b, can be defined as:

$$1 - p_b = CL_b = P(\widetilde{q}_\mu \geq \widetilde{q}_\mu^{obs}|B) = \int_{\widetilde{q}_\mu^{obs}}^{\infty} f(\widetilde{q}_\mu^{obs}|0,\widehat{\theta}_\mu^{obs})dq_\mu \tag{B.4}$$

Hence, values of CL_b very close to 1 indicate poor compatibility with the background only hypothesis.
The CL_s method is defined as the following ratio:

$$CL_s \equiv CL_{s+b}CL_b = p_\mu 1 - p_b \tag{B.5}$$

If, for $\mu = 1, CL_s \leq 0.05$ the signal hypothesis is excluded with 95% CL_s confidence level.
The CL_s method is introduced to reduce the exclusion of region where the sensibility is very small. In particular the CL_{s+b} method excludes regions where $p_\mu < 0.05$ also when the expected number of signal events is much less than that of background. In the modified approach, using the CLs, the p-value is effectively penalized by dividing by $1 - p_b$. If the two distributions $f(\widetilde{q}_\mu|\mu = 0, \widehat{\theta}_0^{obs})$ and $f(\widetilde{q}_\mu|\mu, \widehat{\theta}_\mu^{obs})$ are widely separated, then $1 - p_b$ is only

slightly less than unity, the penalty is slight, and thus exclusion based in CL_s is similar to that obtained from the usual p-value p_{s+b}. If, however, one has little sensitivity to the signal model, then the two distributions are close together, $1 - p_b$ becomes small, and thus the p-value of $s + b$ is penalized (increased) more. In this way one is prevented from excluding signal models in cases of low sensitivity.
From the definition B.5, one can see that CL_s is always greater than the p-value p_{s+b}. Thus the models excluded by requiring $CL_s < 0.05$ are a subset of those excluded by the usual criterion $p_{s+b} < 0.05$, and the upper limit from CL_s is therefore higher (weaker). In this sense the CL_s procedure is conservative.

Appendix C

Acronyms

ATLAS - A Toroidal LHC ApparatuS
ASIC - Application Specific Integrated Circuit

BCF - BOC Control FPGA
BDT - Boosted Decision Tree
BERT - Bit Error Rate Test
BMF - BOC Main FPGA
BOC - Back-Of-Crate
BR - Branching Ratio
BSM - Beyond the Standard Model

CERN - Conseil Européen pour la Recherche Nucléaire
CKM - Cabibbo-Kobayashi-Maskawa (matrix)
CR - Control Region
CSC - Cathode Strip Chambers

DSP - Digital Signal Processing

ECAL - Electromagnetic Calorimeter
EW - Electroweak
EWSB - Electro-Weak Symmetry Breaking
EYETS - Extended Year-End Technical Stop

FCAL - (LAr) Forward Calorimeter
FPGA - Field Programmable Gate Array

GUT - Grand Unified Theory

HCAL - Hadronic Calorimeter
HEC - Hadronic End-Caps Calorimeter
HLT - High-Level Trigger
HTC - Hadronic Tile Calorimeter

IBL - Insertable B-Layer
ID - Inner Detector

ID(electrons) - Electron Identification
IP - Interaction Point
ISR - Initial State Radiation

JES - Jet Energy Scale
JER - Jet Energy Resolution
JTAG - Joint Test Action Group
JVT - Jet Vertex Tagging

LAr - Liquid Argon (calorimeter)
LEP - Large Electron Positron Collider
LH - Likelihood
LHC - Large Hadron Collider
LO - Leading Order
LS - Long Shutdown
LSP - Lightest Supersymmetric Particle
LVDS - Low Voltage Differential Signal

MC - MonteCarlo (simulation)
MCC - Module Controller Chip
MDT - Monitored Drift Tubes
MSSM - Minimal Supersymmetric Standard Model

NLL - Next-to-Leading-Logarithmic
NLO - Next-to-Leading Order
NN - Neural Network
NNLL - Next-to-Next-Leading-Logarithmic
NNLO - Next-to-Next-Leading Order
NZR - Non Return to Zero

OR - Overlap Removal

PCB - Printed Circuit Board
PD - Pixel Detector
PDF - Parton Distribution Function
PS - Proton Synchrotron
PSB - Proton Synchrotron Booster
PV - Primary Vertex

QCD - Quantum Chromodynamics

RF - Radio Frequency
ROD - Read-Out Driver
RPC - Resistive Plate Chambers

SCT - Semi-Conductor Tracker
SF - Scale Factor
SM - Standard Model

SPS - Super Proton Synchrotron
SR - Signal Region
SSRAM - Synchronous Static Random Access Memory
SUSY - Supersymmetry
SV - Secondary Vertex

TDAQ - Trigger and Data Acquisition
TGC - This Gas Chambers
TIA - Transimpedance Amplifier
TRT - Transition Radiation Tracker
TST - Track Soft Term

UV - Ultra-Violet

VEV - Vacuum Expectation Value
VME - Versa Module Europa
VR - Validation Region

List of Figures

List of Tables

Bibliography

1. Evans, L. & Bryant, P. LHC Machine. *JINST* **3,** S08001 (2008).
2. Aad, G. *et al.* The ATLAS Experiment at the CERN Large Hadron Collider. *JINST* **3,** S08003 (2008).
3. Rocca, P. L. & Riggi, F. The upgrade programme of the major experiments at the Large Hadron Collider. *Journal of Physics: Conference Series* **515,** 012012 (2014).
4. Cakir, A. Searches for Beyond Standard Model Physics at the LHC: Run1 Summary and Run2 Prospects. *PoS* **FPCP2015,** 024 (2015).
5. Balbi, G. *et al.* ATLAS Pixel Detector ROD card from IBL towards Layers 2 and 1. *Journal of Instrumentation* **11,** C01021 (2016).
6. Wensing, M. Testing and firmware development for the ATLAS IBL BOC prototype. *Journal of Instrumentation* **7,** C12027 (2012).
7. Balbi, G *et al.* "The Read-Out Driver" ROD card for the Insertable B-layer (IBL) detector of the ATLAS experiment: commissioning and upgrade studies for the Pixel Layers 1 and 2. *Journal of Instrumentation* **9,** C01044 (2014).
8. Gabrielli, A, Alfonsi, F, D'Amen, G & Giangiacomi, N. *Commissioning of ROD boards for the entire ATLAS Pixel Detector* in *PoS(TWEPP17) (yet to be published)* (2017).
9. *Search for squarks and gluinos in final states with jets and missing transverse momentum using 36* fb^{-1} *of* $\sqrt{s}$ *= 13 TeV pp collision data with the ATLAS detector* tech. rep. ATLAS-CONF-2017-022 (CERN, Geneva, 2017). `https://cds.cern.ch/record/2258145`.
10. collaboration, T. A. Observation of a new particle in the search for the Standard Model Higgs boson with the ATLAS detector at the LHC. *Phys. Lett.* **B716,** 1–29 (2012).
11. collaboration, T. C. Observation of a new boson at a mass of 125 GeV with the CMS experiment at the LHC. *Phys. Lett.* **B716,** 30–61 (2012).
12. Martin, S. P. A Supersymmetry primer. [Adv. Ser. Direct. High Energy Phys.18,1(1998)]. doi:`10.1142/9789812839657_0001, 10.1142/9789814307505_0001`. arXiv: `hep-ph/9709356 [hep-ph]` (1997).
13. Baer, H., Barger, V., Nagata, N. & Savoy, M. Phenomenological profile of top squarks from natural supersymmetry at the LHC. *Phys. Rev.* **D95,** 055012 (2017).

14. Brust, C., Katz, A., Lawrence, S. & Sundrum, R. SUSY, the Third Generation and the LHC. *JHEP* **03,** 103 (2012).

15. Glashow, S. L. Partial Symmetries of Weak Interactions. *Nucl. Phys.* **22,** 579–588 (1961).

16. Weinberg, S. A Model of Leptons. *Phys. Rev. Lett.* **19,** 1264–1266 (21 1967).

17. Et al., A. S. Elementary Particle Physics: Relativistic Groups and Analyticity. *In: N. Svartholm, Ed., Eighth Nobel Symposium* (1968).

18. Allanach, B. C. *Beyond the Standard Model Lectures for the 2016 European School of High-Energy Physics* PhD thesis (Cambridge U., DAMTP, 2016). arXiv: 1609.02015 [hep-ph]. https://inspirehep.net/record/1485569/files/arXiv:1609.02015.pdf.

19. Wulzer, A. BSM Lessons from the SM Higgs. *PoS* **EPS-HEP2015,** 005 (2015).

20. Fermi, E. An attempt to a β rays theory. *Il Nuovo Cimento,* 1–20 (1934).

21. Aad, G. *et al.* ATLAS Run 1 searches for direct pair production of third-generation squarks at the Large Hadron Collider. *Eur. Phys. J.* **C75.** [Erratum: Eur. Phys. J.C76,no.3,153(2016)], 510 (2015).

22. Cheng, H.-C., Li, L. & Qin, Q. Second Stop and Sbottom Searches with a Stealth Stop. *JHEP* **11,** 181 (2016).

23. Boehm, C., Djouadi, A. & Mambrini, Y. Decays of the lightest top squark. *Phys. Rev.* **D61,** 095006 (2000).

24. Alwall, J. *et al.* The automated computation of tree-level and next-to-leading order differential cross sections, and their matching to parton shower simulations. *JHEP* **07,** 079 (2014).

25. Beenakker, W., Hopker, R., Spira, M. & Zerwas, P. M. Squark and gluino production at hadron colliders. *Nucl. Phys.* **B492,** 51–103 (1997).

26. Kulesza, A. & Motyka, L. Threshold resummation for squark-antisquark and gluino-pair production at the LHC. *Phys. Rev. Lett.* **102,** 111802 (2009).

27. Kulesza, A. & Motyka, L. Soft gluon resummation for the production of gluino-gluino and squark-antisquark pairs at the LHC. *Phys. Rev.* **D80,** 095004 (2009).

28. Beenakker, W. *et al.* Soft-gluon resummation for squark and gluino hadroproduction. *JHEP* **12,** 041 (2009).

29. Beenakker, W. *et al.* Squark and Gluino Hadroproduction. *Int. J. Mod. Phys.* **A26,** 2637–2664 (2011).

30. Lai, H.-L. *et al.* New parton distributions for collider physics. *Phys. Rev.* **D82,** 074024 (2010).

31. *ATLAS Run 1 Pythia8 tunes* tech. rep. ATL-PHYS-PUB-2014-021 (CERN, Geneva, Nov. 2014). https://cds.cern.ch/record/1966419.

32. Gleisberg, T. *et al.* Event generation with SHERPA 1.1. *JHEP* **02,** 007 (2009).

33. Catani, S., Cieri, L., Ferrera, G., de Florian, D. & Grazzini, M. Vector boson production at hadron colliders: a fully exclusive QCD calculation at NNLO. *Phys. Rev. Lett.* **103,** 082001 (2009).

34. Alioli, S., Nason, P., Oleari, C. & Re, E. A general framework for implementing NLO calculations in shower Monte Carlo programs: the POWHEG BOX. *JHEP* **06,** 043 (2010).

35. Sjostrand, T., Mrenna, S. & Skands, P. Z. PYTHIA 6.4 Physics and Manual. *JHEP* **05,** 026 (2006).

36. Czakon, M., Fiedler, P. & Mitov, A. Total Top-Quark Pair-Production Cross Section at Hadron Colliders Through $O(\alpha_S^4)$. *Phys. Rev. Lett.* **110,** 252004 (2013).

37. Czakon, M. & Mitov, A. NNLO corrections to top pair production at hadron colliders: the quark-gluon reaction. *JHEP* **01,** 080 (2013).

38. Czakon, M. & Mitov, A. NNLO corrections to top-pair production at hadron colliders: the all-fermionic scattering channels. *JHEP* **12,** 054 (2012).

39. Bärnreuther, P., Czakon, M. & Mitov, A. Percent Level Precision Physics at the Tevatron: First Genuine NNLO QCD Corrections to $q\bar{q} \to t\bar{t} + X$. *Phys. Rev. Lett.* **109,** 132001 (2012).

40. Cacciari, M., Czakon, M., Mangano, M., Mitov, A. & Nason, P. Top-pair production at hadron colliders with next-to-next-to-leading logarithmic soft-gluon resummation. *Phys. Lett.* **B710,** 612–622 (2012).

41. Czakon, M. & Mitov, A. Top++: A Program for the Calculation of the Top-Pair Cross-Section at Hadron Colliders. *Comput. Phys. Commun.* **185,** 2930 (2014).

42. Kidonakis, N. Next-to-next-to-leading-order collinear and soft gluon corrections for t-channel single top quark production. *Phys. Rev.* **D83,** 091503 (2011).

43. Kidonakis, N. Two-loop soft anomalous dimensions for single top quark associated production with a W- or H-. *Phys. Rev.* **D82,** 054018 (2010).

44. Kidonakis, N. NNLL resummation for s-channel single top quark production. *Phys. Rev.* **D81,** 054028 (2010).

45. Corcella, G. *et al.* HERWIG 6: An Event generator for hadron emission reactions with interfering gluons (including supersymmetric processes). *JHEP* **01,** 010 (2001).

46. Dittmaier, S. *et al.* Handbook of LHC Higgs Cross Sections: 2. Differential Distributions. doi:10.5170/CERN-2012-002. arXiv: 1201.3084 [hep-ph] (2012).

47. Lonnblad, L. & Prestel, S. Matching Tree-Level Matrix Elements with Interleaved Showers. *JHEP* **03,** 019 (2012).

48. Beenakker, W., Kramer, M., Plehn, T., Spira, M. & Zerwas, P. M. Stop production at hadron colliders. *Nucl. Phys.* **B515,** 3–14 (1998).

49. Beenakker, W. *et al.* Supersymmetric top and bottom squark production at hadron colliders. *JHEP* **08,** 098 (2010).

50. Borschensky, C. *et al.* Squark and gluino production cross sections in pp collisions at $\sqrt{s}$ = 13, 14, 33 and 100 TeV. *Eur. Phys. J.* **C74,** 3174 (2014).

51. *Summary of ATLAS Pythia 8 tunes* tech. rep. ATL-PHYS-PUB-2012-003 (CERN, Geneva, Aug. 2012). https://cds.cern.ch/record/1474107.

52. Martin, A. D., Stirling, W. J., Thorne, R. S. & Watt, G. Parton distributions for the LHC. *Eur. Phys. J.* **C63,** 189–285 (2009).

53. Aaboud, M. *et al.* Performance of the ATLAS Track Reconstruction Algorithms in Dense Environments in LHC Run 2. *Eur. Phys. J.* **C77,** 673 (2017).

54. *Optimisation of the ATLAS b-tagging performance for the 2016 LHC Run* tech. rep. ATL-PHYS-PUB-2016-012 (CERN, Geneva, June 2016). https://cds.cern.ch/record/2160731.

55. Aad, G. *et al.* Performance of b-Jet Identification in the ATLAS Experiment. *JINST* **11,** P04008 (2016).

56. *Electron efficiency measurements with the ATLAS detector using the 2015 LHC proton-proton collision data* tech. rep. ATLAS-CONF-2016-024 (CERN, Geneva, June 2016). http://cds.cern.ch/record/2157687.

57. Herde, H. E. Muon reconstruction performance in ATLAS at Run-II. *PoS* **EPS-HEP2015,** 285 (2015).

58. Aad, G. *et al.* Muon reconstruction performance of the ATLAS detector in proton–proton collision data at $\sqrt{s}$ =13 TeV. *Eur. Phys. J.* **C76,** 292 (2016).

59. Cacciari, M., Salam, G. P. & Soyez, G. The Anti-k(t) jet clustering algorithm. *JHEP* **04,** 063 (2008).

60. *Tagging and suppression of pileup jets with the ATLAS detector* tech. rep. ATLAS-CONF-2014-018 (CERN, Geneva, May 2014). http://cds.cern.ch/record/1700870.

61. *Selection of jets produced in 13TeV proton-proton collisions with the ATLAS detector* tech. rep. ATLAS-CONF-2015-029 (CERN, Geneva, July 2015). http://cds.cern.ch/record/2037702.

62. Hrynevich, A. *ATLAS jet and missing energy reconstruction, calibration and performance in LHC Run-2* tech. rep. ATL-PHYS-PROC-2017-045. 06 (CERN, Geneva, May 2017). https://cds.cern.ch/record/2263777.

63. *Performance of missing transverse momentum reconstruction for the ATLAS detector in the first proton-proton collisions at at $\sqrt{s}$= 13 TeV* tech. rep. ATL-PHYS-PUB-2015-027 (CERN, Geneva, July 2015). https://cds.cern.ch/record/2037904.

64. Heinemeyer, S., Hollik, W. & Weiglein, G. The Mass of the lightest MSSM Higgs boson: A Compact analytical expression at the two loop level. *Phys. Lett.* **B455,** 179–191 (1999).

65. Aaboud, M. *et al.* Jet energy scale measurements and their systematic uncertainties in proton-proton collisions at $\sqrt{s} = 13$ TeV with the ATLAS detector. *Phys. Rev.* **D96,** 072002 (2017).

66. Aad, G. *et al.* Jet energy resolution in proton-proton collisions at $\sqrt{s} = 7$ TeV recorded in 2010 with the ATLAS detector. *Eur. Phys. J.* **C73,** 2306 (2013).

67. Baak, M. *et al.* HistFitter software framework for statistical data analysis. *Eur. Phys. J.* **C75,** 153 (2015).

68. Verkerke, W. & Kirkby, D. The RooFit toolkit for data modeling. *ArXiv Physics e-prints.* eprint: `physics/0306116` (June 2003).

69. Collaboration, T. A. Search for direct top squark pair production in events with a Higgs or Z boson, and missing transverse momentum in $\sqrt{s} = 13$ TeV pp collisions with the ATLAS detector. *JHEP* **08,** 006 (2017).